Morphology Control and Efficiency Improvement on Organic Perovskite Solar Cells Fabricated by Solution-Process under Ambient Air Condition

by

Vincent Obiozo Eze

Dissertation submitted in partial fulfillment for the degree of

Doctor of Engineering

Under the supervision of Professor Tatsuo Mori

Department of Electricity and Materials Engineering
Graduate School of Engineering
Aichi Institute of Technology
Toyota Japan

March 2018

Contents

Chapter 1: Introduction

1.1 Need for renewable energy

The increase in industrialization and rapid growth in human population is envisaged to intensify the demand for energy in the near future by a significant proportion. The primary source of energy fossil fuel (coal, oil, and natural gas), which accounted for 66.7% of the world energy consumption has been predicted to exhaust in supply sooner or later (Fig. 1.1) [1]. Also, the primary source of energy does produce carbon dioxide (CO_2), which has been identified as the main cause of global warming [2, 3, 4].

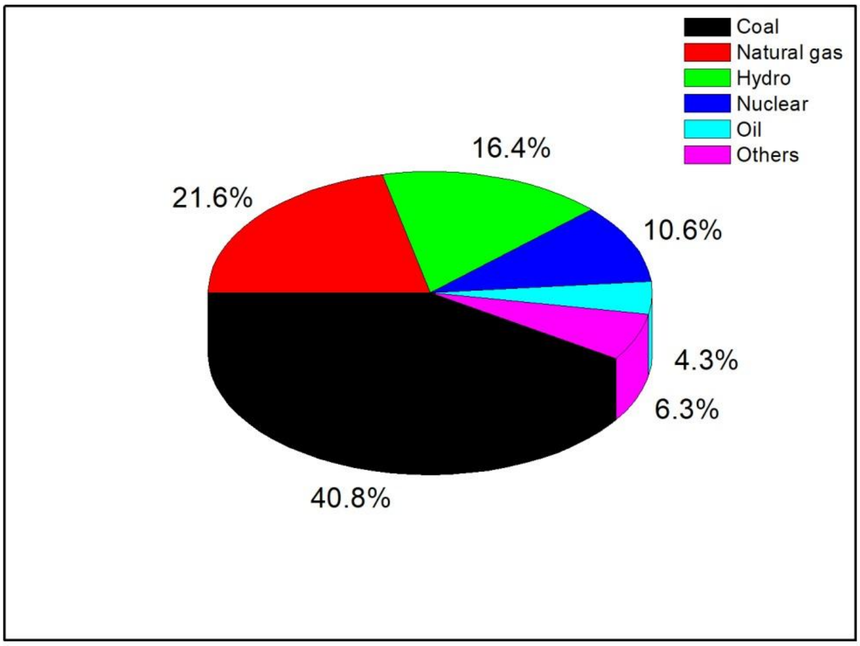

Fig. 1.1 2014 World energy consumption for electricity generation by the International Energy Agency (IEA, 2016) [5].

According to Fig. 1.1, nuclear power accounted for 10.6% of the world energy consumption. Nuclear power can also provide large-scale electricity generation. However, it has been proven to be extremely dangerous and hazardous. Clean and renewable energy such as the wind energy, biomass energy, geothermal energy, ocean energy, solar energy, and hydro power has gained significant attention as an outstanding candidate for the future power generation. These renewable energies are considered as the best substitutes for primary energy because they are environmentally benign and abundant. Among the renewable energy sources, solar energy is the most promising because of its enormous theoretical and technical potential for its use [6,7,8,9]. The amount of energy from sunlight striking the earth in 1 hour is about 4.3 x 10^{20} J, which is higher than all of the energy currently consumed on the planet in one year (4.1 x10^{20}J), yet human only utilizes a small fraction of this infinite solar resources [10, 11].

1.2 Solar Cells

A solar cell or photovoltaic device is required to capture a substantial amount of energy from the sunlight incident on the surface of the earth and convert it into electricity. Over the past four decades, various solar cells have been intensively investigated and used for solar energy conversion as shown in Fig. 1.2. Solar cells are broadly divided into two main groups (Inorganic and Organic solar cells). The prototype inorganic solar cell is a silicon-based P-N junction [12]. There are various forms of silicon solar cells and is by far the most extensively used solar cells. The single crystalline silicon solar cells are usually better than the polycrystalline silicon solar cells. As shown in Fig. 1.2 the single crystalline silicon solar cell has reached an efficiency of 27.6%. The GaAs solar cells have equally shown an unprecedented rise in efficiency (29.3%) rivaling that of the single crystalline silicon solar cell. The highest efficiency of over 40% has been achieved by the multi-junction GaAs solar cells. However, solar cells based on crystalline silicon and GaAs materials are expensive owing to their high production cost.

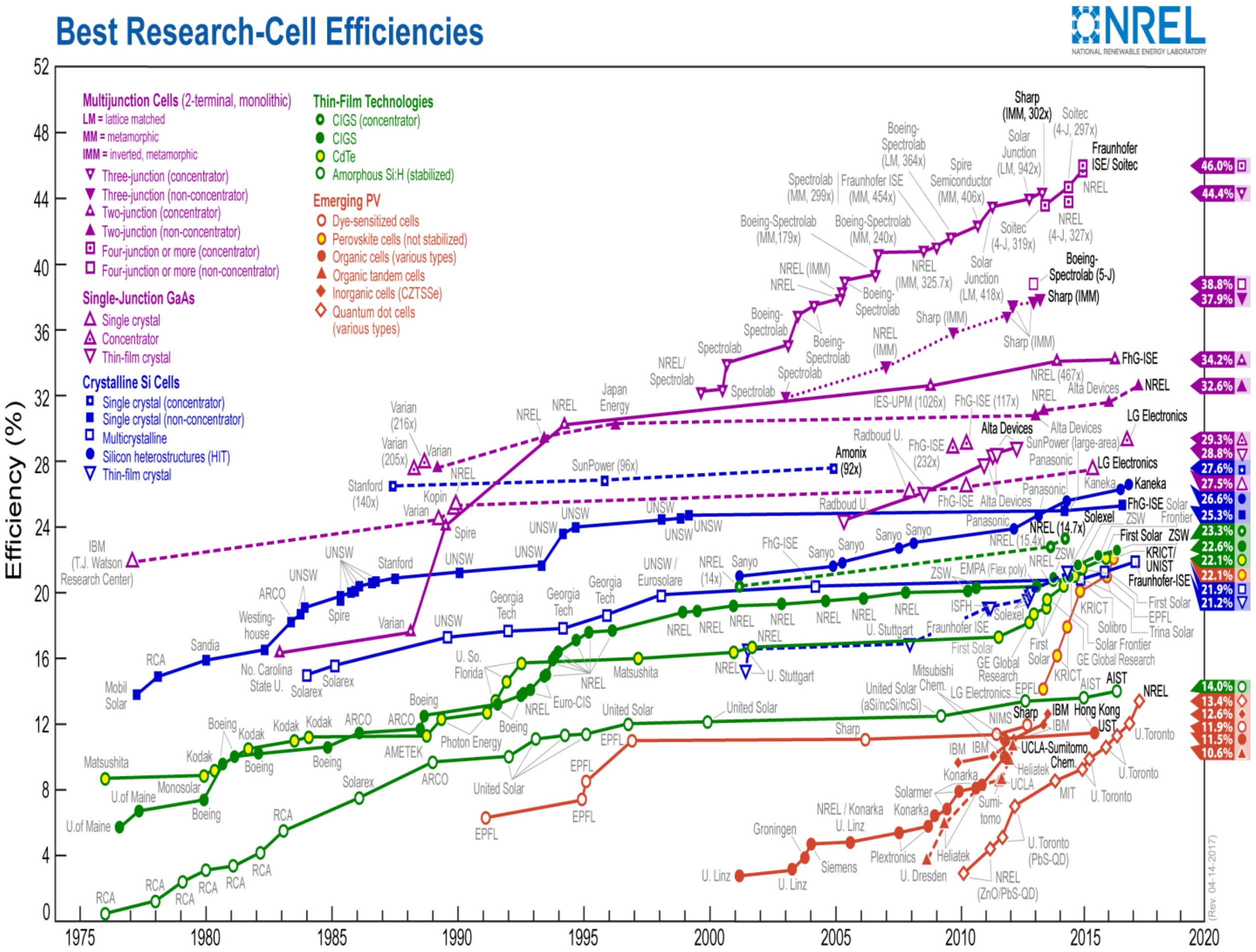

Fig. 1.2 Efficiency chart of solar cells over time. Adapted from the National Renewable Energy Laboratory (NREL) [13].

In order to reduce the production cost of crystalline silicon solar cells, various thin-film technologies such as copper indium gallium diselenide (CIGS), cadmium telluride (CdTe), and amorphous silicon have been developed. The CIGS and CdTe have achieved efficiency of 22.6% and 22.1%, respectively. These efficiencies are attractive and comparable to those of silicon solar cells. Also, the amorphous silicon solar cell which suffers from degradation under illumination achieved an efficiency of about 14.0% (Fig. 1.2) [9]. Emerging photovoltaics such as dye-sensitized solar cells (DSSCs), organic solar cells, polymer solar cells, quantum dot solar cells and perovskite solar cells (PSCs) have gained considerable attention.This is because they can be fabricated using solution-process, assembled using low-cost materials, and fabricated by cost-effective methods. These merits make them to be a very promising renewable energy technologies. However, DSSCs, quantum dot solar cells, and organic solar cells usually suffer from poor stability and efficiencies making them inferior to that of the crystalline silicon solar cells. In recent years, organic-inorganic hybrid halide perovskites have attracted much attention from the solar cells researchers, after it was first used as a light-absorbing material in a DSSC structure by Kojima and co-worker in 2009. With a certified efficiency of 22.1%, PSCs performance can be comparable to that of the CIGS and the traditional single crystalline silicon solar cells. PSCs have the potential to surpass the crystalline silicon solar cells regarding efficiency, cost, and stability and equally compete with the energy generated from fossil fuels. However, intensive research is still needed to solve some of the PSCs major drawbacks such as non-uniform film morphology, current-voltage hysteresis, Lead (Pb) toxicity, and stability.

1.2.1 Operation principle of Solar Cell

In any solar cell, the light to electricity conversion process can be broken down into the following steps:

- Generation of electron-hole pairs or excitons in the absorber material due to absorption of photons.
- The excited charge carriers (electron-hole pairs) are separated and moved towards the contact electrodes.
- The separated charge carriers are collected by the electrodes, where the electron flows through the external circuit before recombining with the hole.

Notably, the typical solar cell technology in use today is based on p–n junctions with p- and n-doped crystalline silicon as light absorber material. Fig 1.3 shows the energy diagram of a silicon solar cell p–n junction in equilibrium. The energy diagram explains the basic working principles of electron-hole separation in the corresponding solar cell. As it can be seen in Fig. 1.3, the electron in the valence band is excited into the conduction band when a photon with energy higher than the band gap is absorbed. The photo-excited charge carriers are separated, the hole diffuses to the metal contact, and the electron is swept across the junction by a strong built-in electric field and collected by the metal electrode.[12, 14)]

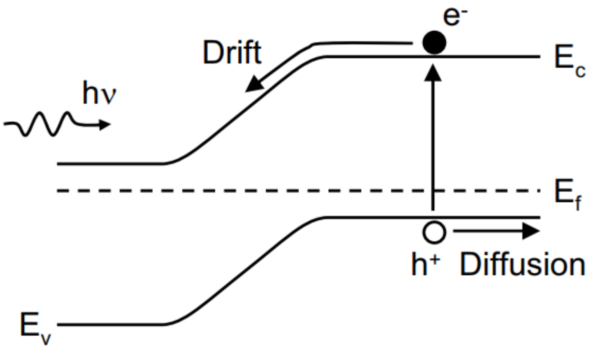

Fig. 1.3 Energy diagram of a silicon solar cell p–n junction [14]. (E_c, E_v, and E_F represent the conduction band, valence band, and Fermi energy level, respectively. While *hv* is the photon, where h is Planck's constant (J.s) and *v* is the frequency of the light (Hz))

1.2.2 Electrical Characterization of Solar Cells

Since solar cell converts light energy into electricity, the performance of the solar cell should be evaluated using electrical measurement. The most common characterization methods are the light and dark current-voltage *(I-V)* and quantum efficiency (QE) or incident photon-to-electron conversion efficiency (IPCE). These methods will be discussed in more detail hereafter.

1.2.3 Solar Spectral Irradiance

To accurately compare the *I-V* performance result of various types of solar cells, same measuring procedures should be followed. This is because the solar cell *I-V* performance depends on several parameters, such as weather (cloud cover, rain, snow, temperature), the time of the day (day, night), the time of the year (summer, winter), the incident light intensity, and the spectral intensity distribution of the incident light [9,15]. Considering that the spectral intensity distribution of the sunlight on the surface of the earth depends on several parameters, solar cell scientists and engineers have agreed to measure the *I-V* curves under defined illumination conditions [15]. Fig. 1.4a shows the schematic illustration of the air masses AM 0, AM 1.0, and AM 1.5. Fig. 1.4b presents the schematic illustration of the spectral distribution geometry. The normal of the receiving surface is tilted by an angle **t**, towards the equator. θ is the angle between the ground normal and the sun at zenith, which is used to calculate the AM as the inverse of cos (θ). The spectrum obtained after transmitted through a particular air mass is usually described by the abbreviation AM followed by a numeric figure [9]. As it can be seen in Fig 1.4a, outside the atmosphere of the earth, the solar spectrum has a defined spectral intensity distribution. This extra terrestrial spectrum is called the AM 0 spectrum according to American Society for Testing and Materials (ASTM) E4900-00 standard, and the solar constant is 1366.1 Wm^{-2} [9]. The least possible distance which the light has to pass through the atmosphere to approach the surface of the earth is at the equator, is termed AM 1.0 (Fig. 1.4a).

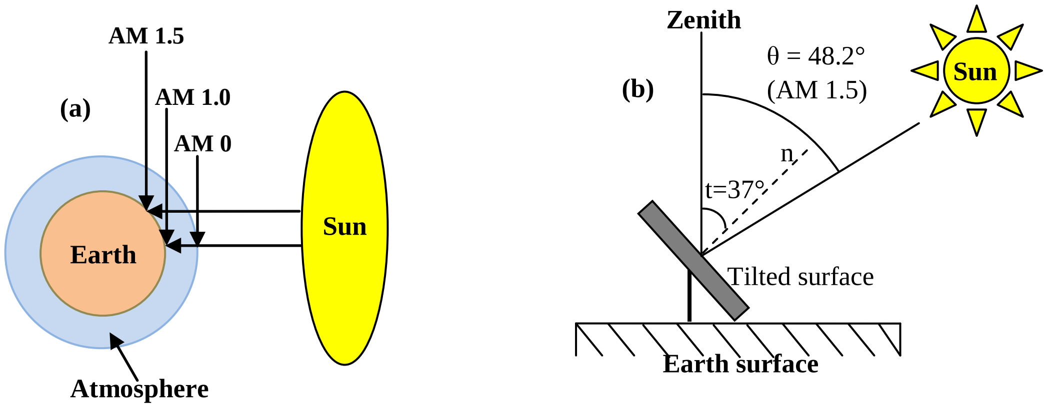

Fig. 1.4 (a) Schematic illustration of the air mass; AM 0, AM 1.0, and AM 1.5, (b) schematic illustration of the spectral distribution geometry depicting the earth, the sun, tilted angle **t,** and **θ.** The normal to the tilted surface is **n**. Note these figures are not drawn to scale, and it is just for illustration. Since the sun is larger than the earth the incident light area that showers the earth can be considered as planar (Fig. 1.4b). Note that the concept of these drawings is based on reference [9, 16].

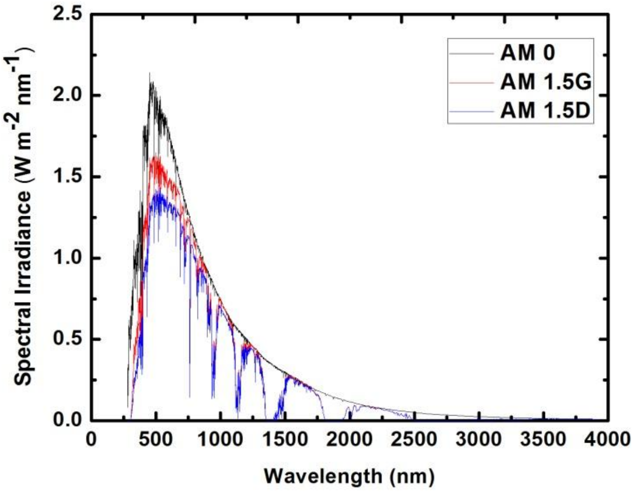

Fig. 1.5 Solar irradiation spectra of AM 0, AM 1.5G, and AM 1.5 D according to ASTM standard.

Fig. 1.5 shows the solar spectral irradiance versus wavelength of AM 0, AM 1.5G and AM1.5D. The AM 1.5G (where G stands for the Global standard by ASTM G173) spectrum has been chosen as the most widely accepted standard to measure solar cell performance data [15]. This spectrum corresponds to specific angular orientations, where the sun is located at an angle of about 48.2° with reference to the zenith, and where the surface normal of the solar cell forms an angle of 37° with reference to the zenith (Fig. 1.4b) [15,16]. AM 1.5G has a total power of 1000 W/m^2 which is obtained by integration. The AM 1.5 spectrum is also known as AM 1.5D where D stands for direct, and circumsolar, which is the easiest spectrum to achieve reproducibly. The AM 1.5D is obtained merely when viewing the sun through a circular aperture with an opening angle of 5.8°, i.e., the sun is at the center of the aperture. The sunlight that is obtained through such an aperture includes the irradiance from solar disk together with irradiation from the corona. AM 1.5D spectrum has a total power of 901W/m^2 which can be obtained by integration [9].

1.2.4 Equivalent Circuit of Solar Cell

Usually, a solar cell behaves like a diode when measured in the dark. Therefore, for an ideal p–n junction solar cell, the dependence of the current density on voltage is given by the Shockley diode equation [15, 17].

$$J(\mathrm{V}) = J_0\,[\exp\left(\frac{\mathrm{eV}}{\mathrm{k_B T}}\right) - 1] \qquad 1.1$$

where e is the elementary charge (C), V is the applied voltage (V), k_B is the Boltzmann constant (J.K^{-1}), T is the temperature (K), and J_0 is the reverse saturation current density (A/cm^2), i.e., the current density passing through the diode when a relatively high reverse bias is applied. Fig. 1.6 shows the equivalent circuit diagram of a solar cell, where a constant-current source is in parallel with the junction. J_{ph} is photocurrent density generated under illumination (A/cm^2). R_{sh} and R_s are the parasitic shunts and series resistances (Ω), respectively. The R_{sh} can be determined from the slope of the current density–voltage (J–V) curve near the short-circuit current density point. While R_s can be extracted from the slope of J-V curve at the open circuit voltage point. In an ideal solar cell, the value of R_{sh} and R_s are respectively infinity and zero.

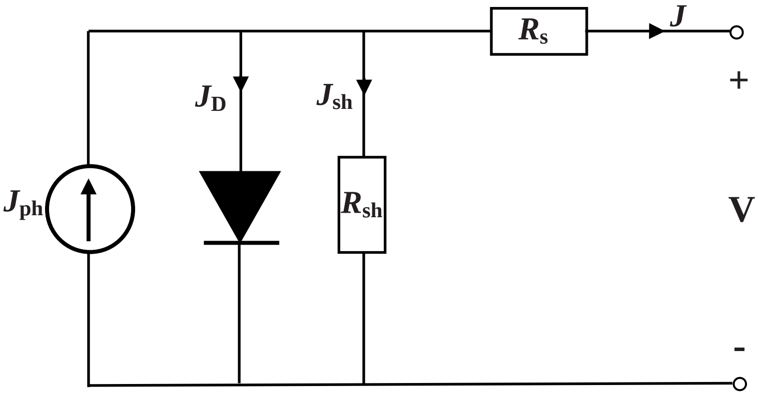

Fig. 1.6 Equivalent circuit diagram of a typical silicon solar cell with a single diode

From the equivalent circuit above, the expression for the current density J is shown in equation 1.2

$$J = J_{\mathrm{ph}} - J_{\mathrm{D}} - J_{\mathrm{sh}} \qquad 1.2$$

Where J_{D} is the diode current density, and J_{sh} is the current density lost due to R_{sh}. For a single diode model, J_{D} can be estimated using the Shockley equation of an ideal diode shown in equation 1.3

$$J_{\mathrm{D}} = J_0 \left[\exp\left(\frac{e(V + JR_s}{nk_{\mathrm{B}}T}\right) - 1\right] \qquad 1.3$$

Herein, n represents the diode ideality factor. For an ideal diode n=1. Therefore, if we substitute equation 1.3 into equation 1.2, the equation becomes:

$$J = J_{\mathrm{ph}} - J_0 \left[\exp\left(\frac{e(V + JR_{\mathrm{s}}}{nk_{\mathrm{B}}T}\right) - 1\right] - J_{\mathrm{sh}} \qquad 1.4$$

Equation 1.4 can be further expressed as:

$$J = J_{\mathrm{ph}} - J_0 \left[\exp\left(\frac{e(V + JR_{\mathrm{s}}}{nk_{\mathrm{B}}T}\right) - 1\right] - \frac{V + JR_{\mathrm{s}}}{R_{\mathrm{sh}}} \qquad 1.5$$

Equation 1.4 &1.5 can be used to analyze the experimental *J–V* curves of a typical p–n junction, organic and hybrid solar cells under solar irradiation [15]. Several parameters can be deduced from the *J–V* curve under illumination, which will be discussed in more detail hereafter.

1.2.5 Current-Voltage Characteristics

The measurement of *I–V* is one of the simplest methods to evaluate the performance of solar cells. The light and dark measurements of the *I–V* curves can be conducted by applying a bias voltage between the contacts of the solar cell. The measured dark *I–V* curve can give information about the charge conduction in the device.

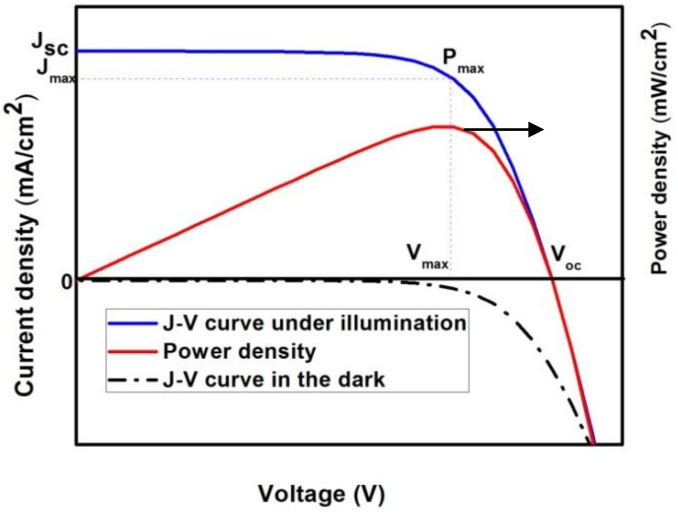

Fig. 1.7 *J–V* characteristics of a typical PSC showing different measuring conditions (under illumination, and in the dark). The power density is obtained by multiplying the voltage by the current density.

Whereas, from the illuminated *J–V* curve, parameters such as maximum power (P_{max}), the short-circuit current density (J_{sc}), open-circuit voltage (V_{oc}), and Fill Factor (FF) can be deduced. Thus, the power conversion efficiency (PCE) can be determined from these parameters. Fig. 1.7 shows the *J–V* curves of a typical PSC measured under illumination with simulated sunlight (AM 1.5 G, 100 mW/cm^2).

1.2.6 Short-circuit current density

The J_{sc} is the current that flows through the external circuit when the electrodes of the solar cell are short-circuited [18]. In other words, J_{sc} is the current density generated when the solar cell's applied voltage is zero (i.e., no current is injected by an external voltage source) under illumination [15]. It is worth mentioning that J_{sc} of a solar cell depends on several factors such as photon flux density, the area of the light-absorbing material, and optical properties of the active area.

1.2.7 Open-circuit voltage

The V_{oc} is the voltage at which no current flows through the external circuit. It is the maximum voltage that solar cells can supply [18]. For a conventional p–n junction solar cell, V_{oc} is a function of T, J_{ph}, and J_0 (see equation 1.6). Also, V_{oc} is related to the amount of recombination in the solar cell.

$$V_{\mathrm{oc}} = \frac{nk_{\mathrm{B}}T}{e}\ln\left(\frac{J_{\mathrm{ph}}}{J_0}+1\right) \qquad 1.6$$

1.2.8 Fill Factor

The FF is the ratio between the maximum power generated by a solar cell and the product of V_{oc} and J_{sc}. As shown in Fig. 1.7, the P_{max} produced by a solar cell can be estimated using equation 1.7.

$$P_{\mathrm{max}} = J_{\mathrm{max}}\,V_{\mathrm{max}} \qquad 1.7$$

where J_{max} and V_{max} are the corresponding maximum voltage (V) and current density of the solar cell, respectively. The mathematical expression of the FF is shown in equation 1.8

$$FF = \frac{P_{\mathrm{max}}}{J_{\mathrm{sc}}\,V_{\mathrm{oc}}} = \frac{J_{\mathrm{max}}V_{\mathrm{max}}}{J_{\mathrm{sc}}V_{\mathrm{oc}}} \qquad 1.8$$

1.2.9 Power Conversion Efficiency

The PCE or η can be estimated as the ratio of the P_{max} generated by a solar cell to the incident power (P_{in}) [18]. For AM 1.5G, P_{in} is calculated to be 1000W/m^2. This has become the standard value for measuring the η of solar cells. The η of a solar cell can be calculated using the expression in equation 1.9.

$$\eta = \frac{P_{\mathrm{max}}}{P_{\mathrm{in}}} = \frac{J_{\mathrm{max}}\, V_{\mathrm{max}}}{P_{\mathrm{in}}} \text{ x } 100\% \qquad 1.9$$

Using the definition of the FF, η can also be expressed by equation 1.10

$$\eta = \frac{P_{\mathrm{max}}}{P_{\mathrm{in}}} = \frac{J_{\mathrm{sc}}\, V_{\mathrm{oc}}\, FF}{P_{\mathrm{in}}} \text{ x } 100\% \qquad 1.10$$

1.2.10 Quantum Efficiency Measurements

The quantum efficiency involves the external quantum efficiency (EQE) and internal quantum efficiency (IQE) [19]. The EQE is the number of extracted electron-hole pairs per incident photon (equation 1.11).

$$EQE = \frac{number\ of\ electrons\ collected}{number\ of\ incident\ photons} \qquad 1.11$$

IQE can be determined by the light reflectance and the spectral response. EQE is sometimes called the incident photon-to-current efficiency (IPCE). The latter is a technique used to evaluate how different absorbing materials used in the cell affect the photocurrent generation [15]. In most cases, EQE is measured with a light source (realized by a monochromatic light) at low light intensity. Fig. 1.8 shows the IPCE curve of PSC with an excitonic absorption peak at around 780 nm. Usually, for ideal quantum efficiency, the IPCE value reaches 100% for the entire absorbance wavelength. However, in solar cells, the quantum efficiency is usually less than 100% due to recombination effects and defects in the device.

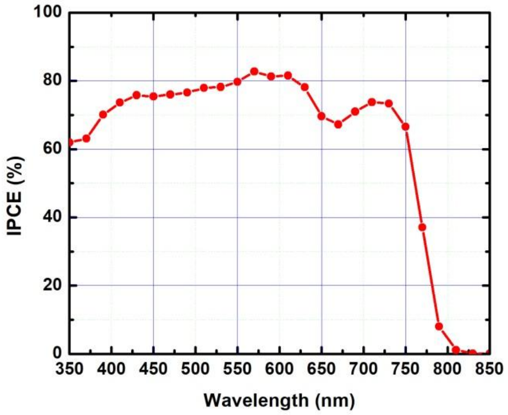

Fig. 1.8 a typical IPCE curve of PSC

IPCE can be calculated using the following expression in equation 1.12.

$$IPCE(\%) = \frac{hc\, J_{sc}}{e\lambda\, P_{in}} \qquad 1.12$$

where *h* is the Planck's constant (J.s), *c* is the speed of light (m/s), λ is the wavelength of light (nm), *e* is the elementary charge (C), and P_{in} is the photon flux. In DSSCs, IPCE can be expressed according to equation 1.13) [20].

$$IPCE(\lambda) = \eta_{LHE}\, \eta_{inj}\, \eta_c \qquad 1.13$$

where η_{LHE} is the light harvesting efficiency at a certain wavelength, η_{inj} is the electron injection efficiency, and η_c is the electron collection efficiency. Inorganic solar cells, the EQE can be represented by the product of each efficiency described in equation 1.14 [21].

$$\eta_{EQE} = \eta_A\, \eta_{ED} \eta_{CT}\, \eta_{CC} \qquad 1.14$$

where η_A is the light absorption efficiency, η_{ED} is the exciton diffusion efficiency to the donor–acceptor interface, η_{CT} is the charge transfer efficiency, and η_{CC} is the charge collection efficiency at the electrodes. In principle, the J_{sc} can be calculated by the integration of IPCE for the whole solar spectrum. The relationship between the IPCE and the corresponding J_{sc} is shown in equation 1.15.

$$J_{\mathrm{sc}} = \frac{e}{hc}\int_{\lambda_{min}}^{\lambda_{max}} P_{\mathrm{AM\ 1.5G}}\,(\lambda) IPCE(\lambda)\ \lambda d\lambda \qquad 1.15$$

where $P_{\mathrm{AM\ 1.5G}}$ is assumed to be equivalent to photon flux. It is worth mentioning that in practice, the J_{sc} estimated according to equation 1.15 does not always match well the corresponding value obtained from the *J–V* measurements. This is due to the mismatch between the spectral irradiance provided by the solar simulator and AM 1.5G spectrum.

1.3 Perovskite solar cells

1.3.1 What is Perovskite?

Perovskite is any material that has the same mineral structure of calcium titanium oxide ($CaTiO_3$). The structure $CaTiO_3$ was discovered by a German mineralogist Gustav Rose in 1839. Perovskite derived its name from a Russian mineralogist Lev A. Perovski (1792–1856), following his pioneering work on the mineral structure [22]. The family of perovskite has the general formula ABX_3, where A and B are cations of different sizes, and X is an anion, where X=oxygen, halogens, or alkali metals (Fig. 1.9). Among the perovskite family, oxide-based perovskites have been extensively studied because of their superior ferroelectricity, magnetic, and superconductive properties [23, 24]. In 1958, Moller characterized the first halide-based perovskite structure, cesium lead halide ($CsPbX_3$) [25]. Later, in 1978 Weber and Naturfosch studied methylammonium lead halide ($CH_3NH_3PbX_3$, where X=I, Cl, Br). In the 1990s, Mitzi and coworkers studied the optoelectronics properties of $CH_3NH_3PbX_3$ perovskites, which was later employed in thin films transistors (TFT) and light-emitting diodes (LED) [26].

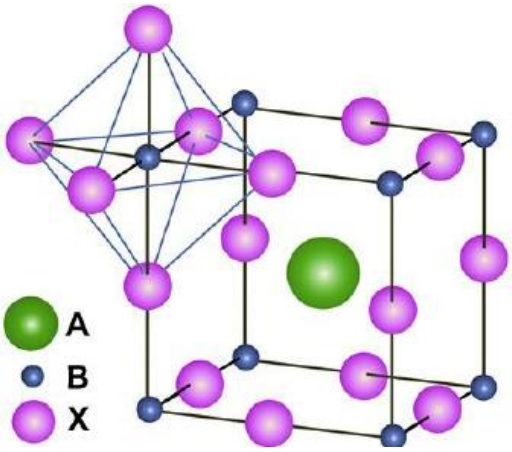

Fig. 1.9 Cubic structure of $CH_3NH_3PbI_3$ perovskites with the general chemical formula ABX_3 organic or inorganic cations occupy position A (green) whereas metal cations and halides occupy the B (blue) and X (purple) positions, respectively. Adapted from reference [27].

1.3.2 Perovskite crystal structure and composition

As mentioned in section 1.3.1, the general formula of perovskite is ABX_3.The most researched perovskites are methylammonium lead triiodide perovskite ($CH_3NH_3PbI_3$), mixed halide perovskites ($CH_3NH_3PbI_{3-x}Cl_x$ and $CH_3NH_3PbI_{3-x}Br_x$), and formamidinium lead triiodide ($NH_2CHNH_2PbI_3$, $FAPbI_3$) adopt the general perovskite chemical formula ABX_3. Where A is the organic cations $CH_3NH_3^+$ (MA^+) and $HC(NH_2)_2^+$ (FA^+), B is metal cation (Pb^{2+}, Sn^{2+}), and X is halide anion (Cl^-, Br^-, I^- or mixed halides) [28]. In an ideal perovskite crystal structure, B is surrounded by an octahedron of anions [BX_6^{4-}], while A is 12-fold cuboctahedra coordinated with X anions, as shown in Fig. 1.9 [27, 29]. It is worth noting that the degree of stability and physical properties of perovskites (electronic, magnetic, and dielectric) depends crucially on the tolerance factor. The Goldschmidt tolerance factor (t) (Equation 1.15) can be used to measure the distortion between the A–X and B–X bond lengths [30].

$$t = \frac{(R_A + R_X)}{\sqrt{2}(R_B + R_X)} \qquad 1.15$$

Where R_A, R_B, R_X, is the ionic radii of A, B, X, respectively.

To alleviate the mismatch of crystal components and octahedral tilting of perovskite, t should be close to 1. Typically, the cubic structure for oxide perovskites is in the range $0.89<t<1$ [31], whereas halide perovskite ranges from $0.85<t<1.11$ [32]. For hybrid halide perovskite, the B site is normally surrounded by a large atom of Pb or Sn. Therefore, A site must be large enough to maintain the tolerance factor. If the A site is not large enough, the cubic structure and symmetry will be distorted and reduced, respectively. When A site is surrounded by voluminous anions, such as long-chain alkylamine, the lead halide perovskite becomes a two-dimensional (2D) layer structure [33, 34]. *Li et al.* proposed the octahedral factor (μ) shown in equation 1.16 can be used to further support the Goldschmidt's tolerance factor [32].

$$\mu = \frac{R_B}{R_X} \qquad 1.16$$

For halide perovskite μ is in the range of 0.442-0.895 [32]. t and μ provide a useful guideline for predicting halide perovskite formability. However, they are not entirely sufficient for determining structures of all the perovskite family [24, 32]. Furthermore, according to X-ray diffraction (XRD) results, perovskite crystals have different phases such as cubic, tetragonal, and orthorhombic [35]. Typically, perovskites adopt cubic structures and encounter phase transitions from cubic to tetragonal to orthorhombic with respect to temperature [36]. Kanatzidis et al. have studied the structural phase α, β, γ transformations for the most researched hybrid perovskites. Where α, β, and γ signify high temperature, intermediate temperature, and low-temperature phases, respectively [37].

1.3.3 Overview of the development of perovskite solar cells

In 2006 Miyasaka and co-workers first incorporated $CH_3NH_3PbBr_3$ perovskites as a sensitizer on nanoporous TiO_2 in liquid electrolyte-based dye-sensitized solar cells (DSSCs) and achieved an efficiency of 2.2% [38]. Later in 2009, the PCE of their device reached 3.8% by replacing the Br with I [39]. It was found that the devices were prone to dissolution and poor stability due to the polar electrolyte solution. In 2011, the PCE of perovskite-sensitized solar cells gradually increased to about 6.5% by Park and co-workers [40]. To further improve the PCE and stability of PSCs a solid electrolyte 2,2',7,7'-tetrakis (*N*,*N*-di-p-methoxyphenylamine)-9,9'-spirobifluorene (Spiro-OMeTAD) was incorporated as a hole transport material (HTM) in 2012. This led to achieving a PCE of 9.7% and improved device stability [41]. Later, in 2012 Snaith and co-workers achieved a PCE of 10.9% using a mesoporous alumina (Al_2O_3) scaffold as an electron transport layer (ETL), and $CH_3NH_3PbI_{3-x}Cl_x$ perovskite to fabricate meso-superstructure solar cells (MSSCs) [42]. In 2013, Grätzel and co-workers reported the sequential deposition method to fabricate high-performance perovskite-sensitized solar cell and achieved an efficiency of about 15.0% [43]. In order to simplify the device architecture, later in 2013, Snaith and co-workers developed n-i-p (n, i, p refers to the electron transporting layer, light-absorber layer, and hole transporting layer, respectively) planar heterojunction structure PSCs. The planar PSCs without the mesoporous layer exhibited a PCE of 15.4% [44]. Since then, the PCEs of PSCs with various geometries and processing methods have been developed, and its PCE reaching 22.1% [45]. It has been widely reported that the high efficiency exhibited by PSCs can be attributed to its excellent photovoltaics properties such as tunable bandgaps [46], large absorption coefficients [41], high charge carrier mobility [47], long exciton diffusion length [48, 49], and small exciton binding energy (<50 meV) [50].

1.3.4 Perovskite solar cell architectures

In this type of solar cell, the light-absorbing layer (perovskite) is usually sandwiched in between an ETL and a hole transport layer (HTL). Since the first report of PSC by Miyasaka and coworkers in 2009, various architectures have been developed to fabricate high-performance PSC. In this section, I will discuss only the most commonly used structures, which are: (a) Mesoporous structure, (b) Bi-layer mesoporous structure, (c) n-i-p planar structure, (d) p-i-n planar structure.

1.3.5 Mesoporous structure

The first geometry of PSC evolved from the solid-state DSSCs structure. Fig. 1.10(a) shows the schematic illustration of a typical mesoporous structure. The mesoporous structure is made up of fluorine-doped tin oxide (FTO) glass substrate followed by a compact ETL (usually titanium oxide (TiO_2) with a thickness of about 50 nm). Next is a mesoporous ETL (TiO_2, Al_2O_3) with a film thickness of about 350 nm or more. The light-absorbing layer "perovskite" is deposited onto the mesoporous layer followed by a HTL (e.g., Spiro-OMeTAD) with a film thickness of about 250 nm. Finally, about 80 nm of a metal contact (Au) is deposited on the HTL [40-43]. A PCE of over 15.0% has been achieved with the mesoporous structure [43].

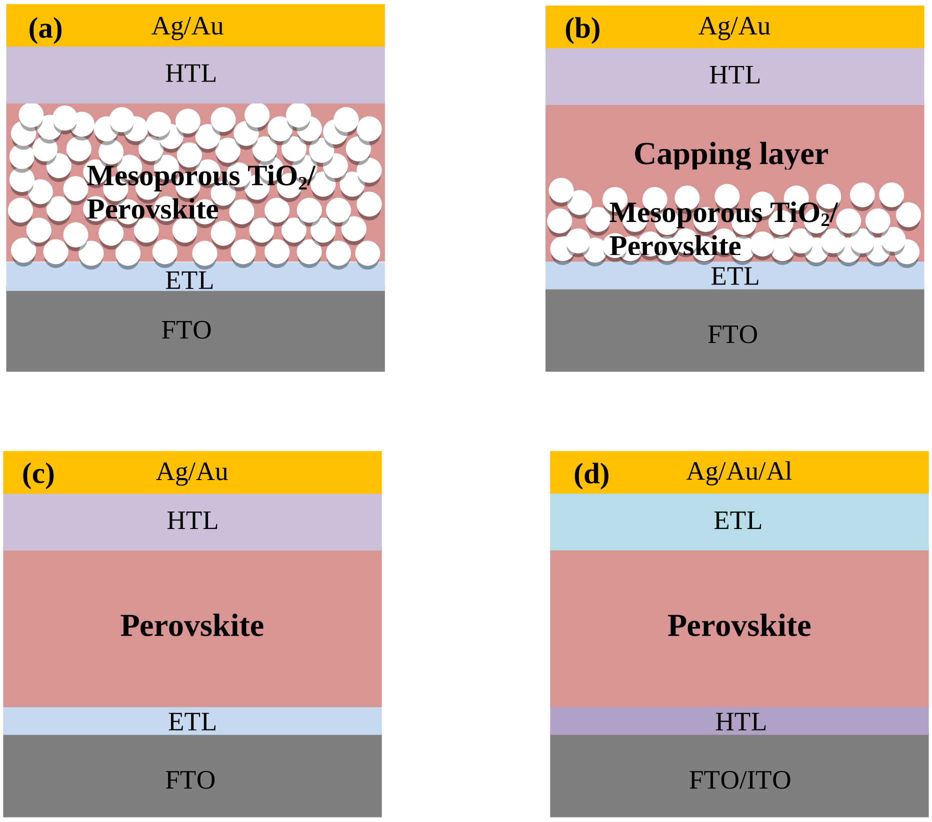

Fig. 1.10 The schematic illustrations of the (a) mesoporous structure, (b) bi-layer structure, (c) n-i-p planar structure and (d) p-i-n planar structure. FTO, ITO, ETL, and HTL represents fluorine-doped tin oxide; Indium-doped tin oxide, electron transport layer, and hole transport layer, respectively.

In this type of structure, the perovskite light-absorbing layer is usually fabricated by two-step deposition method [43]. The surface coverage, grain size, uniformity, roughness of the perovskite layer, which is solely controlled by the underneath mesoporous layer strongly, affects the device performance and reproducibility [51-53]. The mesoporous structure has the advantage of less pronounce hysteresis in the *J*–*V* measurements and the disadvantage of the high-temperature annealing process. The mesoporous structure is not a feasible approach when considering large area device on a low-temperature flexible substrate.

1.3.6 Bi-layer structure

Fig. 1.10 (b) shows the schematic illustration of the bi-layer structure. The overall thickness of the mesoporous scaffold of this type of structure is usually thinner than the conventional mesoporous structure [54, 55]. The capping layer structure was developed to prevent possible shunting pathways in the device, which results from insufficient pore-filling of the perovskite into the mesoporous scaffold [54, 56, 57]. PSCs employing the bi-layer structure have demonstrated high PCEs (>15%) with negligible *J–V* hysteresis [58, 59, 60].

1.3.7 n-i-p planar structure

Fig. 1.10 (c) shows the schematic illustration of a typical n-i-p planar structure, which consists of FTO/ETL/perovskite/HTL/metal contact (Au/Ag). The ideology of n-i-p planar PSCs could be tracked back to Al_2O_3-based mesoporous PSC [42]. Snaith and coworkers found that high-performance PSCs could be achieved without the mesoporous TiO_2 ETL. In 2013, Snaith et al. achieved a PCE of 15% for planar based PSCs fabricated via vapor deposition method [32, 44]. Since then n-i-p planar PSC architecture has gained considerable attention among the PSCs research community. The planar structure was feasible because the metal halide perovskite exhibits ambipolar properties, long charge carrier diffusion lengths of about 100 nm for $CH_3NH_3PbI_3$ and 1000 nm for $CH_3NH_3PbI_{3-x}Cl_x$ [48, 49]. This architecture offers the advantages of simplified device geometry, easy fabrication methods, versatility for device optimization and low cost for mass production. However, n-i-p planar PSC also suffers from poor film formability especially when prepared using solution process and much worse *J–V* hysteresis than the mesoporous devices [61, 62].

1.3.8 p-i-n planar structure

Fig. 1.10 (d) shows the schematic illustration of a typical p-i-n planar structure PSC. The concept of this type of architecture was derived from the traditional organic solar cells [63]. The first p-i-n planar PSC employed the traditional poly 3,4-ethylenedioxythiophene): poly(styrenesulfonic acid) (PEDOT: PSS) and fullerene derivative as the HTL and ETL, respectively, which exhibited a PCE of 3.9% [63]. At that time, it was found the non-constant perovskite morphology on PEDOT: PSS HTL led to the low PCE. To optimize the PCE of p-i-n PSC structure, several attempts were made to improve the perovskite film formation and interface engineering [64-70]. It is worth noting that the p-i-n PSC structure has the advantages of the possibility of low-temperature preparation, avoiding the need of dopants in the HTL and compatibility with organic electronics manufacturing processes [71]. These features are somewhat difficult to achieve in n-i-p PSC structure.

1.3.9 Energy band diagram of typical PSCs

Perovskite $CH_3NH_3PbI_3$ is a direct bandgap semiconductor material with an optical band gap energy approximately 1.5eV, which correspond to an absorption onset of about 800 nm. The large absorption coefficient in the visible region (~10^5 cm^{-1}) enables efficient light-harvesting by building a high density of photoexcited charges with ~ 300 nm thick layer [41, 46, 72].

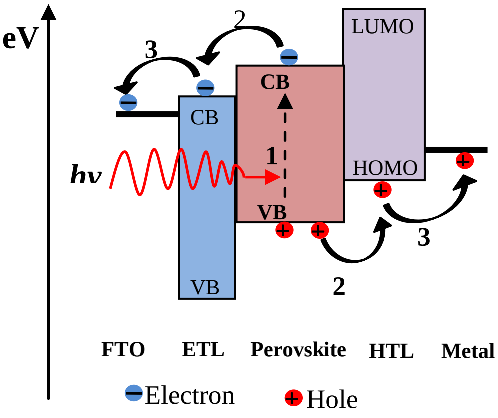

Fig. 1.11 Energy band diagram of n-i-p PSC describing the process of light absorption and generation of free carriers. *hv* is the photon energy, where h is the Planck's constant and *v* is the photon's frequency.

Fig. 1.11 shows the energy band diagram of a typical n-i-p structure PSC demonstrating the process of the charge transfer mechanisms. According to previous reports, the 1.5 eV band gap of $CH_3NH_3PbI_3$ perovskite is mainly determined by the $[PbI_4]^{6-}$ network. This suggests that the organic component somewhat does not influence the band gap energy, however, is responsible for the formation of the 3D perovskite crystal [73-78]. As shown in Fig. 1.11, absorption of photons creates electron-hole pairs in the perovskite. These charge carriers could exist as free carriers or form excitons with a small binding energy in the range of a few milli-electron volts (19-50 meV), which is contrary to that observed in organic solar cells [79]. Next, the electron-hole pairs are thermalized and transported to the ETL and HTL respectively. Finally, the electron and hole are extracted by the FTO and metal contact (Au or Ag), and thus a complete circuit is formed. The $CH_3NH_3PbI_3$ perovskite possesses excellent attributes that are crucial for the development of efficient solar cells. Among these attributes, the strong optical absorption, long electron-hole diffusion lengths, and small exciton binding energy or non-excitonic nature of the charge generation are essential to the outstanding performance of PSCs. Most especially, the high V_{oc} observed in PSCs, which further suggest that the energetic cost associated with exciton splitting is not predominant [79,80, 81].

1.3.10 Deposition of metal halide perovskite film

In PSCs, the quality of the perovskite film is paramount important. It often determines the performance of the device. To achieve high-performance PSCs, it is crucial to fabricate perovskite film with high crystalline and uniform morphology. Perovskite films can be fabricated via vapor deposition and solution process methods [44,82-84]. The vapor deposition method was firstly demonstrated by Snaith and coworkers in 2013 [44]. They employed dual source evaporation systems that separately contain the methylammonium iodide (CH_3NH_3I) and lead chloride ($PbCl_2$) to deposit high-quality $CH_3NH_3PbI_{3-x}Cl_x$ films, exhibiting a PCE of about 15.0% (Fig. 1.12(a)). Despite the high PCEs achieved by vapor deposition methods, it has the disadvantage of the possibility of high-cost manufacturing, since it requires advanced and expensive vacuum facilities. As demonstrated by Chen et al., the vapor-assisted solution process (VASP) is combining solution process of lead iodide (PbI_2) layer and vapor deposition of CH_3NH_3I to form perovskite film with full coverage, microscale grain size and uniform grain structure, which exhibited a PCE of about 12.1% (Fig. 1.12(b)) [84].

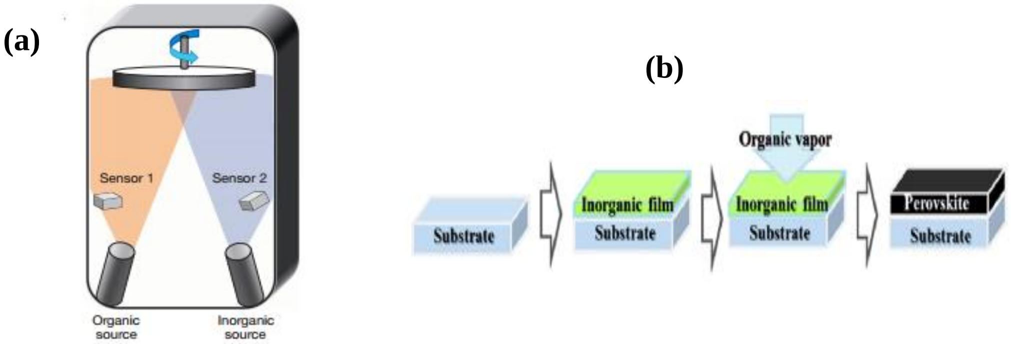

Fig. 1.12 Schematic illustration of perovskite film deposition. (a) Dual-source thermal evaporation system, adapted from reference [44]. (b)Vapor-assisted solution process, adapted from reference [84].

Solution process methods are divided into two major types: one-step and two-step methods. Under the two-step methods, there are two types of techniques: (i) sequential deposition and (ii) two-step spin-coating methods. The solution processing methods have the advantages of ease fabrication and low-cost manufacturing even on large substrates. Among all the deposition methods, one-step solution method is the simplest and easiest. It involves the spin-coating of a mixture of PbX_2 and CH_3NH_3X (X=Cl, Br, I) in a polar solvent such as γ-butyrolactone (GBL), *N*,*N*-dimethylformamide (DMF) or dimethylsulfoxide (DMSO) on top of the planar substrate or a mesoporous scaffold and followed by thermal annealing (Fig. 1.13) [41,42,61,85-88]. Perovskite films prepared by one-step solution process are usually prone to pinhole and non-constant morphology especially on planar substrates [61].

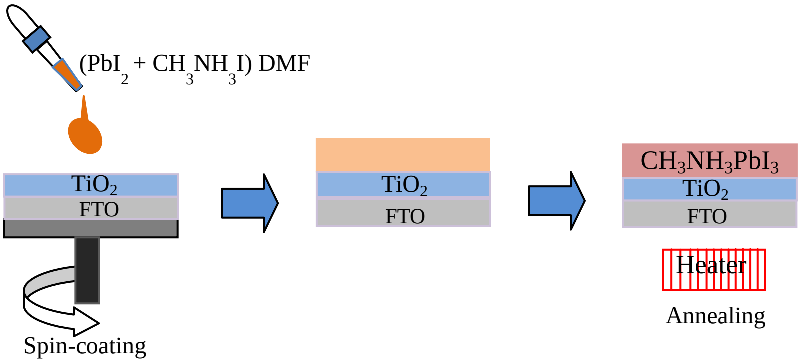

Fig. 1.13 Schematic illustration of one-step spin-coating method

The two-step sequential deposition method was first reported by Mitzi and coworkers in 1998 to make perovskite film [89]. In 2013, Grätzel and coworkers adopted this approach to fabricate high-quality perovskite film on a mesoporous structure [43]. The two-step sequential method involves the spin-coating of the PbI_2 precursor onto a mesoporous or planar substrate to form PbI_2 film and followed by dipping into CH_3NH_3I- Isopropanol (IPA) solution to form $CH_3NH_3PbI_3$ (Fig. 1.14(a)). In this method, the morphology of the final perovskite film depends on the nature of the PbI_2 film, and the dipping time of PbI_2 film into the CH_3NH_3I-IPA solution [32]. The two-step sequential deposition method is mostly suitable for mesoporous structure PSCs. However, on planar substrates, the perovskite formation is usually associated with problems such as dissolution and peeling-off due to the long soaking time of PbI_2 film into the CH_3NH_3I-IPA solution [32, 89, 90]. The long soaking time is required to achieving sufficient diffusion and intercalation of CH_3NH_3I into the compact PbI_2 films [32].

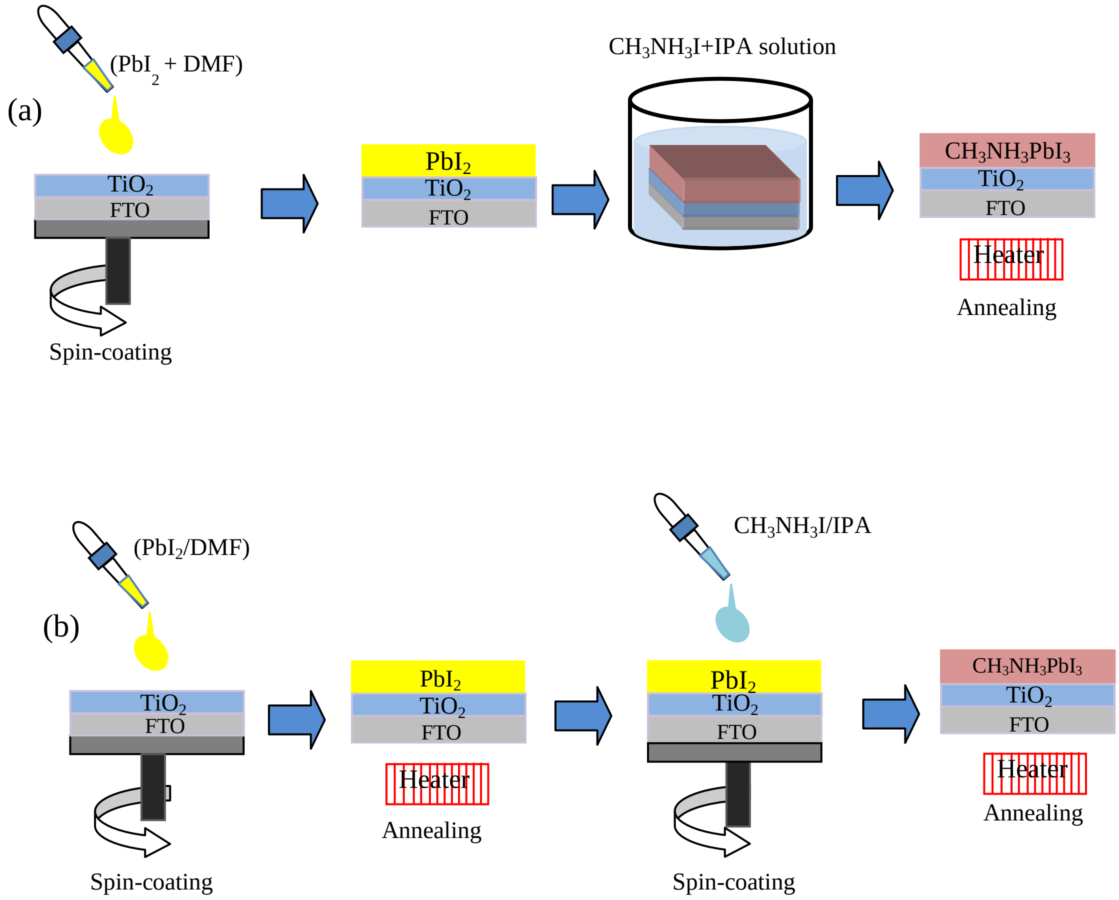

Fig. 1.14 Schematic illustration of: (a) sequential deposition method (b) two-step spin-coating method.

In order to circumvent the problem of incomplete conversion of PbI_2 into perovskites, and gain a better control of perovskite morphology, Park and his co-workers proposed the two-step spin-coating approach, in which the CH_3NH_3I-IPA solution is dropped onto the PbI_2 precursor film, followed by spin coating (Fig. 1.14(b)) [32, 58, 92]. Later in 2014, Xiao et al. adopted the two-step spin-coating approach and developed the interdiffusion strategy. The resultant perovskite film was treated by a solvent-vapor-assisted annealing which led to a high-quality perovskite film [66,68]. Since then, several research groups have adopted the two-step spin-coating method or the modified interdiffusion approach to fabricate high-performance and reproducible PSCs [66,68,93-96]. Compared to two-step sequential method, two-step spin-coating technique is a well-defined method because it can quantitatively manage the fabrication process [92].

1.3.11 Drawbacks of PSCs

PSCs are faced with some challenges such as poor stability, lead toxicity, and hysteresis in *J-V* measurements. Among these issues, the stability of PSCs has been pinpointed as one of the most challenging pitfalls. In Niu et al. review paper, they identified oxygen and moisture, ultra-violet (UV) light, solution processing and temperature as the key issues causing degradation in perovskite film [97]. They reported that oxygen together with moisture could lead to irreversible degradation of $CH_3NH_3PbI_3$ as shown in the reactions below.

$$CH_3NH_3PbI_3\,(s) \rightleftharpoons PbI_2\,(s) + CH_3NH_3I\,(aq) \tag{1.17}$$

$$CH_3NH_3I\,(aq) \overset{H_2O}{\rightleftharpoons} CH_3NH_2\,(aq) + HI\,(aq) \tag{1.18}$$

$$4HI\,(aq) + O_2\,(g) \rightleftharpoons 2I_2\,(s) + 2H_2O\,(l) \tag{1.19}$$

$$2HI\,(aq) \overset{\text{light}}{\rightleftharpoons} H_2\,(g) + I_2(s) \tag{1.20}$$

It was found that the absorption of the $TiO_2/CH_3NH_3PbI_3$ film between 530 nm and 800 nm greatly decreased after exposure to air with a humidity of 60% at 35ºC for 18 h. The group further confirmed the degradation of the perovskite film by comparing XRD patterns before and after exposure to moisture [97]. Contrary to Niu et al. report, Kamat and coworkers found that the reaction of $CH_3NH_3PbI_3$ with H_2O leads to the formation of a hydrate phase, such as $(CH_3NH_3)_4PbI_6{\cdot}2H_2O$, in addition to PbI_2 [98]. Later Leguy et al. suggested that the crystal structure formed after the degradation is a different hydrate phase of $CH_3NH_3PbI_3{\cdot}H_2O$ and proposed that the intermediate $CH_3NH_3PbI_3{\cdot}H_2O$ further decompose into $(CH_3NH_3)_4PbI_6{\cdot}2H_2O$ and PbI_2 phases [99,100]. These conflicting findings further suggest that the degradation mechanism of PSCs is not fully understood. In order to improve the PSCs stability, several approaches have been proposed [101-105]. Among these approaches is the introduction of CH_3NH_3Br into the chemical structure of the unstable $CH_3NH_3PbI_3$ [97, 106].

Surprisingly, the device with CH_3NH_3Br showed good stability after exposure to 55% humidity for 20 days with high PCE [107]. Niemann et al. found that the replacement of an organic ligand CH_3NH_3I with an alkali metal such as Cesium (Cs) or Rubidium (Rb) can improve the stability of PSCs [108, 109]. Tai et al. reported improved stability for $CH_3NH_3PbI_{3-x}(SCN)_x$ compared to $CH_3NH_3PbI_3$ [110]. Karunadasa and co-workers reported that the two-dimensional (2D) hybrid perovskite $(PEA)_2(MA)_2[Pb_3I_{10}]$ (PEA = $C_6H_5(CH_2)_2NH_3^+$, MA = $CH_3NH_3^+$) as light-absorber in PSCs can improve stability [111].

Another critical issue is the toxic heavy metal (Pb) contained in PSCs. To address this issue, significant efforts have been made to fabricate lead-free PSCs. In 2014, Kanatzidis and co-workers reported the first attempt using the lead-free perovskite of methylammonium tin iodide ($CH_3NH_3SnI_3$) as the light-absorbing material to fabricate solution-processed solid-state photovoltaic devices, which exhibited a PCE of 5.23% [112]. In an attempt to improve the PCE of $CH_3NH_3SnI_3$ PSCs, the chemical reaction of iodide with bromide enabled the efficient energetic tuning of the band structure of the perovskites, resulting to a PCE of 5.8% [112]. It is worth mentioning that $CH_3NH_3SnI_3$ PSCs suffers from poor atmospheric stability and PCEs. This poor performance is attributed to the p-type doping via Sn^{2+} oxidation induced during the fabrication process [112]. To improve the performance of $CH_3NH_3SnI_3$ PSCs, tin fluoride (SnF_2) was added to $CH_3NH_3SnI_3$ to efficiently turn the $CH_3NH_3SnI_3$ into Sn^{2+}-rich material that can suppress the formation of Sn vacancies [113]. Another strategy was to introduce hydrazine into $CH_3NH_3SnI_3$ which induced the suppression of Sn^{4+} formation and resulting in improved carrier lifetime and reduced defect- and trap-induced recombination in Sn-based perovskite film [114]. These techniques led to substantial improvement in the performance of $CH_3NH_3SnI_3$-based PSCs. Also, significant efforts have been made to develop perovskite derivatives by the substitution of Pb with other metals such as germanium (Ge), bismuth (Bi), antimony (Sb) and so on [106,102]. However, their performance is still deficient compared to the Sn-based PSCs.

Pertaining the Pb-based devices, it has been estimated that upon dissolution of perovskite layer of a module with the one-meter square area, the impact would not be disastrous due to the relatively small amount (<1g) of lead contained [106,115]. Furthermore, proper device encapsulation could limit the Pb leakage during the cell operation, and appropriate end-of-life disposal could further reduce environmental effects of Pb [106, 116].

Another severe drawback of PSCs is the anomalous hysteresis in *J–V* curves, which is the difference in the current measured in the forward and reverse scanning directions. Snaith and his co-workers in 2014 observed for the first time anomalous hysteresis in PSCs [117]. It was found that the *J–V* measurements strongly depend on the voltage sweep rate and scan direction (forward and reverse voltage scanning, i.e., from short-circuit to open circuit, and from open circuit to short-circuit, respectively), which becomes more severe as the scan rate is slowed down [117]. In their studies, three types of PSCs architectures: (i) planar heterojunction solar cells, (ii) perovskite-sensitized solar cells fabricated on mesoporous TiO_2, and (iii) meso-superstructured solar cells (MSSCs) with Al_2O_3 scaffold were employed to unravel the origin of hysteresis. Furthermore, it was found that hysteresis predominantly arises from the perovskite absorber in the solar cell. Also, the device architectures and contact materials, including p- and n-type contacts can determine the degree of hysteresis [117]. To shed more light on their findings, Snaith and his co-workers further hypothesized three possible origins of hysteresis: (i) trapping and detrapping of charge carriers within the perovskites, (ii) ferroelectric properties of the perovskite of the materials, and (iii) interstitial defects in the perovskite caused by ions migration [117]. Later in 2014, Park and co-workers reported that capacitive characteristics and crystal size of $CH_3NH_3PbI_3$ are found to influence *J–V* hysteresis [118]. It was found that the *J–V* hysteresis is alleviated as crystal size increases. Interestingly, the inverted planar structure PSCs with fullerene as ETL has shown negligible hysteresis [65,70, 119-121]. The fullerene can penetrate or diffuse into the perovskite layer through the grain boundaries during spin-coating and annealing [121, 122]. Moreover, the fullerene interacts with the mobile ions in the perovskite to form a fullerene halide radical [110], which stabilizes the electrostatic properties of the perovskites, mitigates the ionic movement in the perovskites, and thus resulting in negligible hysteresis [121-124].

1.4 Objective of study

Renewable and clean energy supplies are indispensable for sustainable economic development, environmental safety, and the mitigation of global warming. Among various renewable energy technologies, solar cells are probably the most promising alternative to conventional fossil fuels. Recently, solar cells based on organic-inorganic perovskite light-absorbing materials have attracted considerable attention among the photovoltaic research community due to their low fabrication cost and high PCEs. In PSCs, the light-absorbing layer (perovskite), which is usually sandwiched between the ETL and HTL is one of the most significant components, suggesting that it must be high-quality to guarantee high PCEs. Since perovskite materials are moisture sensitive and unstable when exposed to high humid environments, they are usually fabricated using humidity control facilities such as glovebox and deposition machines. The use of such expensive vacuum facilities would significantly increase its production cost and energy payback time thereby hampering its commercialization. It is believed that PSCs would be more attractive and cost-effective if it can be fabricated in the air like the DSSCs. Moreover, the PCE strongly depends on the fabrication method; it is essential to efficiently and meticulously study the device fabrication methods under different condition for the future application. In this thesis, we proposed simple and efficient ways to fabricate high-quality perovskite films with improved uniformity for high-performance planar PSCs under ambient air condition.

1.5 Composition of thesis

In this thesis, we proposed novel device fabrication methods and evaluated the device characteristics. This paper consists of 6 chapters. Chapter 1 shows the research background of solar cells and PSCs. Chapters 3 to 5 is the research content of this thesis, and Chapter 6 is the summary.

Chapter 1 describes the importance of solar energy and why it is preferable to the energy from fossil fuel. It further introduces solar cell, types of solar cells as well as the fundamental theories and physics of solar cell. The latter part of chapter 1 presents a general review on perovskite as an excellent light-absorbing material for solar cells. It also covers further discussions on PSCs such as the development of PSCs, device architectures, energy band diagram of a typical PSC, deposition methods of metal halide perovskite thin films and drawbacks of PSCs.

Chapter 2 introduces the experimental methods, device fabrication and evaluation methods used in this thesis.

Chapter 3 proposes a simple and efficient way to fabricate PSCs**.** The PSC was fabricated using two-step spin-coating method together with air-assisted flow under ambient air condition. The correlations between the films prepared with and without airflow and device performance are systematically investigated.

Chapter 4 describes planar PSCs fabricated by a simple one-step solution process and antisolvent bath (ASB) methods under ambient air condition. Diethyl ether (DEE), which has a low boiling point and no solubility or reactivity with the perovskite precursors, was used to extract the *N*-methyl-2-pyrrolidone (NMP) and γ-butyrolactone (GBL) solvents from the spin-coated solution film. This enabled a uniform, highly smooth and glossy perovskite film. The morphology and grain growth of the resultant perovskite film were further improved by solvent annealing (SA) approach. Perovskite films treated with SA, thermal annealing (TA) and without treatment were systematically investigated. Device containing films prepared with SA, TA and without annealing were fabricated and analyzed. This work highlights the importance of SA for perovskite film prepared by a one-step solution process and ASB method and offers a simple and attractive way to fabricate high-performance PSCs under ambient air condition.

Chapter 5 introduces planar PSCs based on low-temperature amorphous tungsten oxide (WO_x)/fullerene C_{60} ETLs. The WO_x/C_{60} ETLs were fabricated using solution-process. The perovskite film was deposited using one-step solution process and ASB method in ambient air, further suggesting the robustness of this method. The C_{60} layer is incorporated to suppress the inherent charge recombination at the perovskite/WO_x interface. The effect of incorporating C_{60} interlayer on the device performance was systematically investigated. This work demonstrates that WO_x/C_{60} ETLs can work together to enhance the performance of PSCs. Moreover, a potential low-temperature approach.

Chapter 6 summarizes the issue discussed in this thesis and its significance, and the scope of future research.

1.6 References

1) V. Scott, S. Haszeldine, S. Tett, A. Oschlies, 'Fossil fuels in a trillion tonne world.' Nature Climate Change, 5 (2015), 419–423.

2) M. Beccali, M. Cellura, M. Mistretta, "Environmental effects of energy policy in sicily: The role of renewable energy," Renew. Sustain. Energy Rev., 11 (2007) 282–298.

3) D. S. Ginley, D. Cahen, Fundamentals of Materials for Energy and Environmental Sustainability, Cambridge University Press, Cambridge, UK, (2011).

4) H. Lund, "Renewable Energy Strategies for sustainable development," Energy, 32 (2007) 912–919.

5) https://en.wikipedia.org/wiki/World_energy_consumption#cite_note-iea16-12.

6) D. T. Ho, J. Frunt, J. M. A. Myrzik, Photovoltaic energy in power market. In: IEEE energy market 6th international conference on the European; (2009), 1–5.

7) F. Dincer, The analysis on photovoltaic electricity generation status, potential and policies of the leading countries in solar energy, Renewable and Sustainable Energy Reviews 15 (2011), 713–720.

8) A. Simms, "It is time to plug into renewable power." New Scientist, 183, (2004), 18-19.

9) C. K. Frederik, Polymer Photovoltaics a Practical Approach, SPIE, (2008).

10) S. L. Nathan, G. N. Daniel, Powering the planet: Chemical challenges in solar energy utilization, Proceedings of the National Academy of Sciences. 103 (2006) 15729–15735.

11) United Nations Development Program (2003) World Energy Assessment Report: Energy and the Challenge of Sustainability (United Nations, New York).

12) T. Markvart, L. Castaner, Solar Cells: Materials, Manufacture and Operation, Elsevier, Oxford, (2005).

13) https://www.nrel.gov/pv/assets/images/efficiency-chart.png.

14) M. Tao, Inorganic Photovoltaics Solar Cells: Silicon and Beyond, Electrochem. Soc. Interface 17(2008), 30-35.

15) B. Holger, Solar Cells Based on Colloidal Nanocrystals, Springer, (2014).

16) C. A. Gueymard, D. Myers, K. Emery, Proposed Reference Irradiance Spectra for Solar Energy Systems Testing Sol. Energy 73, (2002), 443-467.

17) C. Kittel, Introduction to Solid State Physics, 8th edn., Wiley, New York, (2005).

18) J. Klaus, I. Olindo, H. M. S. Arno, A. C. M. M. Rene, S. Van, Z. Miro, Solar Energy Fundamentals, Technology System, Delft University of Technology, (2014).

19) W. J. Yang, Z. Q. Ma, X. Tang, C. B. Feng, W.G. Zhao, P.P Shi, Internal Quantum Efficiency for Solar Cells, Solar Energy 82 (2008), 106-110.

20) Y. Zusing, C. Chia-Ying, R. Prathik, C. Huan-Tsung, Quantum Dot-Sensitized Solar Cells Incorporating Nanomaterials, Chem. Commun., 47 (2011), 9561-9571.

21) T. Mori, D. Sato, T. Egami, V. O. Eze, Improvement of Photovoltaic Properties for Unmodified Fullerene C_{60}–Based Polymer Solar Cells by Addition of Fusible Fullerene, J. Photopolym. Sci. Technol., 4 (2017), 501–506.

22) M. D. Graef and M. McHenry, structure of materials: an introduction to crystallography, diffraction and symmetry, Cambridge University Press, (2007).

23) M. A Pena, J. L.G Fierro, Chemical Structures and Performance of Perovskite Oxides Chem. Rev. 101 (2001), 1981-2017.

24) Q. Chen, N. De Marco, Y. Micheal Yang, et al., under the spotlight: The organic–inorganic hybrid halide perovskite for optoelectronic applications, Nano Today, (2015)

25) C.K, Crystal structure and photoconductivity of caesium plumbohalides, Nature 182 (1958), 1436

26) D. B Mitzi, Synthesis, Structure, and Properties of Organic-Inorganic Perovskites and Related Materials, Prog. Inorg. Chem. 48 (2007), 1-121

27) X. Zhao, N.-G. Park, Stability Issues on Perovskite Solar Cells, Photonics 2 (2015), 1139-1151

28) Y. Chen, M. He, J. Peng, Y. Sun, Z. Liang, Structure and Growth Control of Organic-Inorganic Halide Perovskite for Optoelectronic: From Polycrystalline Films to Single Crystals, Adv. Sci. 3, (2016), 1500392.

29) T. C. Sum, N. Mathews, Advancements in perovskite solar cells: photophysics behind the photovoltaics, Energy Environ. Sci. 7, (2014), 2518

30) V. M. Goldschmidt, Crystal structure and chemical correlation, Ber. Dtsch. Chem. 60 (1927), 1263-1268

31) M. Johnsson, P. Lemmens, Handbook of Magnetism and Advance Magnetic Materials, John Wiley & Sons, Ltd., (2007).

32) C. Li, X. Lu, W. Ding, L. Feng, Y. Gao, Z. Guo, Formability of ABX_3 (X=F, Cl, Br, I) halide perovskites, Acta Crystallogr. Sect. B: Struct. Sci. 64 (2008), 702-707.

33) Y. Zhao, K. Zhu, Organic–inorganic hybrid lead halide perovskite for optoelectronic and electronic applications, Chem. Soc. Rev., 45, (2016), 655-689.

34) G. Kieslich, S. Sun, A. K. Cheetham, An extended Tolerance Factor approach for organic–inorganic perovskites, Chem. Sci., 6 (2014), 3430-3433.

35) D. Weber, CH3NH3PbX3, ein Pb(II)-System mit kubischer Perowskitstruktur Inst. Anorg. Chem. Univ. Stutt. 33b (1978) 1443-1445.

36) F. Brivio, A. B Walker, A. Walsh, Structural and electronic properties of hybrid perovskites for high-efficiency thin-film photovoltaics from first-principles, APL Mater. 1 (2013), 042111.

37) C. C Stoumpos, C. D. Malliakas, M.G. Kanatzidis, Semiconducting Tin and lead iodide perovskites with organic cations: phase transitions, high mobilities, and near-infrared photoluminescent properties, Inorg. Chem. 52 (2013), 9019-9038.

38) A. Kojima, k. Teshima, T. Miyasaka, Y. Shirai, Proc. 210th ECS Meeting, ECS, (2006)

39) A. Kojima, K. Teshima, Y. Shirai, T. Miyasaka, Organometal halide perovskites a visible-light sensitizers for photovoltaic cells, J. Am. Chem. Soc. 131 (2009), 6050-6051

40) J. -H. Lm, C. -R. Lee, J. -W. Lee, S. W. Park, N. -G. Park, 6.5% efficient perovskite quantum-dot-sensitized solar cells, Nanoscale 3 (2011), 4088-4093

41) H. -S. Kim, C. -R. Lee, J. -H. Lm, K. -B. Lee, T. Moehl, A. Marchioro et al., Lead Iodide Perovskite Sensitized All-Solid State Submicron Thin Film Mesoscopic Solar Cell with Efficiency Exceeding 9%, Sci. Rep. 2 (2012), 591.

42) M. M. Lee, J. Teuscher, T. Miyasaka, T. N. Murakami and H. J. Snaith, Efficient Hybrid Solar Cells Based on Meso-Superstructured Organometal Halide Perovskite, Science, 338, (2012), 643-647

43) J. Burschka, N. Pellet, S.-J. Moon, R. Humphry-Baker, P. Gao, M. K. Nazeeruddin, M. Grätzel, Sequential deposition as a route to high-performance perovskite-sensitized solar cells, Nature 499, (2013) 316

44) M. Z. Liu, M. B. Johnston, H. J. Snaith, Efficient planar heterojunction perovskite solar cells by vapor deposition, Nature 501 (2013) 395-398

45) https://www.nrel.gov/pv/assets/images/efficiency-chart.png

46) J. H. Noh, S. H. Im, J. H. Heo, T. N. Mandal, S. I. Seok, Chemical Management for Colorful, Efficient, and Stable Inorganic Organic Hybrid Nanostructured Solar Cells, Nano lett.,13, (2013) 1764

47) C. Wehrenfennig, G. E. Eperon, M. B. Johnston, H. J. Snaith, and L. M. Herz, High Charge Carrier Mobilities and Lifetimes in Lifetimes in Organolead Trihalide Perovskites, Adv. Mater. 26, (2014)1584.

48) S. D. Stranks, G. E. Eperon, G. Grancini, C. Menelaou, M. J. Alcocer, T. Leijtens, L. M. Herz, A. Petrozza, and H. J. Snaith, Electron-Hole Diffusion Lengths Exceeding 1 Micrometer in an Organometal Trihalide Perovskite Absorber, Science 342, (2013) 341-344.

49) G. Xing, N. Mathews, S. Sun, S. S. Lim, Y. M. Lam, M. Gratzel, S. Mhaisalkar, and T. C. Sum, Long-Range Balance Electron-and Hole-Transport Lengths in Organic-Inorganic $CH_3NH_3PbI_3$, Science 342, (2013)344-347.

50) V. D'Innocenzo, G. Grancini, M. J. P. Alcocer, A. R. S. Kandada, S. D. Stranks, M. M. Lee, G. Lanzani, H. J. Snaith, and A. Petrozza, Exciton versus free charges in organo-lead tri-halide perovskites, Nat. Commun. 5, (2014)3586.

51) J. Qiu, Y. Qiu, K. Yan, M. Zhong, C. Mu, H. Yan, S. Yang, All-Solid-State Hybrid Solar Cells Based on a New Organometal Halide Perovskite Sensitizer and one-dimensional TiO_2 Nanowire Arrays, Nanoscale, 5, (2013) 3245-3248.

52) E. Edri, S. Kirmayer, D. Cahen, G. Hodes, High Open-Circuit Voltage Solar Cells Based on Organic-Inorganic Lead Bromide Perovskite, J. Phys. Chem. Lett., 2013, 897-902

53) D. Bi, G. Boschloo, S. Schwarzmuller, L. Yang, E. M. Johansson, A. Hagfeldt, Efficient and Stable CH3NH3PbI3-sensitized ZnO Nanorod Array Solid-State Solar Cells, Nanoscale, 5, (2013) 11686-11691.

54) J. H. Heo, S. H. Im, J.H. Noh, T.N. Mandal, C.-S. Lim, J. A. Chang, Y. H. Lee, H.-J. Kim, A. Sarkar, et al., Efficient inorganic-organic hybrid heterojunction solar cells containing perovskite compound and polymeric hole conductors, Nat. Photonics, 7 (2013) 486-491.

55) N. J. Jeon, J. H. Noh, W. S. Yang, Y. C. kim, S. Ryu, J. Seo, S. I. Seok, Solvent engineering for high-performance inorganic–organic hybrid perovskite solar cells, Nature, 517 (2015) 476-480.

56) T. Leijtens, B. Lauber, G. E. Eperon, S. D. Stranks, H. J. Snaith, The Importance of Perovskite Pore Filling in Organometal Mixed Halide Sensitized TiO_2-Based Solar Cells, J. Phys. Chem. Lett., 5 (2014) 1096-1102.

57) T. –B. Song, Q. Chen, H. Zhou, C. Jiang, H. –H. Wang, et al., Perovskite solar cells: film formation and properties, J. Mater. Chem., A, 3 (2015) 9032-9050.

58) J.-H. Im, I.-H. Jang, N. Pellet, M. Grätzel, N.-G. Park, Growth of $CH_3NH_3PbI_3$ cuboids with controlled size for high-efficiency perovskite solar cells, Nat. Nanotechnol., 9 (2014) 927-932.

59) N. J. Jeon, H. G. Lee, Y.C. Kim, J. Seo, J. H. Noh, J. Lee, S. I. Seok, *o*-Methoxy Substituents in Spiro-OMeTAD for Efficient Inorganic–Organic Hybrid Perovskite Solar Cells, J. Am. Chem. Soc., 136 (2014) 7837-7840.

60) A. Abate, M. Saliba, D. J. Hollman, S. D. Stranks, K. Wojciechowski, R. Avolio, G. Grancini, A. Petrozza, H. J. Snaith, Supramolecular Halogen Bond Passivation of Organic−Inorganic Halide Perovskite Solar Cells, Nano Lett., 14 (2014) 3247-3254.

61) G. E. Eperon, V. M. Burlakov, P. Docampo, A. Goriely, H. J. Snaith, Morphological Control for High Performance, SolutionProcessed Planar Heterojunction Perovskite Solar Cells, Adv. Funct. Mater.,24 (2014**)**, 151–157.

62) H. J. Snaith, A. Abate, J. M. Ball, G. E. Eperon, T. Leijtens, N. K. Noel, S. D. Stranks, J. T.-W. Wang, K. Wojciechowski, W. Zhang, Anomalous Hysteresis in Perovskite Solar Cells, J. Phys. Chem. Lett. 5 (2014), 1511−1515.

63) J. Y. Jeng, Y. F. Chiang, M. H. Lee, S. R. Peng, T. F. Guo, P. Chen, T. C. Wen, $CH_3NH_3PbI_3$ perovskite/fullerene planar-heterojunction hybrid solar cells. Adv. Mater. 25 (2013) 3727-3732.

64) P. Docampo, J. M. Ball, M. Darwich, G. E. Eperon, H. J. Snaith, Efficient organometal trihalide perovskite planar-heterojunction solar cells on flexible polymer substrates. Nat. Commun. 4 (2013), 2761.

65) J. You, Y. Yang, Z. Hong, T. B. Song, L. Meng, Y. Liu, C. Jiang, H. Zhuo, W. H. Chang, G. Li, Y. Yang, and Moisture assisted perovskite film growth for high performance solar cells. Appl. Phys. Lett. 105 (2014) 183902.

66) Z. Xiao, C. Bi, Y. Shao, Q. Dong, Q. Wang, Y. Yuan, C. Wang, Y. Gao, J. Huang, Efficient, high yield perovskite photovoltaic devices grown by interdiffusion of solution-processed precursor stacking layers. Energy Environ. Sci. 7 (2014) 2619-2623.

67) J. Seo, S. Park, Y. C. kim, N. J. Jeon, J. H. Noh, S. C. Yoon, S. I. Seok, Benefits of very thin PCBM and LiF layers for solution-processed p-i-n perovskite solar cells. Energy Environ. Sci. 7 (2014), 2642-2646.

68) Z. Xiao, Q. Dong, B. Cheng, Y. Shao, Y. Yuan, J. Huang, SolventAnnealing of Perovskite-Induced Crystal Growth for Photovoltaic Device Efficiency Enhancement. Adv. Mater. 26 (2014), 6503-6509.

69) J. Y. Jeng, K. C. Chen, T. Y. Chiang, P. Y. Lin, T. D. Tsai, Y. C. Chang, T. F. Guo, P. Chen, T. C. Wen, J. Y. Hsu, Nickel oxide electrode interlayer in $CH_3NH_3PbI_3$ perovskite/PCBM planar-heterojunction hybrid solar cells. Adv. Mater. 26 (2014) 4107-4113

70) L. Meng, J. You. T.-F. Guo, Y. Yang, Recent Advances in the Inverted Planar Structure of Perovskite Solar Cells. Acc. Chem. Res. 49 (2016), 155−165.

71) C. Zuo, H. J. Bolink, H. Han, J. Huang, D. Cahen, L. Ding, Advances in Perovskite Solar Cells. Adv. Sci., 3 (2016) 1500324.

72) W. –J. Yin, T. Shi, Y. Yan, Unique Properties of Halide Perovskites as Possible Origins of the Superior Solar Cell Performance, Adv. Mater., 26 (2014) 4653-4658.

73) W. –J. Yin, T. Shi, Y. Yan, Unusual defect physics in $CH_3NH_3PbI_3$ perovskite solar cell absorber, Appl. Phys. Lett., 104, (2014) 063903.

74) C. Motta, F. El-Mellouhi, S. Kais, N. Tabet, F. Alharbi, S. Sanvito, Revealing the role of organic cations in hybrid halide perovskite $CH_3NH_3PbI_{3,}$ Nat. Commun., 6 (2015) 7026.

75) E. Mosconi, A. Amat, M. K. Nazeeruddin, M. Grätzel, F. De Angelis, First-Principles Modeling of Mixed Halide Organometal Perovskites for Photovoltaic Applications, J. Phys. Chem. C., 117 (2013) 13902-13913.

76) Y. H Chang, C. H. Park, First-Principles Study of the Structural and the Electronic Properties of the Lead-Halide-Based Inorganic-Organic Perovskites (CH3NH3)PbX3 and CsPbX3 (X = Cl, Br, I), J. Korean Phys. Soc. 44 (2004) 889-893.

77) P. Umari, E. Mosconi, F. De Angelis,Relativistic GW calculations on $CH_3NH_3PbI_3$ and $CH_3NH_3SnI_3$ Perovskites for Solar Cell Applications, Sci. Rep. 4 (2014) 4467.

78) T. Umebayashi, K. Asai, T. Kondo, A. Nakao,Electronic structures of lead iodide based low-dimensional crystals, Phys. Rev. B 67 (2003) 155405.

79) T. C. Sum, N. Mathew, Advancements in Perovskite Solar Cells: photophysics behind the photovoltaics. Energy Environ. Sci., 7 (2014) 2518-2534.

80) N. Marinova, S. Valero, J. Luis Delgado, Organic and perovskite solar cells: Working principles, material and interfaces. Journal of Colloid and Interface Science 488 (2017) 373-389.

81) A. Marchioro, J. Teuscher, D. Friedrich, M. Kunst, R. Van de Krol, T. Moehl, M. Grätzel, J. –E. Moser, Unravelling the mechanism of photoinduced charge transfer process in lead iodide perovskite solar cells, Nature Photonics 8 (2014) 250–255.

82) A. Ng, Z. W. Ren, Q. Shen, S. H. Cheung, H. C. Gokkaya, G. X. Bai, J. C. Wang, et al., Efficiency enhancement by defect engineering in perovskite photovoltaic cells prepared using evaporated PbI_2/CH_3NH_3I multilayers, J. Mater. Chem. A 3 (2015) 9223-9231.

83) C.-W. Chen, H.-W. Kang, S.-Y. Hsiao, P. –F. Yang, K. –M. Chiang, H. –W. Lin, Efficient and uniform planar-type perovskite solar cells by simple sequential vacuum deposition, Adv. Mater. 26 (2014) 6647-6652.

84) Q. Chen, H. P. Zhou, Z. R. Hong, S. Luo, H.-S. Duan, H.-H. Wang, Y. S. Liu, G. Li, Y. Yang, Planar heterojunction perovskite solar cells via vapor-assisted solution process, J. Am. Chem. Soc. 136 (2014) 622-625.

85) J. M. Ball, M. M. Lee, A. Hey, H. J. Snaith, Low-temperature processed meso-superstructured to thin-film perovskite solar cells, Energy Environ. Sci. 6 (2013) 1739.

86) H. Zhou, Q. Chen, G. Li, S. Luo, T. –b. Song, H. –S. Duan, Z. Hong, J. You, Y. Liu, Y. Yang, Interface engineering of highly efficient perovskite solar cells, Science 345 (2014) 542.

87) K. Wojciechowski, M. Saliba, T. Leijtens, A. Abate, H. J. Snaith, Sub 150 °C Processed Meso-superstructured Perovskite Solar Cells with Enhanced Efficiency Energy Environ. Sci. 7 (2014) 1142.

88) J. H. Heo, H. J. Han, D. kim, T. K. Ahn, S. H. Im, Hysteresis-less inverted CH3NH3PbI3 planar perovskite hybrid solar cells with 18.1% power conversion efficiencyEnergy Environ. Sci. 8 (2015) 1602-1608.

89) K. Liang, D. B. Mitzi, M. T. Prikas, Synthesis and Characterization of Organic−Inorganic Perovskite Thin Films Prepared Using a Versatile Two-Step Dipping Technique, Chem. Mater., 10 (1998) 403-411.

90) Y. Zhao, K. Zhu, Three-step sequential solution deposition of PbI_2-free $CH_3NH_3PbI_3$perovskite,J. Mater. Chem. A, 3 (2015) 9086-9091.

91) H. A. Harms, N. Tetreault, N. Pellet, M. Bensimon, M. Grätzel, Mesoscopic photosystems for solar light harvesting and conversion: facile and reversible transformation of metal-halide perovskites, Faraday Discuss., 176 (2014) 251-269.

92) J.-H. Im, H.-S. Kim, N.-G. Park, Morphology-photovoltaic property correlation in perovskite solar cells: One-step versus two-step deposition of $CH_3NH_3PbI_3$, APL Mater. 2(2014), 081510.

93) W. Zhu, T. Yu, F. Li, C. Bao, H. Gao, Y. Yi, J. Yang, G. Fu, X. Zhuo, Z. Zuo, A facile, solvent vapor–fumigation-induced, self-repair recrystallization of $CH_3NH_3PbI_3$ films for high-performance perovskite solar cells, Nanoscale, 7 (2015), 5427-5434.

94) J. Lian, Q. Wang, Y. Yuan, Y.Shao, J. Huang, Organic solvent vapor sensitive methylammonium lead trihalide film formation for efficient hybrid perovskite solar cellsJ. Mater., Chem. A.,3 (2015), 9146-9151.

95) B. Lei, V. O. Eze, T. Mori, High-performance $CH_3NH_3PbI_3$perovskite solar cells fabricated under ambient conditionswith high relative humidity.

96) V. O. Eze, B. Lei, T. Mori, Air-assisted flow and two-step spin-coating for highly efficient CH3NH3PbI3 perovskite solar cells, Jpn. J. Appl. Phys. 55 (2016), 02BF08.

97) G. Niu, X. Guo, L. Wang, Review of recent progress in chemical stability of perovskite solar cells, J. Mater. Chem. A, 3 (2015),8970-8980.

98) J. A. Christians, P. A. M. Herrera, and P. V. Kamat, Transformation of the Excited State and Photovoltaic Efficiency of $CH_3NH_3PbI_3$ Perovskite upon Controlled Exposure to Humidified Air, J. Am. Chem. Soc. 137 (2015), 1530-1538.

99) A. M. A. Leguy, Y. Hu, M. Campoy-Quiles, M. I. Alonso, O. J. Weber, P. Azarhoosh, M. van Schilfgaarde, M. T. Weller, T. Bein, J. Nelson, P. Docampo, and P. R. F. Barnes, Reversible Hydration of $CH_3NH_3PbI_3$ in Films, Single Crystals, and Solar Cells, Chem. Mater. 27 (2015), 3397-3407.

100) M. Shirayama, M. Kato, T. Miyadera, T. Sugita, T. Fujiseki, S. Hara, H. Kadowaki, D. Murata, M. Chikamatsu, H. Fujiwara, Degradation mechanism of CH3NH3PbI3 perovskite materials upon exposure to humid air, J. Appl. Phys. 119 (2016),115501.

101) A. Mei, X. Li, L. Liu, Z. Ku, T. Liu, Y. Rong, M. Xu, M. Hu, J. Chen, Y. Yang, M. Grätzel, H. Han, A hole-conductor–free, fully printable mesoscopic perovskite solar cell with high stability Science 345 (2014) 295.

102) X. Li, M. I. Dar, C. Yi, J. Luo, M. Tschumi, S. M. Zakeeruddin, M. K. Nazeeruddin, H. Han, M. Grätzel, Improved performance and stability of perovskite solar cells by crystal crosslinking with alkylphosphonic acid ω-ammonium chlorides, Nat. Chem. 7 (2015) 703-711.

103) J. B. You, L. Meng, T. –B. Song, T. –F. Guo, Y. M. Yang, W. –H. Chang, Z. R. Hong, H. J. Chen, H. P. Zhou, Q. Chen, Y. S. Liu, N. De Marco, Y. Yang, Improved air stability of perovskite solar cells via solution-processed metal oxide transport layer, Nat. Nanotechnol. 11 (2016) 75-81

104) Z. Y. Liu, B. Sun, T. L. Shi, Z. R. Tang, G. L. Liao, Enhanced photovoltaic performance and stability of carbon counter electrode based perovskite solar cells encapsulated by PDMS, J. Mater. Chem. A 4 (2016) 10700-10709.

105) S. N. Habisreutinger, T. Leijtens, G. E. Eperon, S. D. Stranks, R. J. Nicholas, H. J. Snaith, Carbon Nanotube/Polymer Composites as a Highly Stable Hole Collection Layer in Perovskite Solar Cells, Nano Lett., 14 (10) (2014), 5561–5568.

106) A. B. Djurisic, F. Z. Liu, H. W. Tam, M. K. Wong, A. Ng, C. Surya, W. Chen, Z. B. He, Perovskite solar cells- an overview of critical issues, Progress in Quantum Electronics, 53 (2017) 1-37.

107) J. H. Noh, S. H. Im, J. H. Heo, T. N. Mandal and S. I. Seok, Chemical Management for Colorful, Efficient, and Stable Inorganic−Organic Hybrid Nanostructured Solar CellsNano Lett., 13 (2013), 1764–1769.

108) T. Leijtens, G. E. Eperon, N. K. Noel, S. N. Habisreutinger, A. Petrozza, H. J. Snaith, Stability of metal halide perovskite solar cells, Adv. Energy Mater. 5 (2015) 1500963.

109) R. G. Niemann, L. Gouda, J. G. Hu, S. Tirosh, R. Gottesman, P. J. Cameron, A. Zaban, Cs^+ incorporation into $CH_3NH_3PbI_3$ perovskite: Substitution limit and stability enhancement, J. Mater. Chem. A 4 (2016) 17819-17827.

110) Q. D. Tai, P. You, H. Q. Sang, Z. K. Liu, C. L. Hu, H. L. W. Chan, F. Yan, Efficient and stable perovskite solar cells prepared in ambient air irrespective of the humidity, Nat. Commun., 7 (2016) 381-387.

111) I. C. Smith, E. T. Hoke, D. Solis-Ibarra, M. D. McGehee and H. I. Karunadasa, A Layered Hybrid Perovskite Solar-Cell Absorber with Enhanced Moisture Stability Angew. Chem., Int. Ed., 2014, 53, 11232– 11235.

112) T.-B. Song, T. Yokoyama, S. Aramaki, M. G. Kanatzidis, Performance Enhancement of Lead-Free Tin Based Perovskite Solar Cells with Reducing Atmosphere-Assisted Dispersible Additive, ACS Energy Lett. 2 (2017), 897−903.

113) X. P. Chen, S. Xiang, H.-J. Gong, X.-G. Wei, S.-H. Influence of Defects and Synthesis Conditions on the Photovoltaic Performance of Perovskite Semiconductor CsSnI3. Chem. Mater. 26 (2014), 6068− 6072.

114) T. Yokoyama, T.-B. Song, D. H. Cao, C. C. Stoumpos, S. Aramaki, M. G. Kanatzidis, The Origin of Lower Hole Carrier Concentration in Methylammonium Tin Halide Films Grown by Vapor-Assisted Solution Process. ACS Energy Lett. 2 (2017) 22−28.

115) B. Hailegnaw, S. Kirmayer, E. Edri, G. Hodes, D. Cahen, Rain on methylammonium lead iodide based perovskites: Possible environmental effects of perovskite solar cells, J. Phys, Chem. Lett. 6 (2015) 1543-1547.

116) S. T. Williams, A. Rajagopal, C.-C. Chueh, A. K. –Y. Jen, Current Challenges and Prospective Research for Upscaling Hybrid Perovskite Photovoltaics, J. Phys. Chem. Lett. 7 (2016) 811-819.

117) H. J. Snaith, A. Abate, J. M. Ball, G. E. Eperon, T. Leijtens, N. K. Noel, S. D. Stranks, J. T. –W. Wang, K. Wojciechoeski, W. Zhang, Anomalous Hysteresis in Perovskite Solar Cells, J. Phys. Chem. Lett. 5 (2014), 1511-1515.

118) H. –S. Kim, N. –G. Park, Parameters Affecting *I–V* Hysteresis of CH3NH3PbI3 Perovskite Solar Cells: Effects of Perovskite Crystal Size and Mesoporous TiO_2 Layer, J. Phys. Chem. Lett. 5 (2014) 2927-2934.

119) J. You, Z. Hong, Y. Yang, Q. Chen, M. Cai, T. B. Song, C. C. Cheng, S. Lu, Y. Liu, H. Zhou, Y. Yang, Low-temperature solution-processed perovskite solar cells with high efficiency and flexibility. ACS Nano 8 (2014) 1674-1680.

120) J. You, L. Meng, T. B. Song, T. F. Guo, Y. Yang, W. H. Chang, Z. Hong, H. Chen, H. Zhou, Q. Chen, Y. Liu, N. De Marco, Y. Yang, Improved air-stability of perovskite solar cells via solution-processed metal oxide transport layers. Nat. Nanotechnol., 11 (2016) 75-81

121) Y. Shao, Z. Xiao, C. Bi, Y. Yuan, J. S. Huang, Origin and elimination of photocurrent hysteresis by fullerene passivation in CH3NH3PbI3 planar hetero-junction solar cells. Nat. Commun. 5 (2014), 5784.

122) S. D. Stranks, H. J. Snaith, Metal-halide perovskites for photovoltaic and light-emitting devices. Nat. Nanotechnol. 10 (2015), 391−402.

123) J. Xu, A. Buin, A. Ip, H. Li, W. Voznyy, O. Comin, R. Yuan, M. Jeon, S. Ning, Z. Mcdowell, J. Kanjanaboos, P. Sun, J. Lan, X. Quan, L. Kim, D. H. Hill, I. G. Maksymovych, P. Sargent, E. H. Perovskite− fullerene hybrid materials suppress hysteresis in planar diodes. Nat. Commun. 6 (2015), 7081.

124) M. D Bastiani, M. Binda, M. Gandini, J. Ball, A. Petrozza, Charge extraction layer investigation for high efficiency and hysteresis-less organo lead halide perovksite solar cell, Proceedings of the MRS Spring Meeting C4.04, (2015).

Chapter 2

Experimental Methods and Characterization

2.1 Materials and reagents

Methylammonium iodide (CH_3NH_3I) was synthesized in accordance with the reported procedures [1]. Fluorine-doped tin oxide (FTO) glass substrates (sheet resistance: 12 Ω/sq.) were purchased from Asahi Glass. Semico-Clean, acetone, isopropanol, tungsten hexachloride (WCl_6; ≥99.9%, Sigma-Aldrich), titanium(IV)isopropoxide (99.0%), ethanol, acetonitrile, dichlorobenzene, dimethyformamide (DMF) (Sigma-Aldrich, 99.8%), *N*-methyl-2-pyrrolidone (NMP; >99%, Sigma-Aldrich), γ-butyrolactone (GBL; >98.5%, Sigma-Aldrich), anhydrous diethyl ether (DEE; >99.0%, Sigma-Aldrich), dimethyl sulfoxide (DMSO; 99.0%, Wako), fullerene C_{60} (>99%, Jilin OLED Material), 2,2′,7,7′-tetrakis(*N*,*N*-di-*p*-methoxyphenylamine)-9,9′-spirobifluorene (Spiro-OMeTAD), and PbI_2 (99.0 %, Sigma-Aldrich) were used without further treatment.

2.2 Fabrication of perovskite solar cells

In this study, the n-i-p planar structure (see section 1.3.7 of chapter 1) was used for the fabrication of perovskite solar cells (PSCs). The entire process except for the deposition of back contact electrode (Au) was carried out by solution process under ambient air condition. In this section, I will mention the fabrication steps of PSCs.

2.2.1 Preparation of working electrode

Fig. 2.1a shows the schematic diagram of the patterned FTO glass substrate. While Fig. 2.1b presents the ultraviolet (UV) ozone treatment equipment. In this thesis, FTO glass substrates were used as the substrate. It was patterned by etching with hydrochloric acid (HCl) and zinc powder and sequentially cleaned with Semico-Clean, ultrahigh purified water, acetone, and isopropanol. The cleaned FTO glass substrate was transferred into the chamber of the UV ozone cleaner (Nippon Laser and Electronics (NLE-UV253)). The chamber was purged by O_2 at 0.2 MPa for 1 min then treated with UV-light for 15 min. After the UV ozone treatment, the chamber was purged by 0.2 MPa N_2 for 1 min to eliminate the remaining ozone [2].

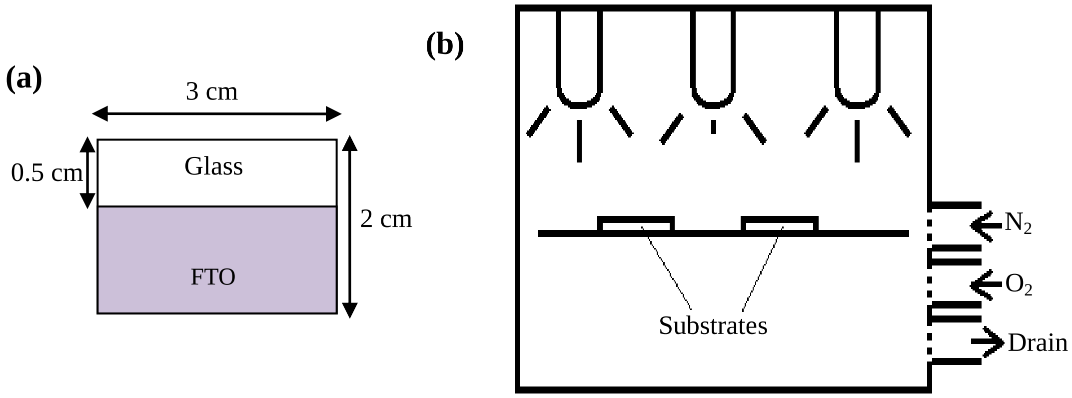

Fig. 2.1 Schematic diagram showing the patterned FTO glass substrate, (b) UV-Ozone treatment equipment [2].

2.2.2 Deposition of compact TiO_2 as an electron transport layer

Fig. 2.2a shows the chemical structure of titanium(IV) isopropoxide (TTIP). Fig. 2.2b describes the fabrication process of the compact TiO_2 electron transport layer (ETL). The compact TiO_2 ETL was prepared by spin-coating a solution of TTIP (1.5 ml) in ethanol (10 ml) and HCl (0.1 ml) onto the cleaned FTO substrates at 3000 rpm for the 20s to form an approximately 50-nm-thick layer. All the samples were moved onto a hot plate and kept at 125 °C for 20 min and then sintered at 500 °C for 30 min (Fig. 2.2b).

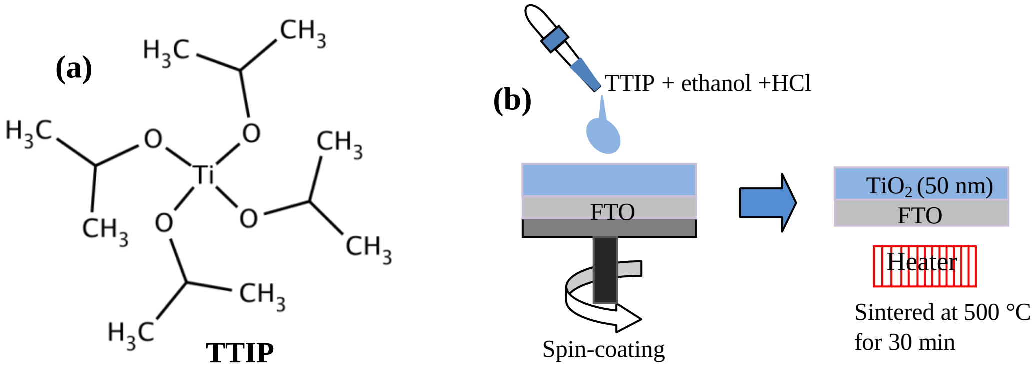

Fig. 2.2 (a) Chemical structure of titanium(IV) isopropoxide. (b) Schematic illustration of the fabrication of compact TiO_2 layer.

2.2.3 Deposition of amorphous tungsten oxide/fullerene C_{60} as electron transport layer

Fig. 2.3 describes the fabrication method of amorphous tungsten (WO_x) and C_{60} fullerene ETLs. The WO_x ETL was prepared by a low-temperature solution process described in a previous report [3]. 0.1 g/mL WCl_6 was dissolved in ethanol and stirred at 50 °C. The solution was spin coated on clean FTO substrates in the air at a spin speed of 3000 rpm for 30 s. The films were subsequently annealed on a hot plate in the atmosphere at 150 °C for 10 min. The thickness of the WO_x film is about 50 nm. WO_x/C_{60} ETLs were prepared by spin coating C_{60} dichlorobenzene (DCB) solutions (15 mg/ml) on WO_x films at a spin speed of 2500 rpm for 30 s. The thicknesses of C_{60} films were controlled by varying the concentration of C_{60} in DCB.

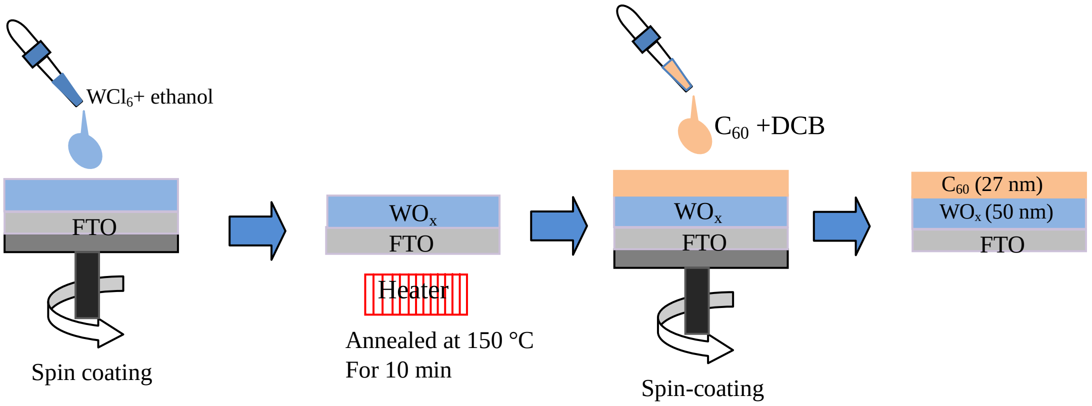

Fig. 2.3 Schematic illustration of the fabrication of WO_x/C_{60} fullerene ETLs

2.2.4 Deposition of perovskite film

The perovskite films were fabricated using solution process method. In chapter 3 of this thesis, the perovskite film was prepared using air-assisted flow and two-step spin-coating method. While in chapter 4 and 5, the perovskite films were prepared using one-step solution process and antisolvent bath (ASB) method. These methods are described in chapter 3 and 4.

2.2.5 Deposition of hole transport layer

In this thesis, Spiro-OMeTAD (Fig. 2.4a) was used as the hole transport material (HTM). The hole transport layer (HTL) was fabricated by spin coating a Spiro-OMeTAD solution on top of the perovskite film at 2000 rpm for 60 s to form an approximately 250-nm-thick layer (Fig. 2.4b). The Spiro-OMeTAD solution was prepared by mixing 17.5 μl of lithium bis(trifluoromethanesulfonyl) imide (Li-TFSI) solution (520 mg of Li-TSFI in 1 ml of acetonitrile) and 28.8 μl of 4-tert-butylpyridine (TBP) with 72.3 mg of Spiro-OMeTAD in 1 ml of chlorobenzene (CBZ) solution.

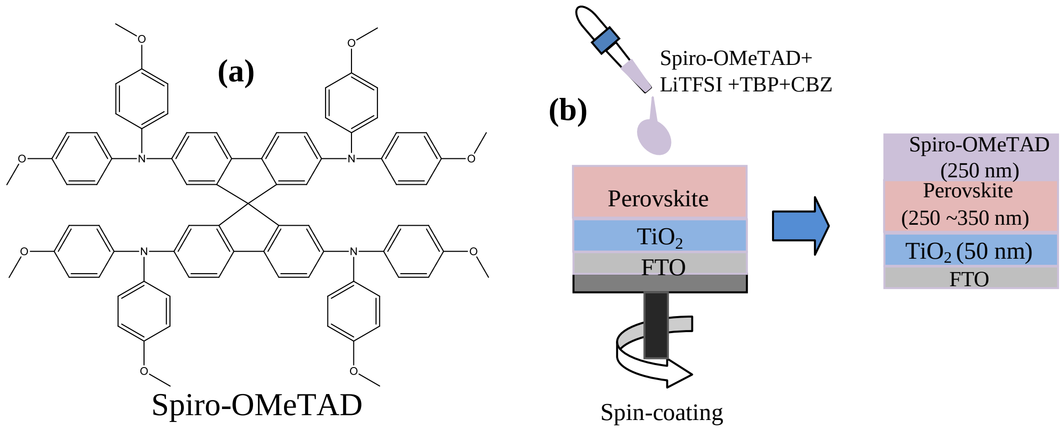

Fig. 2.4 (a) Chemical structure of Spiro-OMeTAD. (b) Schematic illustration of the fabrication of HTL on perovskite layer.

2.2.6 Deposition of back contact electrode

The metal back contact electrode was deposited using vacuum evaporation machine (VTR-350M/ERH, ULVAC KIKO, Inc.) to deposit Au metal on top of the HTL at 3.4 x 10^{-4} Pa. The Au thickness is about 80 nm. A metal mask was used to define the active area (0.06 cm^2) of the PSCs

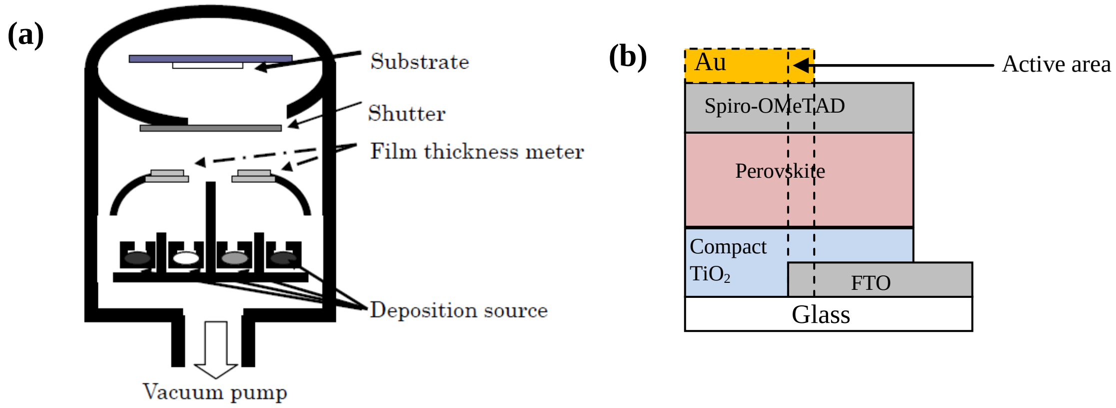

Fig. 2.5 Schematic diagram of vacuum deposition system for the evaporation of Au [2], (b) Structure of PSCs showing the evaporated Au metal electrode and the active area.

2.3 Characterization techniques

The performance of organic-inorganic hybrid solar cells strongly depends on the device structure, morphology of the light-absorbing layer, and evaluation methods. It is crucial to gain a better understanding of how to accurately: (i) characterize the film quality, (ii) measure the electrical properties of the solar cells. This can be achieved by using various electrical, optical and morphological characterization techniques which can provide detailed information about the physical and electronic properties of the material and solar cell. In this section, I will briefly discuss the most commonly used techniques with high relevance for the characterization of solar cell materials and device.

2.3.1 Current-voltage measurements

The current-voltage (*J–V)* measurements were recorded by applying external potential biases to the cells and recording the output photocurrent with a digital source meter (Agilent B2901A). A 150 W xenon lamp (Bunkoukeiki Otento-SUN3 Xe-S150) was applied as the light source, and the output irradiation intensity was adjusted to the AM 1.5G condition (100 mW/cm^2). Before each measurement, the light intensity was calibrated using a silicon reference cell (Bunkoukeiki). The step voltage and delay time were 10 mV and 10 ms, respectively. The characteristics of a typical PSCs' *J–V* curves have been described in the section 1.2.5 of chapter 1.

2.3.2 Incident photon-to-electron conversion efficiency

Incident photon conversion efficiency (IPCE) measurement was conducted in the wavelength range of 350-850 nm with a 300 W xenon light source and a monochromatic (Asahi Spectra PVL 3300) (see section 1.2.10 of chapter 1)

2.3.3 Ultraviolet-Visible Absorption Spectroscopy

Ultraviolet-visible (UV-vis) absorption spectroscopy is a technique for determining the electronic structure and composition of semiconductor materials based on absorption [4]. When UV-vis light passes through atoms or molecules of semiconductor materials, electrons in the atoms or molecules of the material become excited from a lower energy level to a higher energy level [4,5]. It is worth mentioning that the probability of absorption strongly depends on the material, wavelength, and the distance which the light travels through the material. The absorbance of a material can be expressed using Beer's Lambert law in the equation below.

$$\boldsymbol{A' = \varepsilon l c} \qquad \textbf{2.1}$$

where A′ is the absorbance, ε is the molar extinction coefficient in L mol^{-1} cm^{-1}, *l* is the path length in cm, and c is the concentration of the absorbing species in mol/L. The samples in this thesis were measured using a UV-vis spectrophotometer (Shimadzu UV 2450).

2.3.4 Photoluminescence (PL) spectroscopy

Photoluminescence (PL) spectroscopy is a powerful technique for the study and characterization of the electronic structure of materials, and the dynamical processes occurring in materials [6]. It involves measuring the energy distribution of emitted photons after optical excitation. The analyzed energy distribution is used to determine the properties of the material such as defect species, defect concentration, possible stimulated emission, band gap, recombination mechanisms and so on [6]. Steady-state PL measurement has been widely employed to investigate the origin of traps in perovskites, passivation effect and charge-hole recombination on the perovskite/ETL or HTL interfaces [7]. The samples in this thesis were measured using a Jasco NRS-

5100PL laser Raman spectrophotometer. The excitation wavelength was 325.29 nm, and the detection range was 600-900 nm.

2.3.5 X-ray diffraction

X-ray diffraction (XRD) is a nanocrystallite size measurement technique used to monitor the structure of molecular orientation of materials [4,8]. This technique is highly relevant to the investigation and optimization of charge transport properties of solar cells materials [8]. The technique can measure nanocrystallite size down to as small as 10 Å [4]. In X-ray diffraction, a diffraction pattern of the sample is obtained by illuminating the sample with x-rays. The pattern is recorded by detectors [8]. Diffraction only occurs when the distance between the adjacent lattices planes follows Bragg's law for the X-ray to be diffracted from the atomic plane [4]. In the simplest approach, as illustrated in Fig. 2.6, the relationship between the wavelength of the incident X-rays, the angle of incidence and spacing between the crystal lattice planes of atoms can be expressed using Bragg's law.

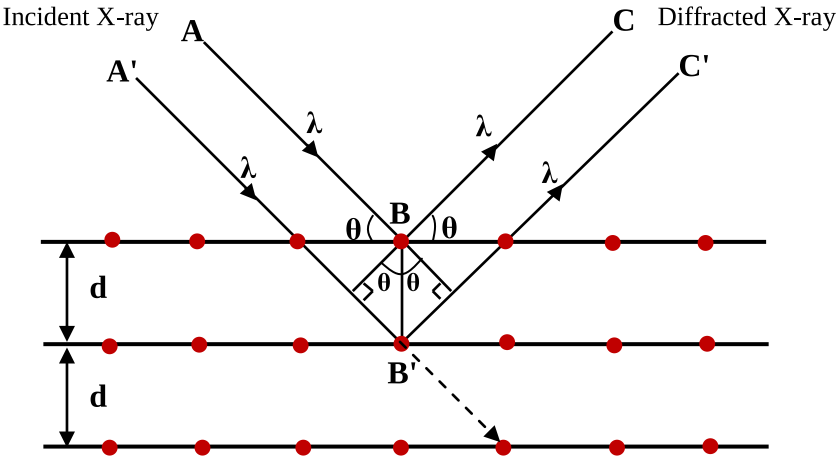

Fig. 2.6 Schematic illustration of diffraction processes in XRD measurement.

$$n\lambda = 2d\,sin\,(\theta) \qquad 2.2$$

where n (integer) is the order of interference, λ is the wavelength of the incident X-rays (usually Cu Kα: λ = 1.540562 Å), d is the lattice spacing in nm, and θ is the angle of incidence in degrees. Note that the diffraction X-rays exhibit constructive interference when the distance between paths ABC and A'B'C' differ by an integer number of wavelength [9]. It is worth mentioning that from the line broadening of the diffraction peaks, the crystallite size D (nm) can be estimated using Scherrer's equation shown below [4].

$$D = \frac{K\lambda}{\beta cos\theta} \qquad 2.3$$

where β is the full width at half maximum intensity (FWHM), in radian. θ is the diffraction angle in degrees of the considered diffraction peak, and K is a shape factor (dimensionless) The value of K is around 0.94 but varies with the actual shape of the crystalline. In this thesis, the XRD patterns were recorded in the 2θ range of 5-60° using an X-ray diffractometer (Rigaku RINT2500V/PC) with Cu Kα radiation (40 kV, 100 mA).

2.3.6 Atomic Force Microscopy

Atomic force microscopy (AFM) was invented in 1986 [11]. It is a powerful technique for nanoparticle size, shape, roughness, and morphology measurement. AFM can be employed for either single composition nanoparticles or mixed nanoparticle composites. Also, it can be conducted in air and liquid environments. AFM can exhibit a spatial resolution of about 4 nm and has the merit of easy sample preparation. It can give more detailed information regarding particle morphology in the z-direction than the scanning electron microscopy and transmission electron microscopy. However, AFM has the disadvantages of only analyzing small portions of the sample and long data acquisition time. In AFM, the three most important classes of interaction between the probe and the substrate are (i) contact mode, (ii) non-contact mode, and (iii) tapping mode [4].

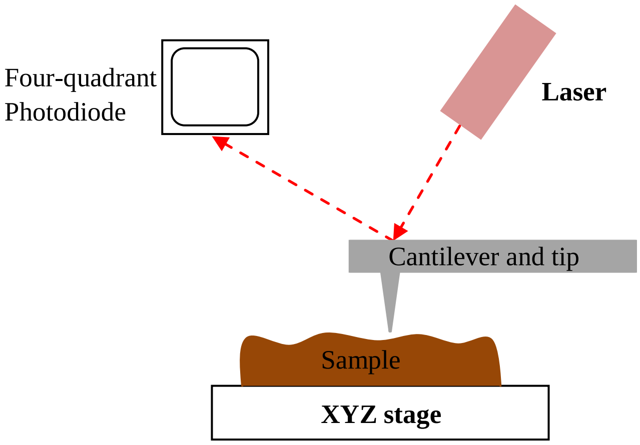

Fig. 2.7 Schematic illustration of the working principle of AFM

AFM is made up of a probe in the shape of a cantilever with a small tip at its free end, a laser, a four-quadrant photodiode, and a scanner unit (Fig. 2.7). The cantilever bends in response to the force between the tip and the sample [11]. The laser beam is focused onto the back of the free end of the cantilever and reflected to the four-quadrant photodiode. This allows detecting the bending of the cantilever with high precision. When the tip of the cantilever is scanned across the sample surface, the force of interaction between the tip and the sample modifies the static bending of the cantilever (i.e., when the tip is in contact) or the resonance frequency of the cantilever oscillation (i.e., when it is vibrated, and the tip is at a small distance from the surface) [8]. In this thesis, contact mode AFM (Keyence VN-8000 viewer and an analyzer) has been used to study the surface roughness and morphology of our samples.

2.3.7 Scanning Electron Microscopy

Scanning electron microscopy is an advanced imaging technique and widely used for the characterization of nanoparticle size, shape, arrangement and degree of agglomeration [4].

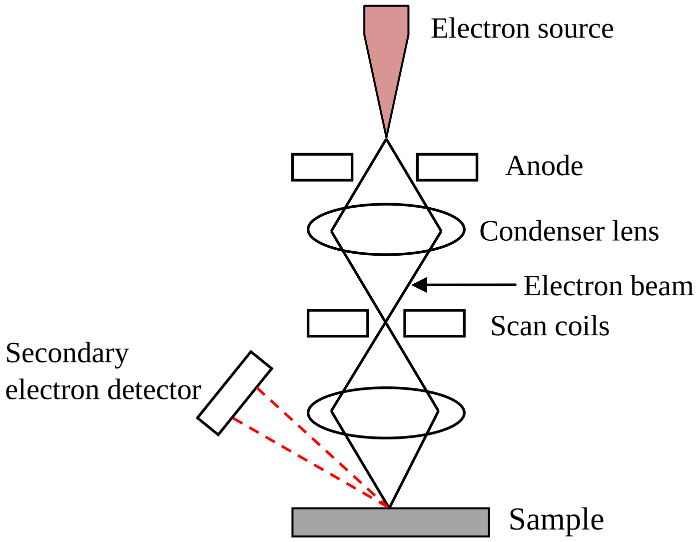

Fig. 2.8 Schematic illustration of SEM set-up

In a typical SEM, an electron gun and multiple condenser lenses produce an electron beam. (Fig. 2.8) The rays of the beam are deflected at a various angle of the optic axis by the sets of electromagnetic scan coils [12]. The objective lens focuses the electron beam to very fine spot (1-5 nm) and scans the sample surface in a raster pattern. When scanning the primary electron beam over the surface of the sample, secondary electrons are emitted from the sample surface and detected, thereby producing SEM image [12]. Also, the backscattered electrons of the electron beam might be detected. The backscattered electron image can be used for contrasting the sample regions. SEM has the advantages of superior lateral resolution and the capability of analyzing a broad range of scales from nanometer range to millimeter range. However, SEM lacks z direction morphology information, and it is also a vacuum technique [8]. In this thesis, the morphology of our samples was observed by field emission SEM (FE-SEM; JEOL JSM6335FM, the acceleration voltage of 10 kV). For SEM analysis, the samples were mounted on the sample holder and taped with a conductive tape.

2.3.8 Fourier Transform Infrared spectroscopy

The compositional purity of the perovskite film was characterized by Fourier transform infrared spectroscopy (FT-IR) Shimadzu IR-Prestige-21, FT-IR-8400S. The measurements were carried out using samples prepared by the KBr pellet method.

2.3.9 Kelvin Probe Measurement

The work function of WO_x and WO_x/C_{60} films deposited on FTO substrates were characterized by Kelvin probe (RIKEN KEIKI FAC-1, A16621-4) vibrating capacitor method. The C_{60} films were deposited on the FTO/WO_x layer by vacuum evaporation in a glove box [13]. The surface potential difference between Au plate and the samples and the work function is evaluated by using Equation 2.4.

$$WF_s = WF_{Au} - V_E \qquad 2.4$$

where WF_s is the work function of the sample surface, WF_{Au} is the work function of the Au (4.9 eV) and V_E is the external voltage.

2.4 Reference

[1] J. Burschka, N. Pellet, S.-J. Moon, R. Humphry-Baker, P. Gao, M. K. Nazeeruddin, and M. Gratzel, Nature 499, 316 (2013).

[2]S.-G. Park, Study of charge carrier injection and transport in organic light-emitting diodes, http://ir.nul.nagoya-u.ac.jp/jspui/handle/2237/19718

[3] K. Wang, Y.Shi, Q. Dong, Y. Li, S. Wang, X. Yu, M. Wu, T. Ma, Low-temperature and solution-processed amorphous WOx as an electron-selective layer for perovskite solar cells, J. Phys. Chem. Lett. 6 (2015) 755-759.

[4] K. Lu, Nanoparticulate Materials: Synthesis, Characterization, and Processing, John Wiley & Sons, Inc. New Jersey, (2013).

[5] H. Borchert, Solar Cells Based on Colloidal Nanocrystals, Springer Cham Heidelberg New York Dordrecht London, (2014).

[6] G. D. Gilliand, photoluminescence spectroscopy of crystalline semiconductors, Materials Science and Engineering, R18 (1997) 99-400.

[7]Y. Shao, Z. Xiao, C. Bi, Y. Yuan, J. Huang, Origin, and elimination of photocurrent hysteresis by fullerene passivation in CH3NH3PbI3 planar heterojunction solar cells, Nat. Commun., 5 (2014) 5784.

[8] F. C. Krebs, Polymer Photovoltaics: a practical approach, SPIE press, USA, (2008).

[9]https://serc.carleton.edu/research_education/geochemsheets/BraggsLaw.html

[10] D. Abou-Ras, T. Kirchartz, U. Rau, Advanced Characterization Techniques for Thin Film Solar Cells, Wiley-VCH Verlag GmbH & Co. KGaA, (2011).

[11] G. Binnig, C. F. Quate, C. Gerber, Atomic force microscope. Phys. Rev Lett. 56 (1986), 930-933.

[12] T. G. Rochow, E. G. Rochow, An Introduction to Microscopy by Means of Light, Electron, X-Rays, or Ultrasound, Plenum Press New York and London, 1978 &1979.

[13] N. Ishiyama, M. Kubo, T. Kaji, M. Hiramoto, Doping-based control of the energetic structure of photovoltaic co-deposited films, Appl. Phys. Lett., 99 (2011), 133301

Chapter 3

Influence of air-assisted flow on the performance of planar perovskite solar cells fabricated by two-step spin-coating method [22, 23]

3.1 Introduction

Perovskite solar cells (PSCs) can be fabricated using various architectures and methods. Era *et al.*,[1] Lui *et al.*,[2] Mitzi *et al.*,[3] and Salau [4] adopted vapor deposition in vacuum via a dual or single source to deposit the thin layer of mixed halide perovskite employed in planar-structured solar cells and achieved a PCE of over 15%. However, vapor deposition significantly raises the cost of fabrication and consequently poses a potential hurdle to large-scale production. The perovskite layer can be easily prepared by a solution-processed method. Dualeh et al., and Eperon et al., fabricated perovskite films using the one-step spin-coating method. However, it was found that the one-step spin-coating method resulted in nonuniform films that permitted direct contact between the electron-transporting layer (ETL) and the hole-transporting layer (HTL).[5,6] In contrast, a two-step sequential deposition method that involves the spin-coating of the hot lead(II) iodide (PbI_2) in *N,N*-dimethylformamide (DMF) onto mesoscopic or planar-structured substrates, followed by dipping into methylammonium iodide–isopropanol (CH_3NH_3I–IPA) solution, has enabled the successful construction of uniform and fully covered $CH_3NH_3PbI_3$ films.[7-10] However, depositing perovskite films prepared by two-step dipping on a planar substrate has been reported to be associated with problems such as the incomplete reaction of PbI_2 crystals with organic ammonium and uncontrolled perovskite crystal size as well as rough surface morphology.[10-12] These reports demonstrated that the resultant perovskite films are more suitable for use in mesoporous-structured PSCs.[8] Therefore, a faster and easier method in which perovskite formation and crystal growth can be controlled, resulting in high-quality films with homogeneous morphology, is exceedingly desirable for the preparation of planar PSCs with superior performance.

We investigated the effect of air-assisted flow (AAF) on the performance of perovskite solar cell fabricated by two-step spin-coating method.[13,14,19] The airflow is incorporated to assists in the deposition of the PbI_2 and perovskite layer during the spin-coating process. It was found that the uniformity and coverage of the perovskite light-absorbing layer over the underlying compact-TiO_2 ETL were improved by incorporating airflow. In addition, we meticulously investigated the effect of AAF on (i) PbI_2 crystallization, (ii) perovskite morphology, and (iii) device performance. The results of the device constructed with AAF (w/ AAF) and a control device without AAF (w/o AAF) were compared.

3.2 Preparation of perovskite film

Fig. 3.1(a) shows the device structure and Fig. 3.1(b) is the schematic diagram of the airflow condition. Fig. 3.2 (a) and (b) describe the fabrication procedures for with and without AAF in the two-step spin-coating method. For the perovskite layer, a 1.1 M PbI_2/DMF solution was consecutively spin-coated onto the TiO_2 layer at 2000 rpm for 5 s and 6000 rpm for 10 s. After a delay time of 2 s, dry air with a pressure of 0.2 MPa was blown over the surface of the PbI_2 during the spin coating process. The height from the substrate to the outlet is controlled to be around 10 cm. Next, the PbI_2 film was dried at 100 °C for 10 min, then 10 mg/ml CH_3NH_3I/IPA solution was loaded onto the PbI_2 layer with a waiting time of 30 s before spin coating at 4000 rpm for 30 s to form about 350-nm-thick layer. Dry air was blown over the surface of the perovskite solution for the duration of spin coating. After spin coating, the samples were set on the hotplate for crystallization at 100 °C for 10 min. For w/o AAF cells used as a control group, other than omitting the airflow, every other condition was kept identical (Fig. 3.2 (b)).

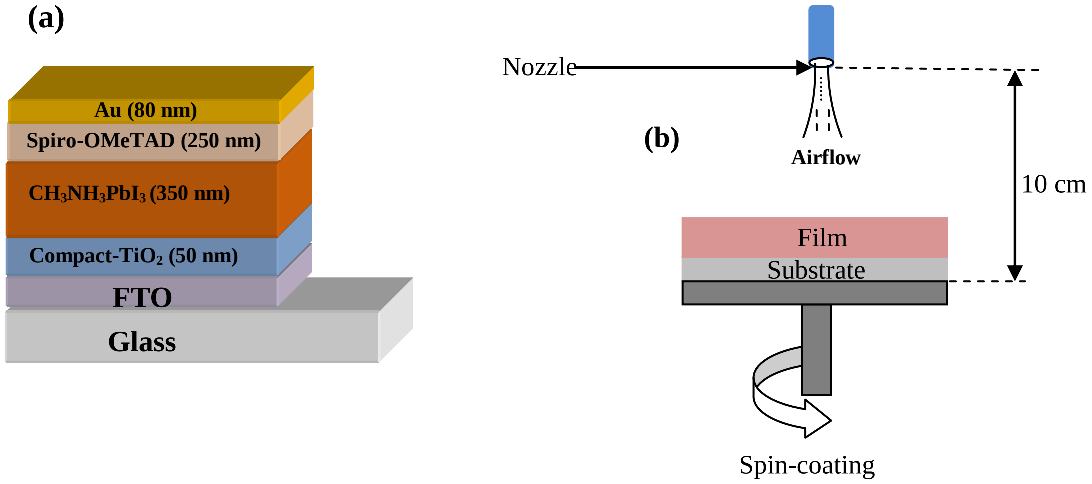

Fig 3.1 (a) Device structure (b) Schematic diagram of the air flow condition. The diameter of the air flow outlet is about 0.5 cm, and a pressure of 0.2MPa.

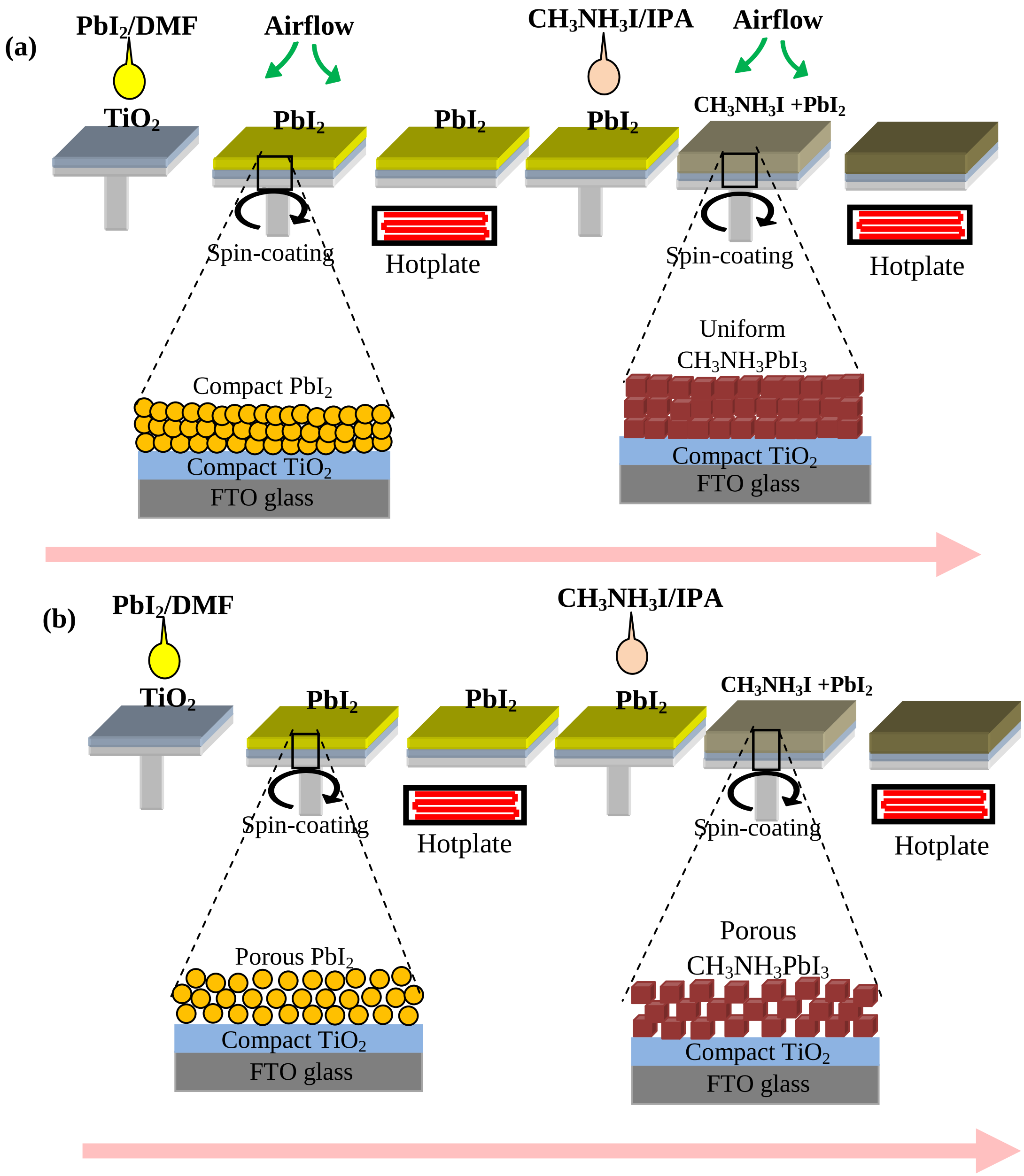

Fig. 3.2 (a) Schematic of procedure of perovskite film fabricated w/ AAF in the two-step spin-coating method progressing from left to right. (b) Schematic of procedure of perovskite film fabricated w/o AAF in the two-step spin-coating method progressing from left to right.

3. 3 Results and discussion

3.3.1 Morphological characterization

The top-view and cross-sectional SEM images of PbI_2 and $CH_3NH_3PbI_3$ films prepared by w/ AAF and w/o AAF methods are shown in Figs. 3.3 and 3.4. For the w/o AAF condition, PbI_2 and $CH_3NH_3PbI_3$ films did not sufficiently cover the underlying compact-TiO_2 layer, as shown in Figs. 3.3(a) and 3.3(b). Rough PbI_2 and $CH_3NH_3PbI_3$ layers with several grooves that could cause a direct contact between the compact TiO_2 layer and HTL [Figs. 3.4(a) and 3.4(b), red arrows] were also confirmed. However, there were significant improvements when the w/ AAF method was incorporated [Figs. 3.3(c) and 3.3(d)].The compact TiO_2 underlying layer was completely covered by PbI_2 and $CH_3NH_3PbI_3$ crystal particles, as shown in Figs.3. 4(c) and 3.4(d).

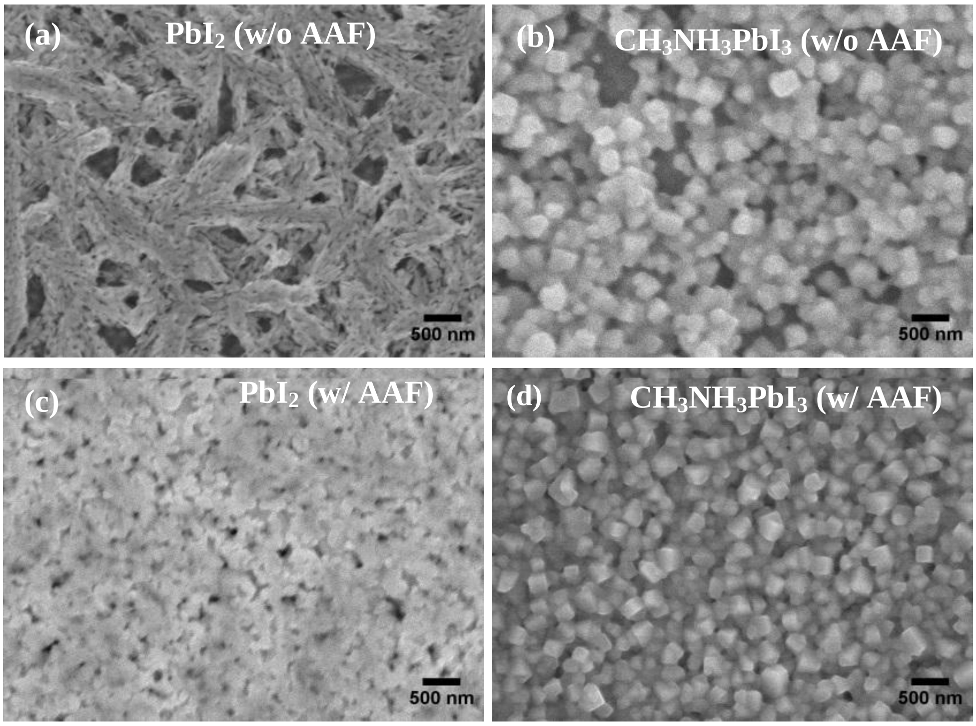

Fig. 3.3 SEM images of the PbI_2 and $CH_3NH_3PbI_3$ films prepared by (a, b) w/o AAF method and (c, d) w/ AAF method.

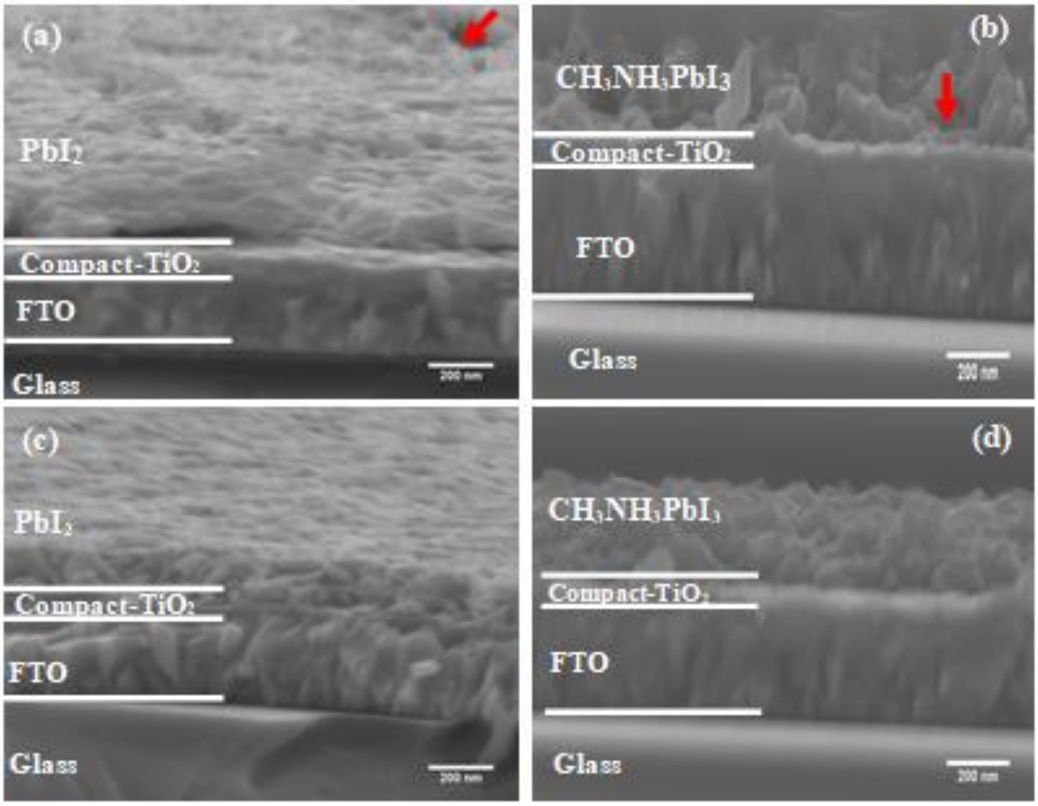

Fig. 3.4 Cross-sectional SEM images of PbI_2 and $CH_3NH_3PbI_3$ films prepared by (a, b) w/o AAF method and (c, d) w/ AAF method.

We analyzed the particle size distribution of the perovskite films fabricated w/ AAF, and w/o AAF by image analysis software (Nano Measure), (see Figs. 3.5(a) and 3.5(b)). The perovskite film prepared by the w/ AAF method had particle sizes ranging from 100 to 320 nm with a mean particle size of 196.4 ± 21 nm. In contrast, the w/o AAF-based perovskite film had particle sizes ranging from 130 to 400 nm, with a mean particle size of 262.5 ± 51 nm. The smaller variation in particle size distribution exhibited by the w/ AAF perovskite film could be attributed to both the fast evaporation of DMF solvent in PbI_2 and the IPA solvent during spin-coating. The airflow can promote the uniform crystallization process of the PbI_2 film and control the reaction kinetics between PbI_2 and CH_3NH_3I through evaporating solvents during the spin coating process.

The morphology of perovskite films with relatively uniform distributions of crystal sizes is expected to be beneficial in enhancing the device PCE.

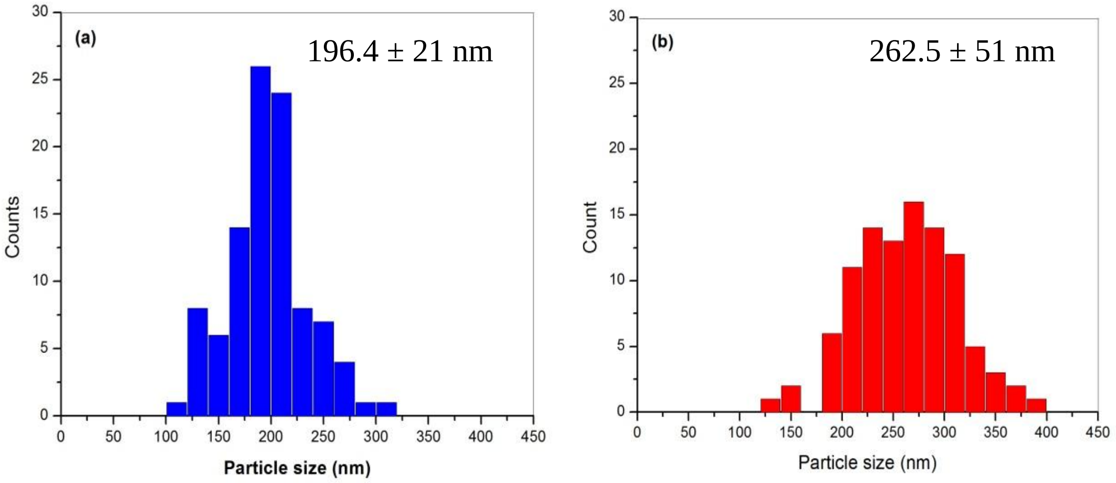

Fig. 3.5 Analysis of the particle size distribution for perovskite films (a) w/ AAF and (b) w/o AAF.

Notably, we have also employed the AAF route to prepare PbI_2 films, contrary to what had been previously reported.15,18) It was found that the surface coverage and uniformity of $CH_3NH_3PbI_3$ perovskite are strongly influenced by the morphology of PbI_2 in two-step spin coating or sequential deposition, and by controlling the crystallization of PbI_2 with AAF, a highly compact layer could be readily obtained.13) In our case, the PbI_2 films prepared by the w/o AAF method usually consist of larger crystals with rough surface, whereas the w/ AAF method yielded a much smoother surface [Figs. 3.6(a) and 3.6(b)]. The rough surface of the w/o AAF films could be attributed to the ultralow evaporation rate of DMF in ambient air, which results in low degrees of supersaturation and precipitation,18) and thereby promote the formation of nonconstant perovskite morphology in the underlying compact TiO_2 layer.

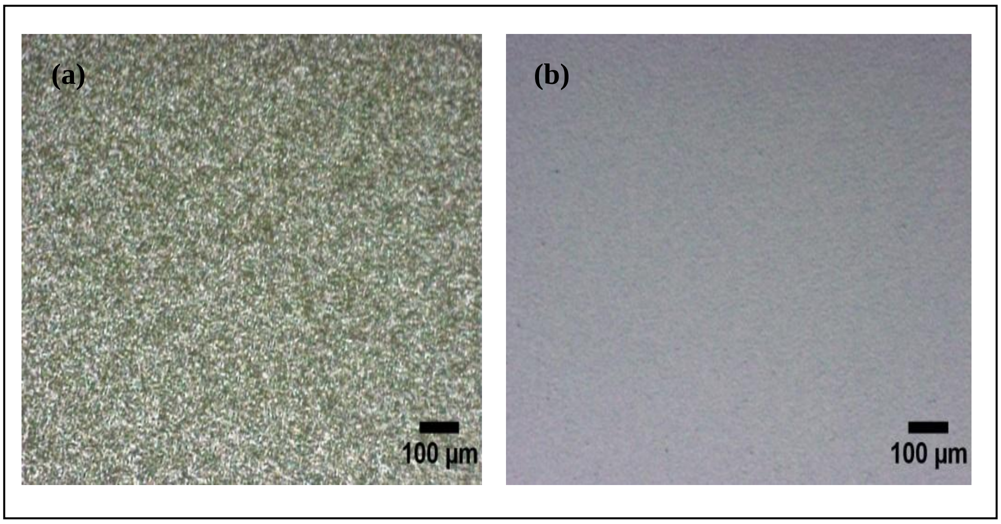

Fig. 3.6 Optical microscopy images (200 x 200 μm^2) of PbI_2 prepared by (a) w/ o AAF method and (b) w/ AAF method.

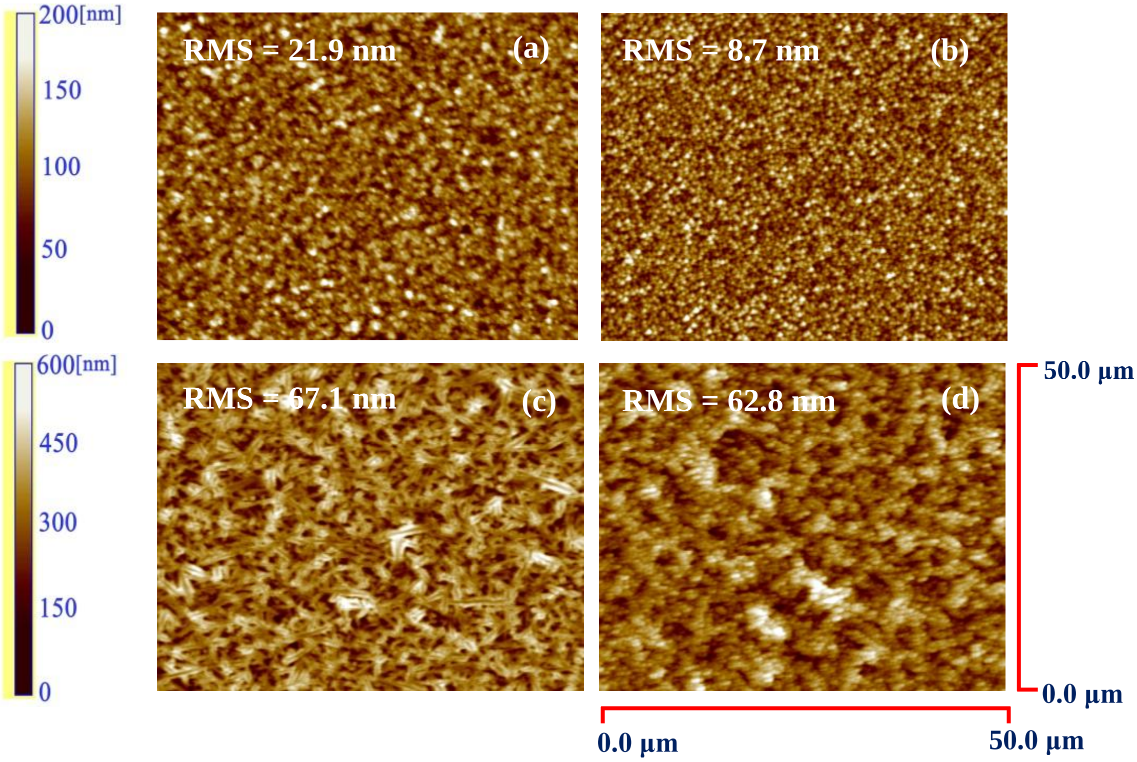

Fig. 3.7 AFM images of PbI_2 and $CH_3NH_3PbI_3$ films prepared by (a), (b) w/ AAF method and (c), (d) w/o AAF method, respectively.

We further characterized the PbI_2 and $CH_3NH_3PbI_3$ films derived by the two methods by AFM, as shown in Fig. 3.7. The calculated root-mean-squared roughnesses of PbI_2 and perovskite films made by the w/ AAF method [Figs. 3.7(a) and 3.7(b)] are 21.9 and 8.7 nm, respectively. For the films made by the w/o AAF method [Figs. 3.7(c) and 3.7(d)], they are 67.1 and 62.8 nm, respectively. The roughness of films fabricated by the w/ AAF route is significantly reduced compared with that of w/o AAF films, as is evident in the AFM images. The significant disparities in the calculated RMS values between the w/o AAF and w/ AAF films show that the AAF route is more effective for fabricating smooth and homogeneous perovskite films for reproducible and high-efficiency solar cells.

3.3.2 Photovoltaic performance characterization

The *J–V* curves of forward and reverse scans of our best-performance solar cells are shown in Fig. 3.8. The photovoltaic parameters of the best performance, average values, and corresponding standard deviation of w/ AAF and w/o AAF planar PSCs are summarized in Table 1. All the parameters of the best-performance w/ AAF solar cell are superior to those of the w/o AAF solar cell. For the w/o AAF solar cell, the forward potential scan (from short circuit to open circuit) revealed values of 17.91 mA/cm^2, 0.864 V, 0.560, and 8.67% for the short-circuit density (J_{sc}), open-circuit voltage (V_{oc}), fill factor (FF), and PCE, respectively. Similarly, the reverse potential scan (from open circuit to short circuit) resulted in J_{sc} of 17.91 mA/cm^2, V_{oc} of 0.881 V, FF of 0.620, and PCE of 9.78%. Conversely, for the w/ AAF device, higher values of J_{sc} of 21.52 mA/cm^2, V_{oc} of 0.980 V, FF of 0.630, and PCE of 13.28% were obtained from the forward potential scan, and 21.63 mA/cm^2, 1.02 V, 0.714, and 15.75% respectively, from the reverse potential scan. The calculated, i.e., average PCE values were 14.52 and 9.22% for the best-performance w/ AAF and w/o AAF devices, respectively.

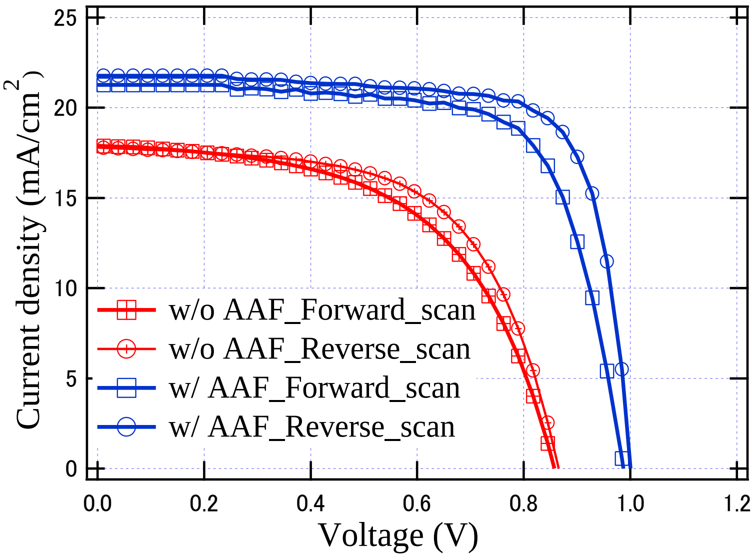

Fig. 3.8 *J-V* curves of the best-performance w/AAF and w/o AAF solar cells under AM 1.5G 1 sun illumination conditions (100 mW/cm^2) recorded at forward and reverse scans.

Table 1. Photovoltaic parameters of PSCs prepared by w/ AAF and w/o AAF methods, measured. The values in brackets correspond to the average values from 10 planar cells and the corresponding standard deviation.

Solar cells	Scan direction	*J*sc (mA/cm^2)	*V*oc (V)	FF	PCE (%)	Average PCE (%)
(Bestcells)	Forward	21.52	0.980	0.630	13.28	
w/ AAF	Reverse	21.63	1.020	0.714	15.75	14.52
w/ AAF	Forward	(21.46±0.20)	(0.980±0.003)	(0.620±0.01)	(13.00±0.15)	
(10 Cells)	Reverse	(21.61±0.56)	(1.000±0.006)	(0.710±0.01)	(15.34±0.20)	
(Bestcells)	Forward	17.91	0.864	0.560	8.67	
w/o AAF	Reverse	17.91	0.881	0.620	9.78	9.22
w/o AAF	Forward	(17.45±0.21)	(0.894±0.031)	(0.529±0.02)	(8.25±0.30)	
(10 Cells)	Reverse	(17.43±0.21)	(0.900±0.030)	(0.560±0.05)	(8.77±0.70)	

Hysteresis was observed in the *J–V* characterization of both cells but was not pronounced. The results of the statistical analysis of photovoltaic parameters obtained from 10 planar PSCs are shown in Fig. 3.9. Th planar PSCs showed average efficiencies with the small standard deviation (Table I).

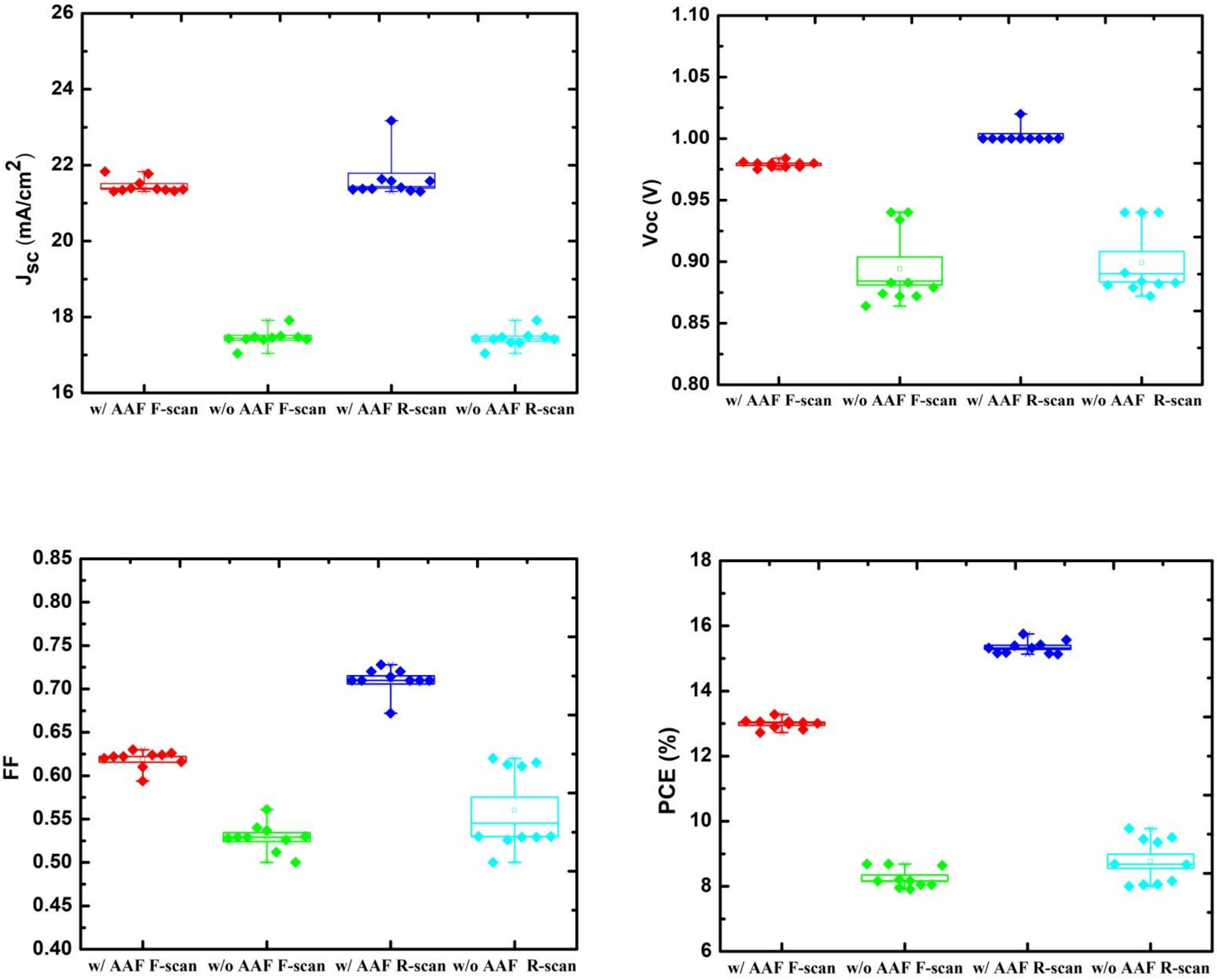

Fig. 3.9 Statistical analysis of forward potential scan (F-scan) and reverse potential scan (R-scan) results of J_{sc}, V_{oc}, FF, and PCE of the PSCs fabricated by w/AAF and w/o AAF methods. The data from 10 cells were statistically analyzed.

The w/o AAF and w/ AAF devices have average efficiencies and standard deviations of 8.25 ± 0.30% and 13.00 ± 0.15% for the forward potential scan and 8.77 ± 0.70% and 15.34 ± 0.20% for the reverse potential scan, respectively. The small standard deviations obtained from the devices indicate that both w/ and w/o AAF devices have good reproducibility. The apparent disparities between the photovoltaic parameters of both solar cells can be attributed to their $CH_3NH_3PbI_3$ layer morphological differences. Note that a nonuniform perovskite morphology will cause (1) light to pass straight through the perovskite film without absorption, thereby decreasing the available photocurrent, and (2) a high frequency of shunt paths, which will enable contact between the HTM layer and the compact-TiO_2 layer.[20, 21)] Both of these effects can unavoidably cause a decrease in PV parameters

To gain insight into the influence of perovskite morphology on *Jsc*, the IPCE spectra, which specify the ratio of extracted electrons to incident photons at a given wavelength, were measured for the best-performance w/o AAF and w/ AAF solar cells (Fig. 3.10). The IPCE spectra of both devices show photoresponse in a wide range from 350 to 800 nm, with a maximum value close to ~80% for the w/ AAF solar cell. The relatively high maximum efficiency (~80%) obtained by the w/ AAF solar cell is indicative of excellent light harvesting efficiency due to the homogeneous and well-controlled perovskite film. The integrated J_{sc}values from IPCE curves for w/o AAF (17.07 mA/cm^2) and w/ AAF (21.32 mA/cm^2) solar cells were found to be consistent with the experimentally measured *Jsc* value under simulated AM 1.5 illumination of 100 mW/cm^2. The mismatch between the simulated sunlight and the AM 1.5G standard is assumed to be negligible.

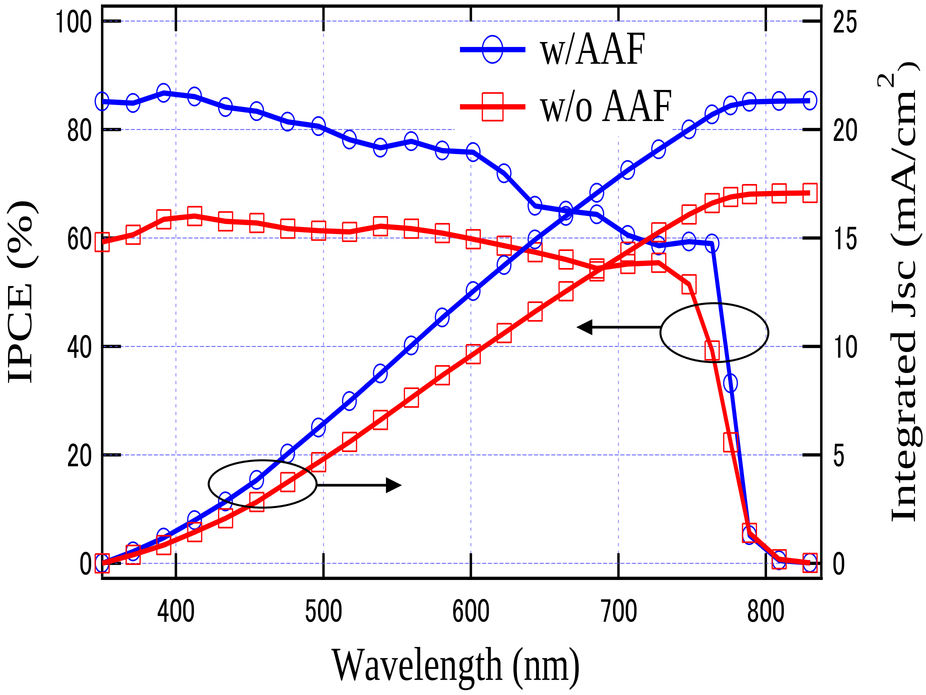

Fig. 3.10 IPCE spectra and integrated photocurrent curves for the best w/ AAF (blue circles) and w/o AAF (red squares) solar cells.

3.3.3 Structural and optical characterization

Typical XRD patterns for w/ AAF and w/o AAF $CH_3NH_3PbI_3$ crystals coated on FTO glass/compact-TiO_2 substrates are presented in Fig. 3.11. Strong diffraction peaks located at 2θ of 14.08°, 23.48°, 28.40°, and 31.86° can be assigned to (110), (211), (220), and (310) planes of the tetragonal $CH_3NH_3PbI_3$ phase, respectively. Notably, the XRD patterns of the two films are the same, and they reveal traces of remnant PbI_2 in both w/ AAF and w/o AAF $CH_3NH_3PbI_3$ films. We inferred that this might be the result of an incomplete reaction of PbI_2 and CH_3NH_3I owing to the absence of a mesoporous scaffold.16) We made an effort to extend the loading time to 180 s, but the PbI_2 phase could not be entirely removed from the perovskite film. Previous reports have suggested that residual unreacted PbI_2 may act as a built-in hole-blocking layer, and may be advantageous for the solar cell light conversion.9, 17)

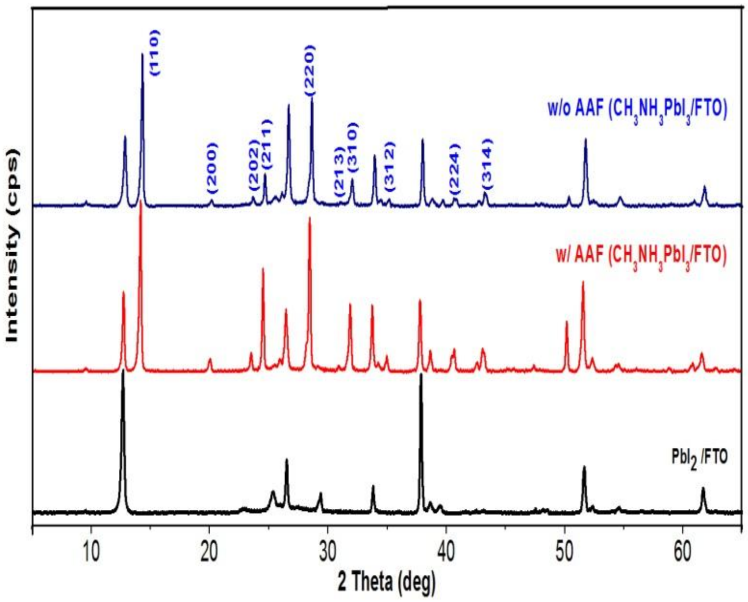

Fig. 3.11 XRD patterns for PbI_2 (PDF #73-1754) on FTO glass/compact-TiO_2, $CH_3NH_3PbI_3$ perovskite for both w/ AAF (red line) and w/o AAF (blue line) solar cells (FTO glass/compact-TiO_2/perovskite)

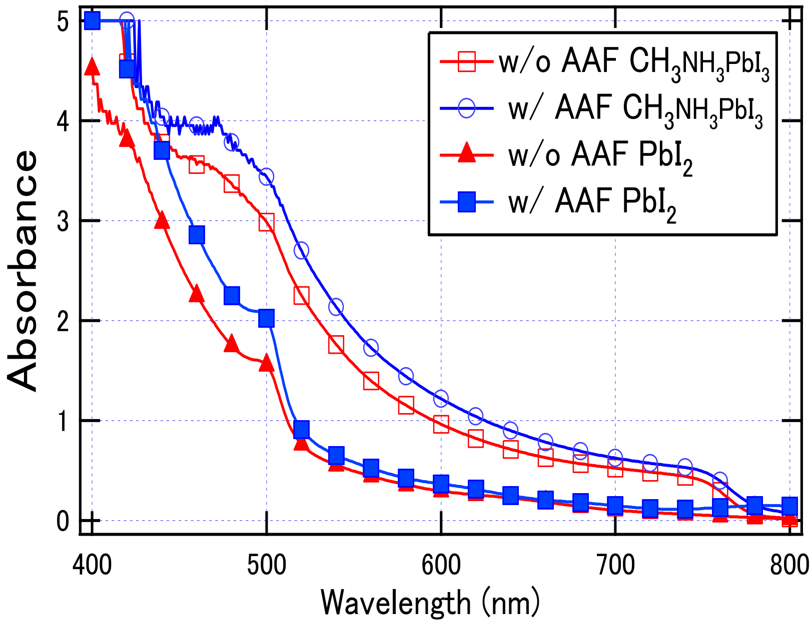

Fig. 3.12 Absorption spectra of PbI_2 and perovskite films prepared by w/ AAF and w/o AAF methods.

Absorption spectroscopy was carried out to study the optical properties of $CH_3NH_3PbI_3$ prepared by w/ AAF and w/o AAF methods. As shown in Fig. 3.12, the UV-vis spectra of PbI_2 and $CH_3NH_3PbI_3$ films prepared by the two methods span from 400–800 nm. The w/ AAF PbI_2 and $CH_3NH_3PbI_3$ films comparatively show an increased absorption intensity from the UV-to-near-infrared region. This is consistent with the increased performance of IPCE, as shown in Fig. 3.10. The increased absorbance exhibited by the w/ AAF-based films should be attributed to the improved surface coverage of the underlying compact-TiO_2 layer.

The PL measurements were performed to gain further insight into the relevance of the compact-TiO_2/perovskite and perovskite/HTM interface for the two types of preparation methods. Figure 3.13 shows the PL spectra for compact-TiO_2/$CH_3NH_3PbI_3$ and $CH_3NH_3PbI_3$/spiro-OMeTAD samples prepared by the w/ AAF and w/o AAF methods. The emission peaks observed at around 760 nm resulted from the PL of $CH_3NH_3PbI_3$ which is similar to results indicated in other reports.10)

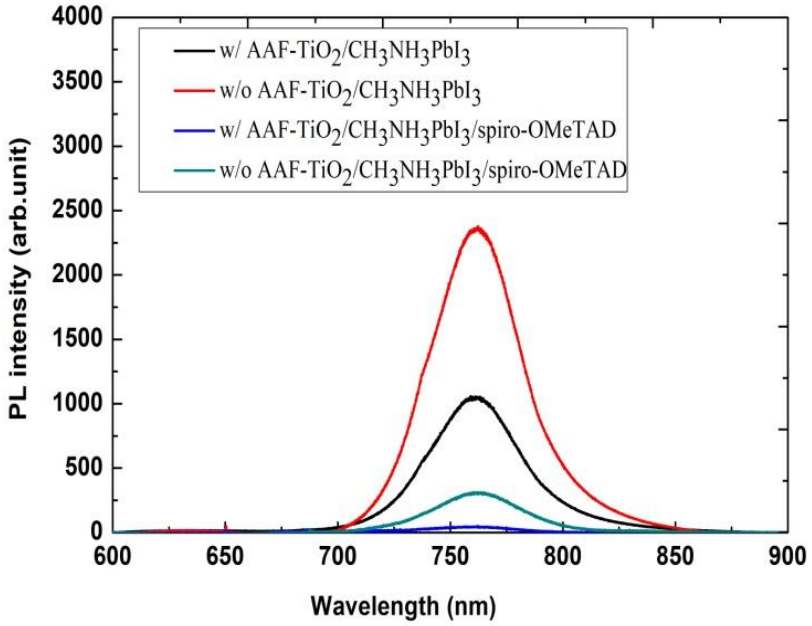

Fig. 3.13 Photoluminescence (PL) spectra of compact-TiO_2/$CH_3NH_3PbI_3$ and compact-TiO_2/ $CH_3NH_3PbI_3$ /spiro-OMeTAD on FTO glass substrate prepared by w/ AAF and w/o AAF methods.

In general, samples prepared with AAF exhibit lower PL emission. However, the PL quenching is stronger when the samples are excited through the Spiro-OMeTAD film. When considering the sufficient coverage of $CH_3NH_3PbI_3$ for the w/ AAF samples compared with the w/o AAF samples, the lower PL emission, and significant quenching indicate that better electron and hole collections are achieved when the electron-hole pair is generated close to the compact-TiO_2/perovskite and perovskite/spiro-OMeTAD interfaces, respectively. We then inferred that the improved PV performance of the w/ AAF solar cells is mainly due to the efficient charge separation at the two interfaces.

3. 4 Conclusions

We demonstrated the importance of using AAF in the two-step spin-coating method for preparing $CH_3NH_3PbI_3$ perovskite films for highly efficient solar cells. Two-step spin-coating deposition is found to be more precise than the two-step dipping method because of its quantitatively managed procedure. Improving the $CH_3NH_3PbI_3$ coverage of the underlying compact-TiO_2 layer was vital to achieving high light harvesting and efficient charge separation for the w/ AAF devices. The application of AAF in the fabrication of both PbI_2 and perovskite films for PSCs led to a PCE of 13.28% for the forward potential scan and 15.75% for the reverse potential scan. The correlations between the efficiencies and film morphologies of our solar cells were systematically studied using absorption spectra, AFM images, and SEM images. Our studies provide a promising route for fabricating low-cost, high-performance PSCs by an easy method.

3.5 References

1) M. Era, T. Hattori, T. Taira, and T. Tsutsui, Chem. Mater. **9,** 8 (1997).

2) M. Liu, M. B. Johnston, and H. J. Snaith, Nature **501,** 395 (2013).

3) D. B. Mitzi, M. Prikas, and K. Chondroudis, Chem. Mater. **11,** 542 (1999).

4) A. Salau, Sol. Energy Mater. **2,** 327 (1980).

5) A. Dualeh, N. Tétreault, T. Moehl, P. Gao, M. K. Nazeeruddin, and M. Grätzel, Adv. Funct. Mater. **24,** 3250 (2014).

6) G. E. Eperon, V. M. Burlakov, P. Docampo, A. Goriely, and H. J. Snaith, Adv. Funct. Mater. **24,** 151 (2014).

7) S. Dharani, H. K. Mulmudi, N. Yantara, P. T. T. Trang, N. G. Park, M. Graetzel, S. Mhaisalkar, N. Mathews, and P. P. Boix, Nanoscale **6,** 1675 (2014).

8) D. Liu and T. L. Kelly, Nat. Photonics **8,** 133 (2014).

9) A. Yella, L.-P. Heiniger, P. Gao, M. K. Nazeeruddin, and M. Grätzel, Nano Lett. **14,** 2591 (2014).

10) J. Burschka, N. Pellet, S.-J. Moon, R. Humphry-Baker, P. Gao, M. K. Nazeeruddin, and M. Grätzel, Nature **499,** 316 (2013).

11) Q. Chen, H. Zhou, Z. Hong, S. Luo, H.-S. Duan, H.-H. Wang, Y. Liu, G. Li, and Y. Yang, J. Am. Chem. Soc. **136,** 622 (2013).

12) K. Liang, D. B. Mitzi, and M. T. Prikas, Chem. Mater. **10,** 403 (1998).

13) S. Razza, F. Di Giacomo, F. Matteocci, L. Cinà, A. L. Palma, S. Casaluci, P. Cameron, A. D'epifanio, S. Licoccia, and A. Reale, J. Power Sources **277,** 286 (2015).

14) J.-H. Im, H.-S. Kim, and N.-G. Park, APL Mater. **2,** 081510 (2014).

15) K.-L. Wu, A. Kogo, N. Sakai, M. Ikegami, and T. Miyasaka, Chem. Lett. **44**, 321 (2015).

16) H.-S. Kim and N.-G. Park, J. Phys. Chem. Lett. **5,** 2927 (2014).

17) F. Hao, C. C. Stoumpos, Z. Liu, R. P. Chang, and M. G. Kanatzidis, J. Am. Chem. Soc. **136,** 16411 (2014).

18) F. Huang, Y. Dkhissi, W. Huang, M. Xiao, I. Benesperi, S. Rubanov, Y. Zhu, X. Lin, L. Jiang, and Y. Zhou, Nano Energy **10,** 10 (2014).

19) J.-H. Im, I.-H. Jang, N. Pellet, M. Grätzel, and N.-G. Park, Nat. Nanotechnol. **9,** 927 (2014).

20) C. Wehrenfennig, G. E. Eperon, M. B. Johnston, H. J. Snaith, and L. M. Herz, Adv. Mater. **26,** 1584 (2014).

21) B. Lei, V. O. Eze, T. Mori, J. Nanosci. Nanotechnol.16, 3176 (2016).

22) B. Lei, V. O. Eze, T. Mori, Jpn. J. Appl. Phys., 54, 100305 (2015).

23) V. O. Eze, B. Lei, T. Mori, Jpn. J. Appl. Phys., 55, 02BF08 (2016).

Chapter 4

Effect of solvent annealing on the performance of planar perovskite solar cells fabricated by one-step spin-coating method [40)]

4.1 Introduction

Several deposition methods such as vacuum evaporation,[1)] one-step spin-coating,[2,3)] two-step sequential deposition,[4)] two-step spin-coating,[5,6)] and a vapor-assisted solution process[7)] have been developed for fabricating perovskite films. Among these methods, one-step spin-coating is the simplest method of fabricating low-cost solar cell devices. However, it is challenging to form high-quality and continuous perovskite films by spin-coating a mixed solution of lead iodide (PbI_2) with methylammonium iodide (MAI) in a polar solvent such as dimethylformamide (DMF) owing to the rapid crystallization of methylammonium lead halide ($MAPbI_3$).[3,8)] In the two-step dipping or spin-coating method, the PbI_2 solution is first deposited onto the substrate, followed by dipping into or spin-coating MAI solution to produce the perovskite film. On a planar substrate, incomplete conversion of PbI_2 usually exists, which may cause problems in the device reproducibility and stability.[7)]

High-performance PSCs have been obtained with solution-processed methods, but one drawback is that the polycrystalline films have a relatively small grain size, between 100 and 300 nm, owing to the rapid reaction of PbI_2 and MAI, and the crystallization of the perovskite materials.[9)] The polycrystalline films are usually prone to bulk defects and trap states at the grain boundaries.[10,11)] To further improve the quality of perovskite films, many different approaches have been developed. These include solvent engineering,[12)] fast deposition crystallization,[13)] inclusion of various additives,[14-18)] moisture-assisted method,[19)] and air exposure.[20)] With all these methods, remarkable efficiencies have been achieved; however, their experimental procedures are sometimes difficult to reproduce. Solvent annealing (SA) can be applied to perovskite films to increase the crystallinity and grain size effectively. Xiao *et al.* previously employed the SA technique with a long annealing time (100 °C for 1 h) to increase the grain size of the perovskite film fabricated by two-step spin-coating.[21)] Recently, Zhou *et al.* have also used the solvent-solvent extraction concept in the fabrication of high-quality hybrid-perovskite thin films with a grain size of ~ 100 nm.22)

We showed that high-quality, uniform and reproducible planar $MAPbI_3$ PSCs can be fabricated by facile one-step solution deposition and antisolvent bath (ASB) methods in ambient air at a relative humidity (RH) >30%. The SA treatment method was incorporated to control the grain growth and morphology of the resultant perovskite film, which led to significant improvements in the photophysical properties of the film. The SA device achieved an average PCE of 15.20% and the highest efficiency of 16.77% under air mass global (AM 1.5G) spectrum illumination.

4.2 Preparation of perovskite film

The perovskite layer was prepared by dissolving PbI_2 (2 M) and MAI (2.39 M) in a mixed solvent of *N*-methyl-2-pyrrolidone (NMP) (1 ml) and γ-butyrolactone (GBL) (0.2 ml) and stirred at room temperature for 12 h to form the $MAPbI_3$ precursor solution. Next, the precursor solution was dropped onto the compact TiO_2 film to prepare the $MAPbI_3$ film as shown in Fig. 4.1a. The spin-coating process was performed at a constant rotation speed of 4500 rpm for 30 s without acceleration time. The solution-coated substrate was carefully dipped immediately in a beaker containing about 50 ml of anhydrous diethyl ether (DEE) bath.22) The substrate was kept immersed for the 90s until it turned dark brown with a glossy appearance. The substrate was removed from the DEE bath and dried in ambient air. The obtained $MAPbI_3$ films were approximately 250 nm thick. The films were further treated by SA at 150 °C for 10 min under DMSO vapor atmosphere as shown in Fig. 4.1a. For the SA, the perovskite film was put on top of a hotplate and covered with a petri dish. At the edge of the petri dish, 10μl of dimethylsulfoxide (DMSO) solvent was dropped during annealing.21) As the control samples, pristine perovskite films without annealing and perovskite films with thermal annealing (TA) at 150 °C for 10 min in ambient air were also prepared.

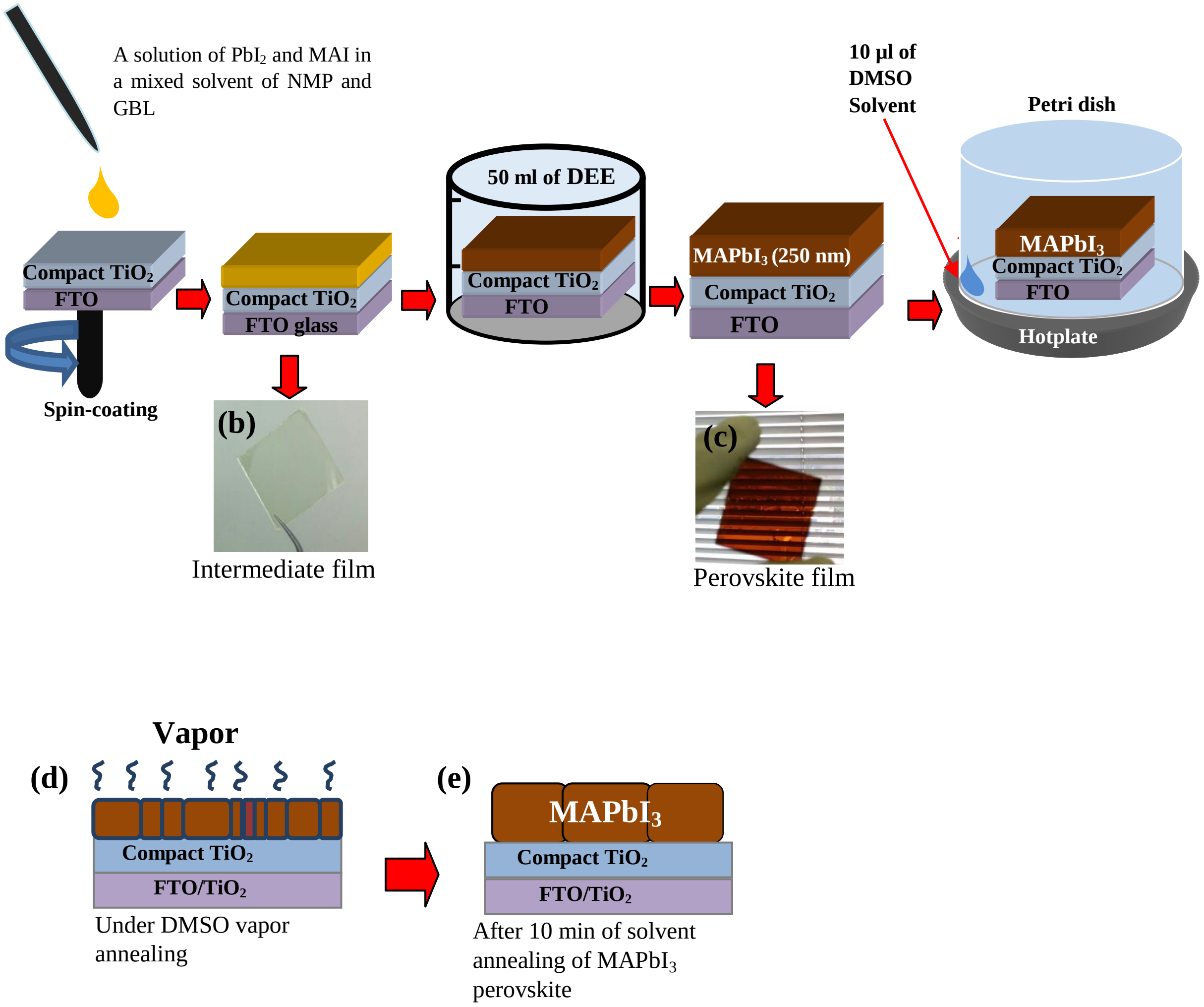

Fig. 4.1 (a) Schematic diagram of perovskite film fabricated by one-step spin-coating and ASB methods, and SA treatment method under DMSO solvent vapor (The photographs represent that of (b) the precursor solution-coated substrate and (c) the as-prepared $MAPbI_3$ perovskite film after 90 s of bathing in a beaker containing 50 ml of DEE) (d) Illustration of $MAPbI_3$ perovskite grain growth by a dissolution and precipitation process under DMSO vapor environment. (e) Illustration of enlarge grains of the $MAPbI_3$ perovskite after SA treatment.

4.3 Results and discussion

The $MAPbI_3$ perovskite was deposited by the one-step solution process and ASB method onto the FTO/compactTiO_2 substrate by spin-coating from a solution of PbI_2 and MAI in a mixed solvent of NMP and GBL, as shown in Fig. 4.1(a) (see Sect. 4.2).The solution-coated substrate exhibited an extremely dense and uniform MAI-PbI_2-NMP-GBL intermediate film [see a photograph of Fig. 4.1(b)]. Furthermore, the antisolvent DEE, which has a low boiling point and no solubility or reactivity with the perovskite precursors was adopted to extract the NMP and GBL solvents from the spin-coated solution film, and this led to a uniform, highly smooth and glossy $MAPbI_3$ perovskite film [see photograph of Fig.4.1(c)].22). DMSO solvent was chosen for SA due to its remarkable coordinating capability with MAI-PbI_2.23,24) For SA treatment, the DMSO vapor would condense on the surface of $MAPbI_3$ inside the petri dish, and consequently, a solid-liquid phase of $MAPbI_3$ is formed [Fig. 4.1 (d)].25,26) As shown in Fig. 4.1 (d), the DMSO solvent molecules in the $MAPbI_3$ film will facilitate the rearrangement of the precursor atoms, inducing the atom packing in a regular array structure.27) Upon gradual release of the DMSO, the $MAPbI_3$ perovskite forms and crystallizes in a semi-equilibrium form.

4.3.1 Morphological characterization

Figure 4.2 (a) shows an AFM image of the resultant perovskite film (hereafter referred to as the as-prepared perovskite film) with a homogeneous and smooth surface. The root mean square (RMS) roughness determined by AFM is 8.3 nm, which is relatively small, suggesting the benefit of the ASB process. However, as shown in Figs. 4.3 (a) and 4.3 (b), the SEM images of the as-prepared perovskite film consist of small grains with a significant amount of grain boundaries that covered the compact TiO_2 layer underneath.

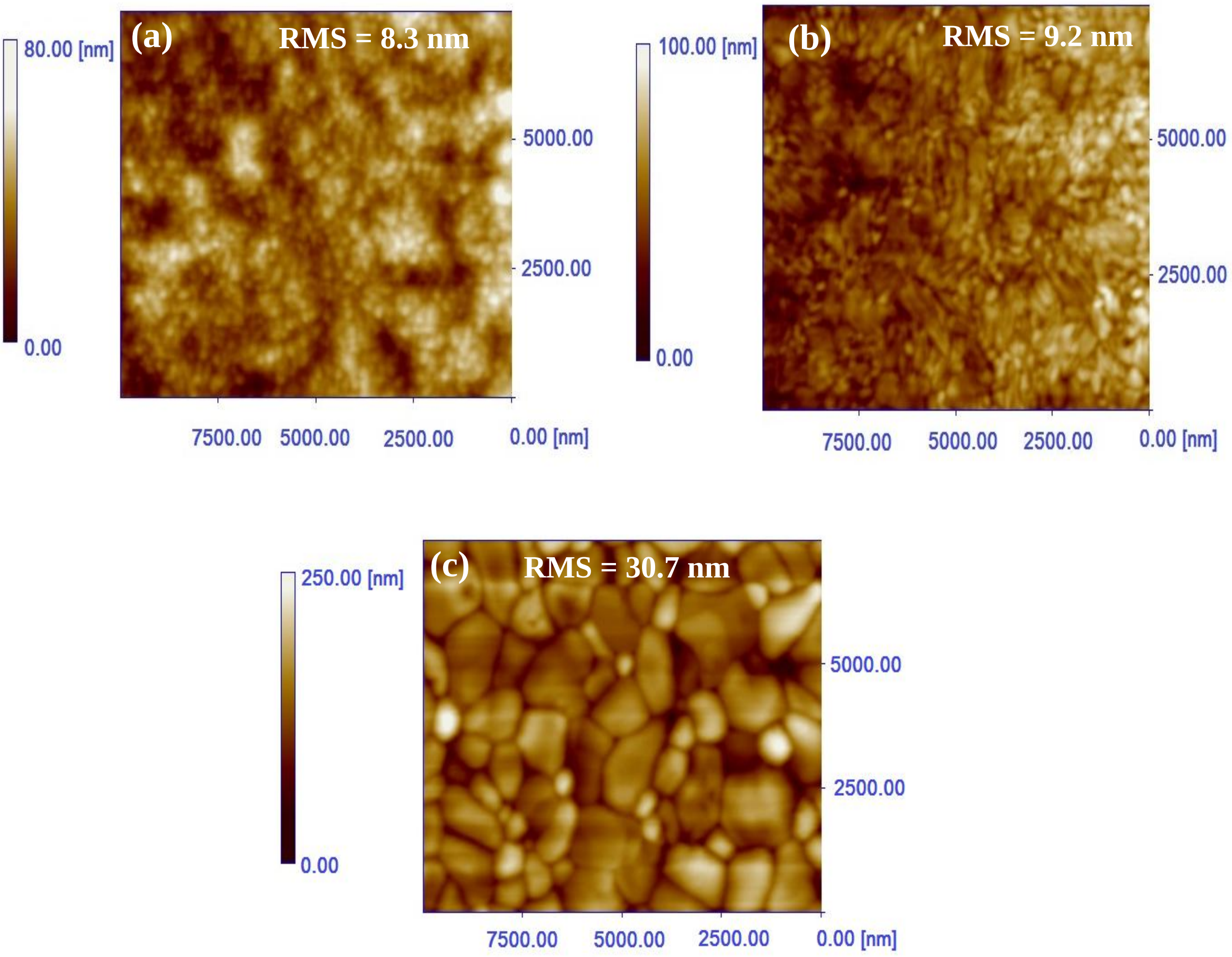

Fig. 4.2 AFM images of (a) the as-prepared perovskite film, (b) TA perovskite film, and (c) SA perovskite film.

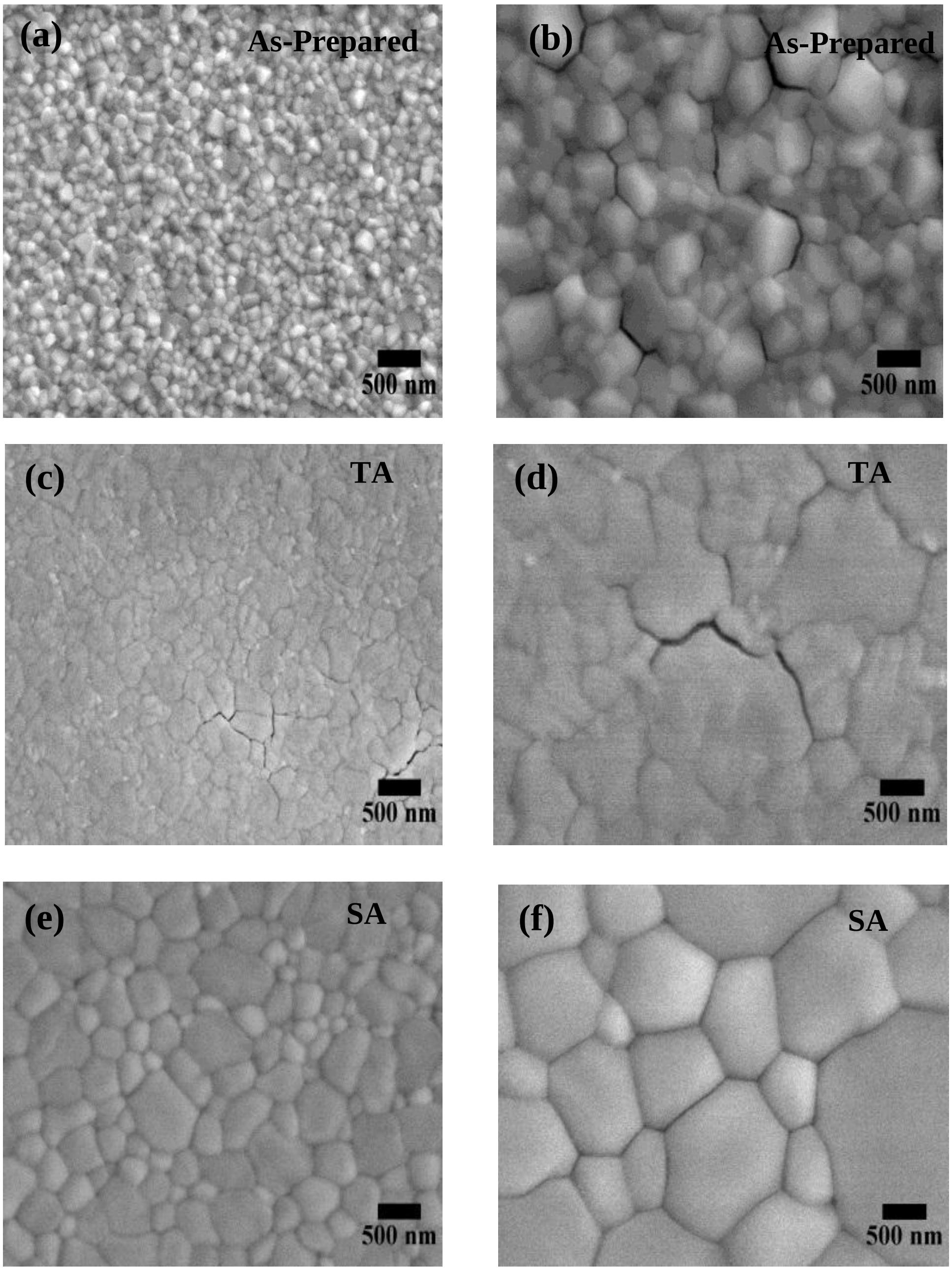

Fig. 4.3 (a) Low magnification of SEM image, (b) High magnification of SEM image of the as-prepared perovskite film. (c) Low magnification of SEM image, (d) High magnification of SEM image of TA film. (e) Low magnification of SEM image SA, (f) High magnification of SEM image of SA film.

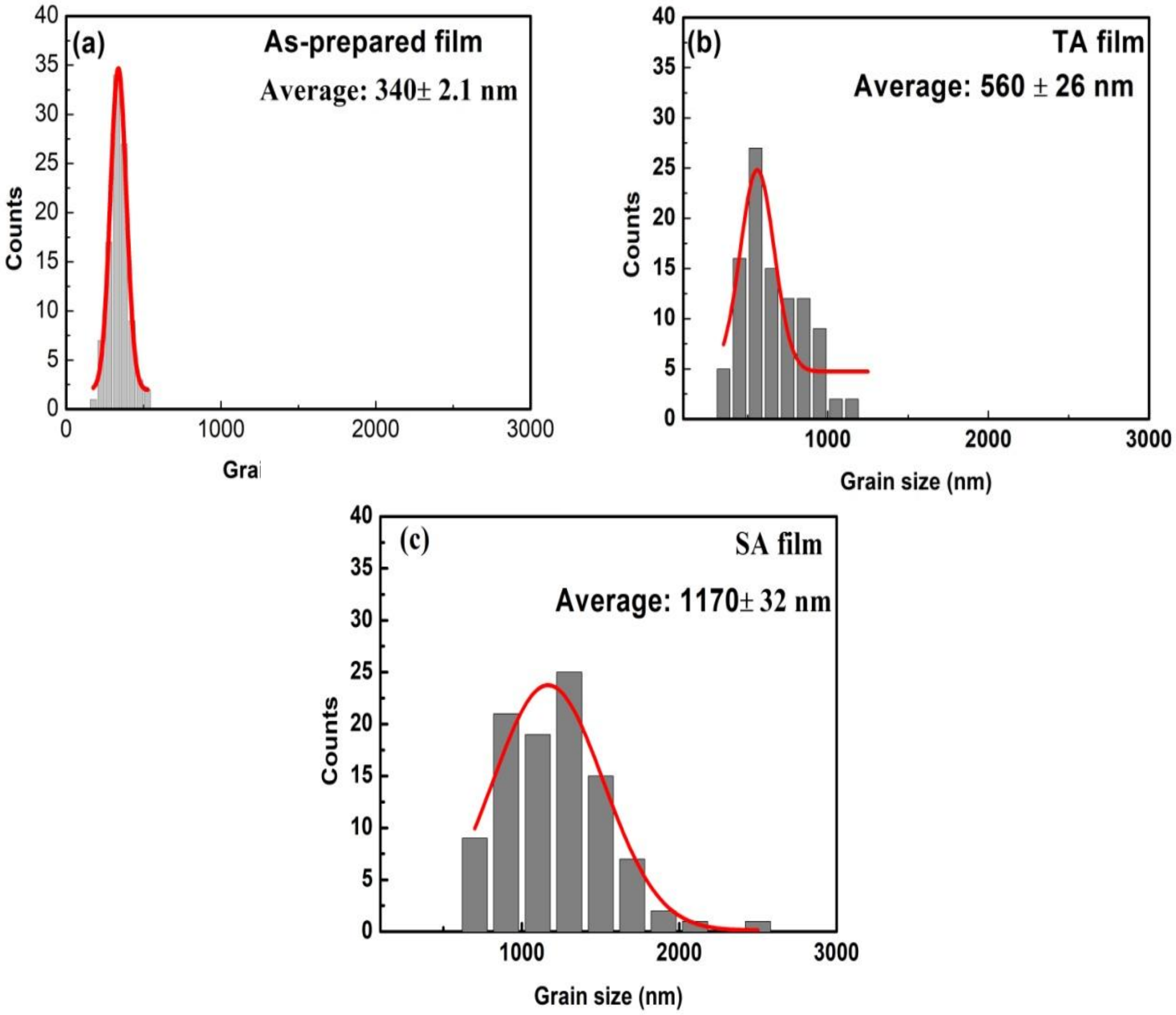

Fig. 4.4 Grain size distributions of (a) as-prepared, (b) TA, and (c) SA perovskite films.

The grain size distribution of the as-prepared film, which was determined from SEM images, using the image analysis software (Nano Measure), is shown in Fig. 4.4 (a). The as-prepared perovskite film exhibited an average grain size of 340 ± 2.1 nm. To improve the microstructure of the as-prepared film, TA was applied. The RMS roughness of the TA perovskite film was found to increase by about 10% [Fig. 4.2 (b)], which may be due to the increased grain size. The SEM images of the TA perovskite film also confirmed the increased grain size [Figs. 4.3 (c) and 4.3 (d)]. As shown in Fig. 4.4 (b), the TA perovskite film consists of crystals with an average size of 560 ± 26 nm. It has been shown that TA treatment could be used to increase the grain size of the as-prepared perovskite film to a certain degree; however, the margin is not so pronounced and further increasing the TA time could decompose the $MAPbI_3$ perovskite films without markedly increasing the grain size.[21)] Interestingly, upon SA treatment, grain growth and merging were observed [Figs. 4.3(e) and 4.3 (f)]. The SA perovskite film exhibited grains with an average size of 1170 ± 32 nm as shown in Fig. 4.4 (c).The AFM image is shown in Fig.4.2 (c) also confirmed the increased grain size of the SA perovskite film with an RMS roughness of 30.7 nm. It was found that the film growth increased the surface roughness. Despite the relatively higher RMS roughness of the SA perovskite film, the film still retained its uniform surface, which is critical for high-performance planar devices.

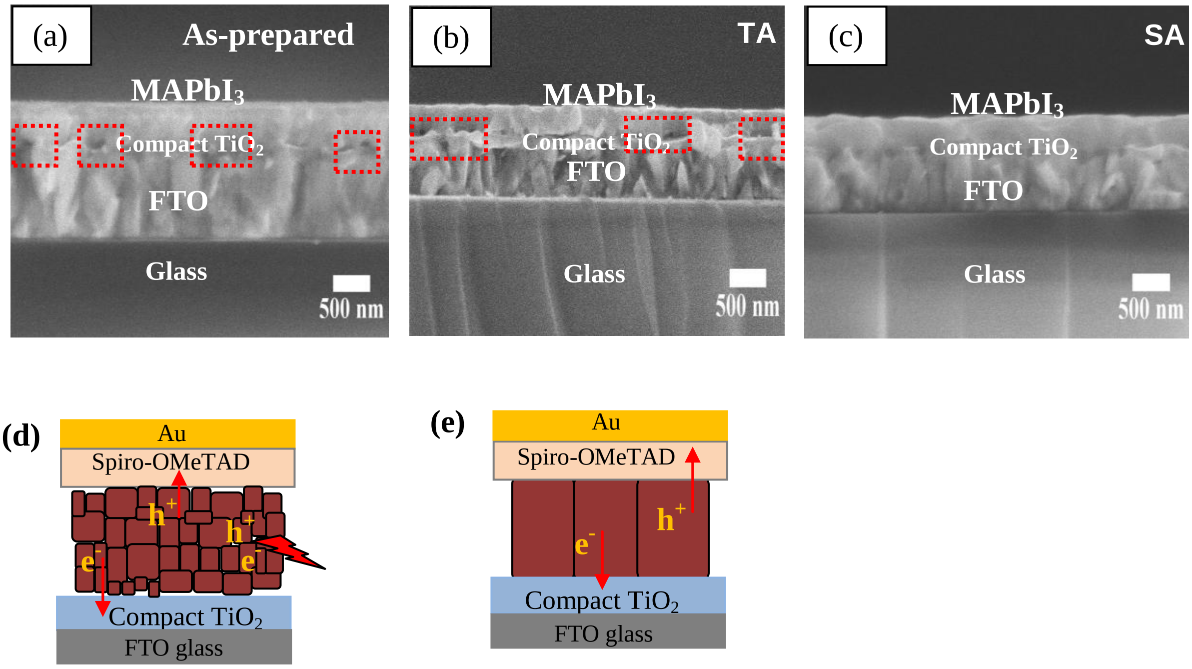

Fig. 4.5 Cross-sectional SEM images of the (a) as-prepared, (b) TA, and (c) SA $MAPbI_3$ Perovskite films. Charge transport model of (d) $MAPbI_3$ perovskite without SA treatment, the electron and hole recombine due to many grain boundaries and crystal defects. (e) With SA treatment. The grain boundary effects is alleviated by SA treatment.

Figure 4.5 shows the cross-sectional SEM images of as-prepared, TA, and SA perovskite films and charge transport model of $MAPbI_3$ perovskite film prepared with and without SA treatment. It is found that void areas (red boxes) appeared at the compact TiO_2/perovskite interface for the as-prepared and TA perovskite films [Figs. 4.5 (a) and 4.5 (b)]. These void areas observed in both films suggest that the films exhibit low uniformity at the compact TiO_2/perovskite interface and may act as shunt paths that could lead to a direct contact between Spiro-OMeTAD and the compact TiO_2 layer [Fig. 4.5 (d)].28) As shown in Fig. 4.5 (c), the SA perovskite film shows high uniformity at the compact-TiO_2/perovskite interface, which suggests its importance in the fabrication of high-performance planar PSCs. It is worth mentioning that highly uniform perovskite film with enlarging grains and fewer grain boundaries will promote efficient charge transport in the device and thus enhance the device performance [Fig. 4.5 (e)].

4.3.2 Structural and optical characterization

Figure 4.6 (a) shows the XRD patterns of the as-prepared, TA, and SA perovskite films. The strong diffraction peaks located at 2θ values of 14.08, 28.41, and 31.86° can be assigned to (110), (220), and (310) planes of the tetragonal $MAPbI_3$ phase, respectively. The full widths at half maximum (FWHMs) of the characteristic (110) peak were estimated to be 0.487, 0.310, and 0.116° for the as-prepared, TA, and SA perovskite films, respectively. Phase-pure $MAPbI_3$ perovskite was observed in all the films, indicating the complete crystallization of the perovskites.

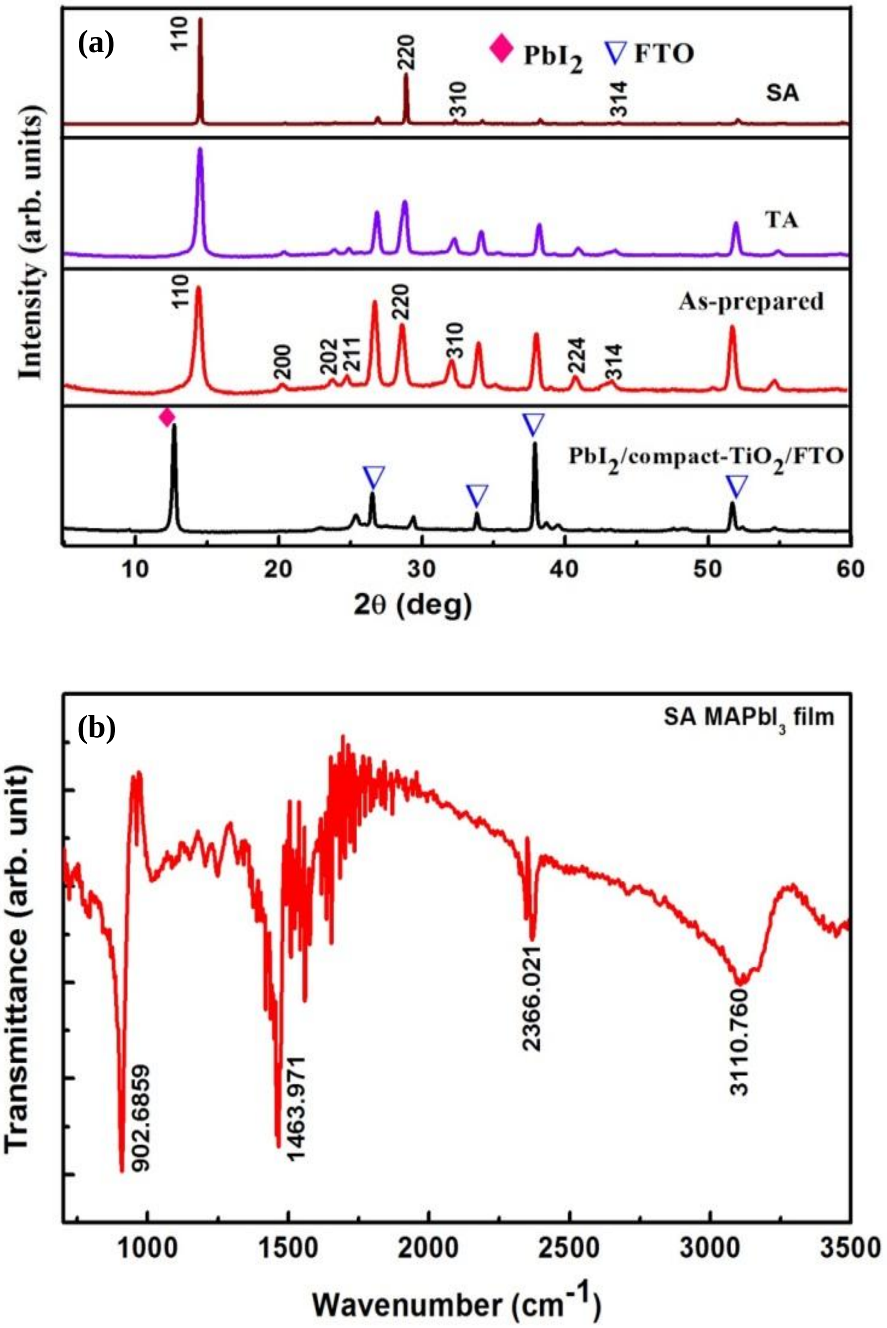

Fig. 4.6 (a) XRD patterns of PbI_2, as-prepared, TA, and SA $MAPbI_3$ perovskite films on FTO/compact TiO_2 substrates. (b) FTIR spectrum of the SA $MAPbI_3$ perovskite film.

The characteristic (110) peak for the SA perovskite film appeared stronger and sharper than those for the as-prepared and TA perovskite films, suggesting the higher crystallinity of the SA perovskite film with fewer defects. The higher crystallinity obtained by the SA film is an important factor for improving the photophysical properties,29) and performance of perovskite solar cells.8,16,21) In order to confirm the compositional purity of the SA $MAPbI_3$ perovskite film, the film was characterized by FT-IR as shown in Fig. 4.6 (b). The characteristic peaks of DMSO at around 960 and 1012 cm^{-1} could not be identified in the spectrum,12) suggesting that no residual DMSO existed within or on the surface of the perovskite film after the SA treatment.

We further investigated the effects of SA on the light absorption and photoluminescence properties of the perovskite films. Figure 4.7 (a) shows the absorption spectra of the perovskite films. The perovskite films showed an absorption edge at approximately 780 nm. An enhanced absorption between 800 and 400 nm regions was observed for the SA perovskite film, while the as-prepared and TA films showed almost similar light absorptions. The enhanced light absorption of the SA film may be related to the improved perovskite morphology and crystallinity.21)

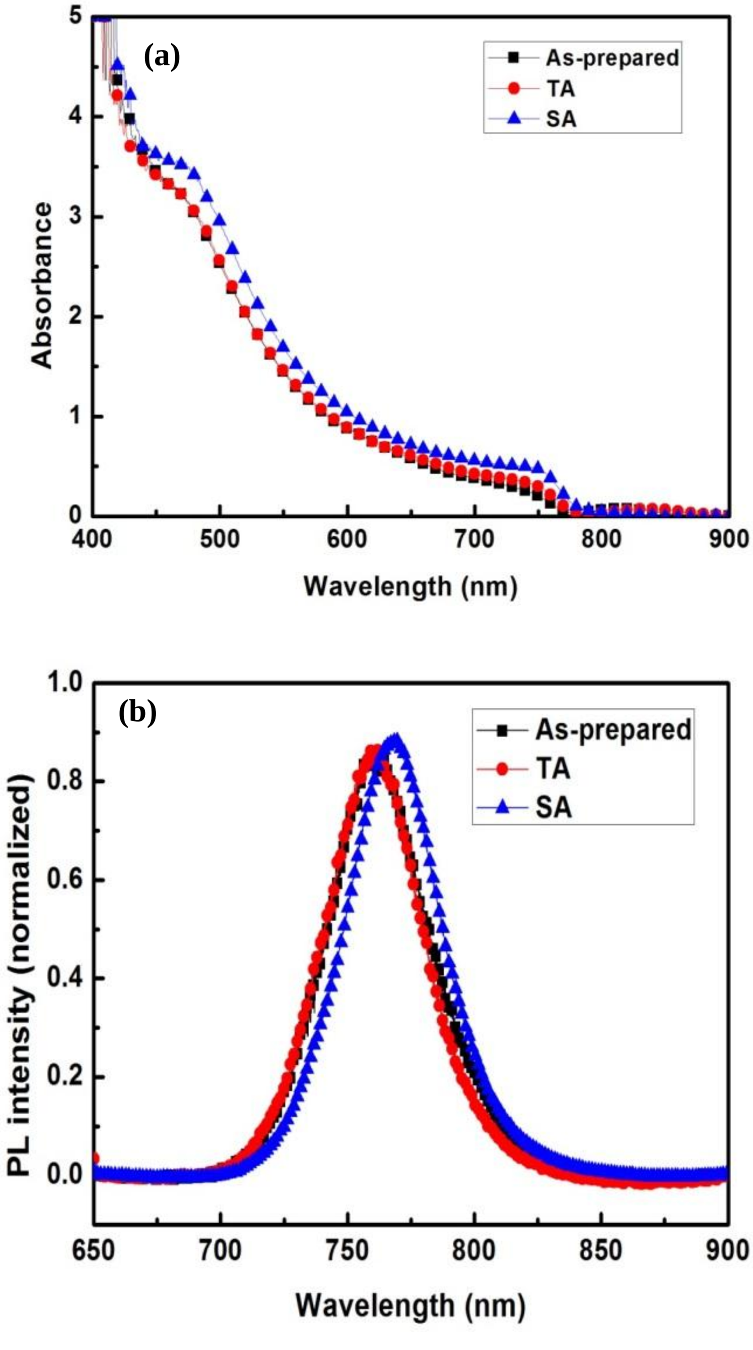

Fig. 4.7 (a) UV-vis absorption and (b) PL spectra of the as-prepared, TA, and SA perovskite films deposited on the FTO/compact TiO_2 and glass substrates, respectively.

The steady-state PL spectra of the perovskite films on glass substrates were measured as shown in Fig. 4.7 (b). The as-prepared and TA perovskite films exhibited similar emission peaks at about 760 nm, while the SA perovskite film exhibited an emission peak at about 770 nm. The PL result of the SA perovskite film showed a redshift, suggesting perovskite domains with fewer defect states in bulk.10) Usually, the PL emission is related to the recombination channel associated with the band gap and trap state. The redshift observed for the SA perovskite film demonstrates that in the SA treatment, the DMSO vapor contributes to the elimination of defects and decreases the trap density around the band edge, which could reduce the recombination loss and thus enhance the device photocurrent collection.

4.3.3 Photovoltaic performance characterization

The effect of SA on the device performance was evaluated using the device structure of FTO/compact TiO_2 (50 nm)/$MAPbI_3$ (250 nm)/Spiro-OMeTAD (250 nm)/Au (80 nm). For comparison, devices incorporating the as-prepared and TA perovskite films were also fabricated. Figure 4.8(a) shows the *J–V* curves (reverse scan) of the perovskite solar cells measured under AM 1.5G, 100 mW/cm^2 light illumination. The PV parameters of our top-performing and average-performing devices, together with the standard deviation of measurements of 16 devices, are summarized in Table 1. The as-prepared perovskite solar cell (without annealing) showed a short-circuit current (J_{sc}) of 22.20 mA/cm^2, an open circuit voltage (V_{oc}) of 0.861, a fill factor (FF) of, 0.570, and a PCE of 10.90%. Similarly, for the TA device, an overall PCE of 12.83% was achieved with a J_{sc} of 22.64 mA/cm^2, a V_{oc} of 0.884 V, and an FF of 0.641. When SA treatment was carried out, the device exhibited a higher J_{sc} of 23.65 mA/cm^2, a V_{oc} of 1.01 V, an FF of 0.702, and a PCE of 16.77%. The average PCEs of the as-prepared, TA, and SA devices are 9.44±0.81, 11.82±0.80, and 15.20±1.00%, respectively, thereby proving the high reproducibility of our devices and as well as the benefit of using the one-step solution process and ASB method. The higher PCE obtained by the SA device could be attributed to the enlarge perovskite grains with fewer bulk defects, less scattering of grain boundaries, improved crystallinity and charge transport [Fig. 4.5 (e)].10,21,29)

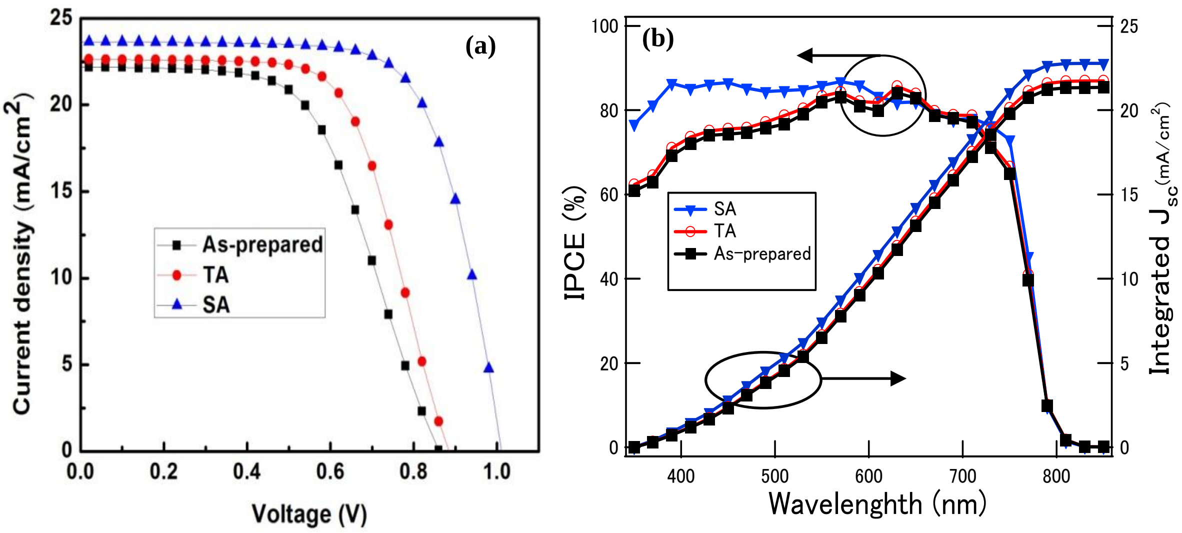

Fig. 4.8 (a) *J–V* curves of the as-prepared, TA, and SA PSCs measured under reverse voltage scanning and AM 1.5G illumination. (b) IPCE spectra of the as-prepared, TA, and SA devices.

The presence of large grains may promote improved charge extraction efficiency and markedly reduce charge recombination loss at grain boundaries in the device. Figure 4.8 (b) shows the IPCE spectra of the as-prepared, TA, and SA perovskite solar cells. As can be seen in the IPCE response, the SA device starts to deviate at around 780 nm and consistently above 80% within the visible wavelength range from 350 to 620 nm, suggesting higher charge collection efficiency. The integrated J_{SC} values from IPCE curves for SA (22.79 mA/cm^2), TA (21.74 mA/cm^2), and as-prepared (21.35 mA/cm^2) solar cells are in good agreement with the experimentally measured J_{sc} value under the simulated AM 1.5G illumination of 100 mW/cm^2.

Table 1. PV parameters of the as-prepared, TA, and SA PSCs measured under reverse voltage scanning. The values in parentheses correspond to the average values from 16 solar cells and the corresponding standard deviation.

Device	Annealing time (min)	J_{sc} (mA/cm^2)	V_{oc} (V)	FF	PCE (%)
As-prepared (best)	0	22.20	0.861	0.570	10.90
As-prepared (average)		(22.05±0.18)	(0.840±0.011)	(0.51±0.04)	(9.44±0.81)
TA (best)	10	22.64	0.884	0.641	12.83
TA (average)		(22.55±0.05)	(0.861±0.012)	(0.610±0.03)	(11.82±0.80)
SA (best)	10	23.65	1.010	0.702	16.77
SA (average)		(23.38±0.14)	(1.000±0.008)	(0.65±0.04)	(15.20±1.00)

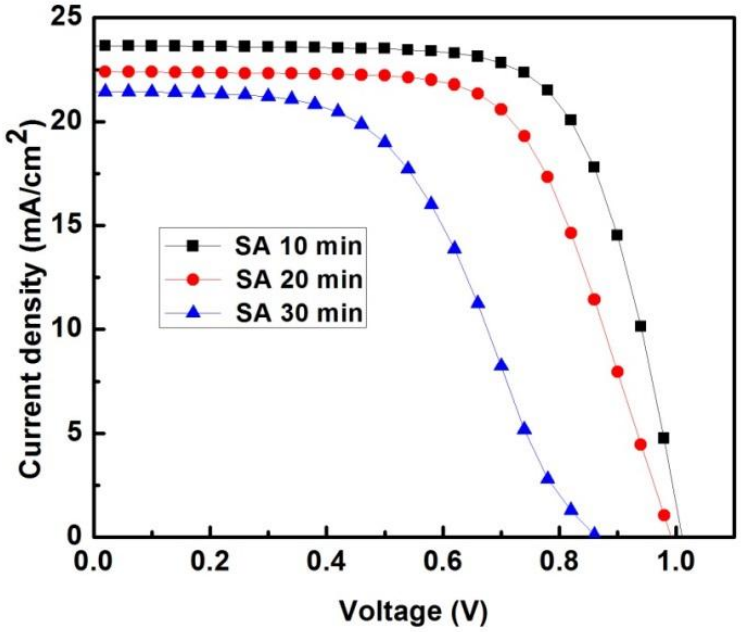

Fig. 4.9 *J-V* curves of PSCs with different SA durations.

Table 2. Summary of the PV parameters for the PSCs with SA for 20 and 30 min measured under the reverse voltage scanning.

Devices	Annealing time (min)	J_{SC} (mA/cm^2)	V_{OC} (V)	FF	PCE (%)
SA	20	22.41	1.000	0.650	14.57
SA	30	21.44	0.860	0.520	9.59

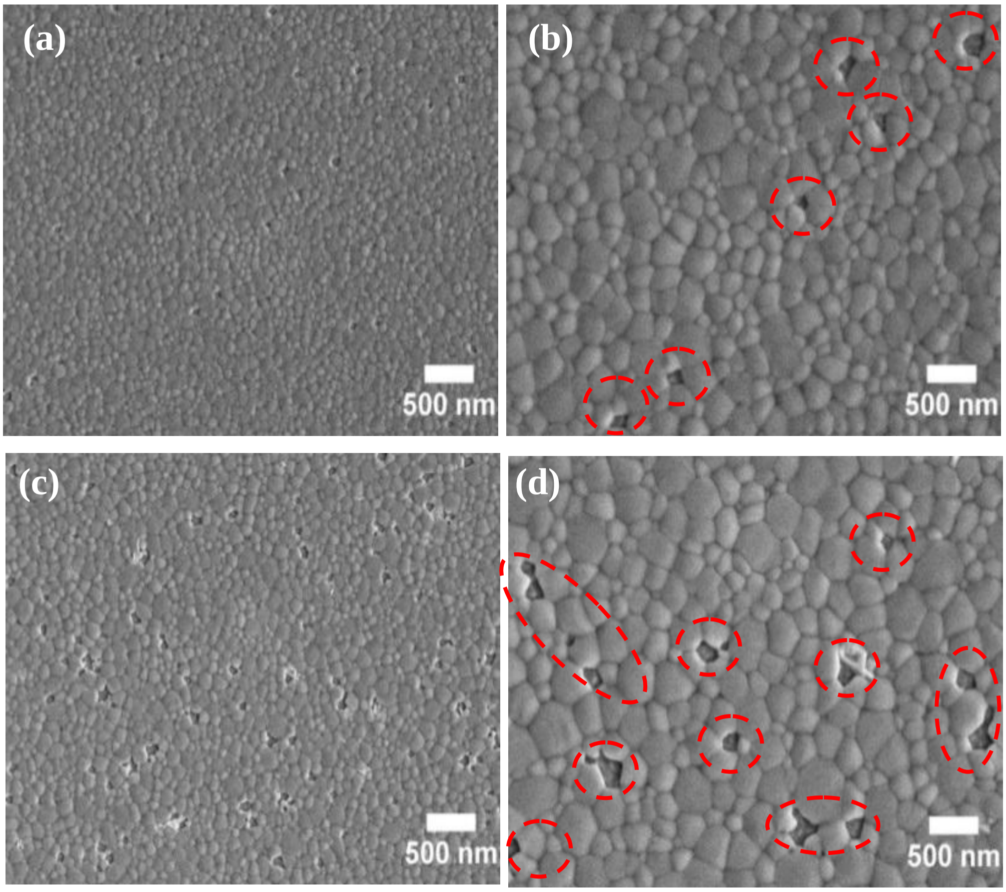

Fig. 4.10 Low and high magnifications of SEM images of SA perovskite films. (a, b) annealed for 20 min and (c, d) annealed for 30 min.

In order to gain further insight into the effect of SA duration on the device performance, PSCs with SA treatment for 20 and 30 min were also fabricated. Figure 4.9 shows the *J-V* curves of PSCs with different SA durations. A summary of the PV parameters of SA for 20 and 30 min is shown in Table 2. Compared with the device incorporating SA for 10 min (optimum SA time) listed in Table 1, the device with the perovskite film with SA for 20 min showed a relatively lower PCE of 14.57%, with V_{oc}, J_{sc}, and FF of 1.000 V, 22.41 mA/cm^2, and 0.650, respectively. Further increasing the SA duration to 30 min, however, was not favorable for the solar cell performance, where a lower PCE of 9.59%, a V_{oc} of 0.860 V, and an FF of 0.520 were achieved. Compared with the best- performing PSCs (SA for 10 min), the drop in the PV parameters for both devices with 20 and 30 min SA treatment devices stems from the poor coverage, which was caused by the decomposed (red spheres) perovskite films, as shown in Fig. 4.10. The poor coverage of perovskite may have caused (1) light to pass straight through the perovskite film without absorption, decreasing the available photocurrent, and (2) a high frequency of shunt paths, which would enable contact between the HTM layer and the compactTiO_2 layer.$^{30)}$ Both of these effects can unavoidably decrease J_{sc}, V_{oc}, FF and consequently PCE. As shown in Figs. 4.10(a) and 4.10(b), the perovskite film with SA for 20 min was slightly decomposed compared with that with SA for 30 min [Figs.4.9(c) and 4.9(d)]. With increasing SA time (>10 min), $MAPbI_3$ perovskite films were decomposed owing to the high substrate temperature (150 °C),$^{31,32)}$ and not the DMSO solvent vapor. However, with the films on the hotplate, 10 µl of DMSO dropped at the edge of the petri dish will produce limited solvent vapor pressure and evaporated solvent molecules, which would not cause wide-range dissolution and irreparable damage, but probably lead to the formation of a quasi-liquid phase on the surface and void areas of the perovskite film. The liquid phase could act as a binder, which bonds with adjacent grains, remolds a significant portion of the grain boundary, and then recrystallizes in areas where grains are not in contact, and thus leading to films with higher quality and morphology.$^{25,33)}$

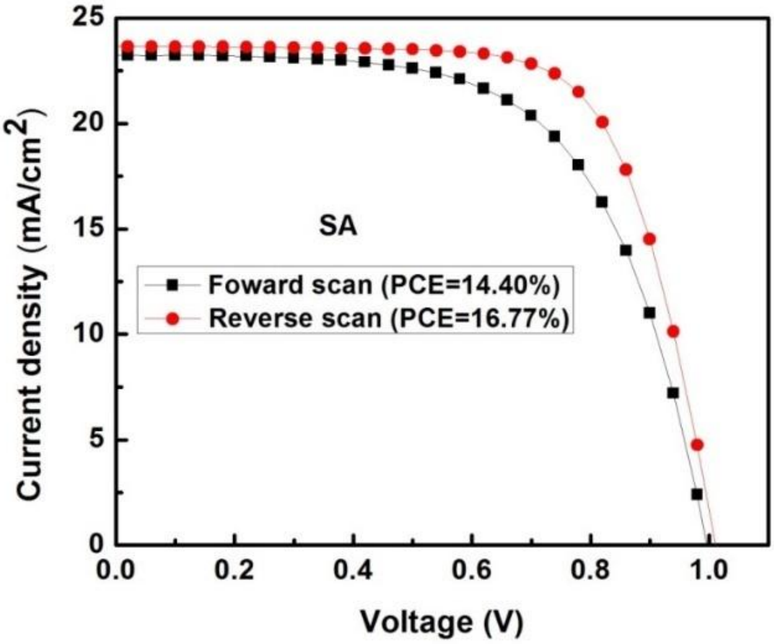

Fig. 4.11 *J*–*V* curves (forward and reverse scans) of SA (10 min) device.

Hysteresis is one of the most critical issues for planar PSCs in the *J*–*V* measurement. Typically, the origin of hysteresis can be either the trapping and de-trapping of charge carriers,34) changes in the absorber or contact conductivity, 35) ferroelectric properties of the perovskite materials, 36) and the electro-migration of ions in the perovskites.37) The forward scan (from the short circuit to the open circuit) and reverse scan (from the open circuit to the short circuit) of the SA (10 min) device are presented in Fig. 4.11. For the *J*–*V* measurement, a scanning speed of 0.2 V/s was adopted for both the forward and reverse scans. The SA device showed a hysteresis behavior and the hysteresis may be related to the poor electronic contact existing between the perovskite and compact TiO_2 layer.38,39)

4. 4 Conclusions

We have incorporated the SA treatment technique in combination with the one-step spin-coating and ASB methods to fabricate high-performance $MAPbI_3$ planar PSCs. The SA treatment led to the improved the $MAPbI_3$ perovskite morphology and crystallinity. The high uniformity at the compactTiO_2/perovskite interface was achieved by SA for 10 min as confirmed by the cross-sectional SEM images. Further increasing the SA duration from 20 to 30 min led to severe decomposition of the perovskite film. The steady-state PL result showed that the SA perovskite film has relatively fewer defects and a low trap density around the band edge, which lead to the reduced recombination loss and enhanced PV performance of the device. The best-performing SA device achieved a PCE up to 16.77% and an average PCE of 15.20±1.00. The combination of SA, one-step spin-coating and ASB methods offered a simple and efficient way to fabricate high-quality planar perovskite films for high-performance PSCs.

4.5 References

1) M. Liu, M. B. Johnston, and H. J. Snaith, Nature **501**, 395 (2013).

2) H. Zhou, Q. Chen, G. Li, S. Luo, T.-B. Song, H.-S. Duan, Z. Hong, J. You, Y. Liu, and Y.Yang, Science **345**, 542 (2014).

3) P. Docampo, J. M. Ball, M. Darwich, G. E. Eperon, and H. J. Snaith, Nat.Commun.**4**,2761 (2013).

4) J. Burschka, N. Pellet, S.-J. Moon, R. Humphry-Baker, P. Gao, M. K. Nazeeruddin, andM. Grätzel, Nature **499**, 316 (2013).

5) V. O. Eze, B. Lei, and T. Mori, Jpn. J. Appl. Phys.**55,** 02BF08 (2016).

6) J.-H. Im, I.-H. Jang, N. Pellet, M. Grätzel, and N.-G. Park, Nat.Nanotechnol.**9**, 927 (2014).

7) Q. Chen, H. Zhou, Z. Hong, S. Luo, H.-S. Duan, H.-H. Wang, Y. Liu, G. Li, and Y. Yang, J. Am. Chem. Soc.**136**, 622 (2013).

8) A. Dualeh, N. Tétreault, T. Moehl, P. Gao, M. K. Nazeeruddin, and M. Grätzel, Adv. Funct. Mater.**24**, 3250 (2014).

9) E. Edri, S. Kirmayer, A. Henning, S. Mukhopadhyay, K. Gartsman, Y. Rosenwaks, G. Hodes, and D. Cahen, Nano Lett.**14**, 1000 (2014).

10)W. Nie, H. Tsai, R. Asadpour, J.-C. Blancon, A. J. Neukirch, G. Gupta, J. J. Crochet, M. Chhowalla, S. Tretiak, and M. A. Alam, Science **347**, 522 (2015).

11) L. Zuo, Z. Gu, T. Ye, W. Fu, G. Wu, H. Li, and H. Chen, J. Am. Chem. Soc.**137**, 2674 (2015).

12) N. J. Jeon, J. H. Noh, Y. C. Kim, W. S. Yang, S. Ryu, and S. I. Seok, Nat. Mater.**13**, 897(2014).

13) M. Xiao, F. Huang, W. Huang, Y. Dkhissi, Y. Zhu, J. Etheridge, A. Gray-Weale, U. Bach, Y. B. Cheng, and L. Spiccia, Angew. Chem.**126**, 10056 (2014).

14) H.-L. Hsu, C.-C. Chang, C.-P. Chen, B.-H. Jiang, R.-J. Jeng, and C.-H. Cheng, J. Mater. Chem. A **3**, 9271 (2015).

15) Y.-J. Jeon, S. Lee, R. Kang, J.-E. Kim, J.-S. Yeo, S.-H. Lee, S.-S. Kim, J.-M. Yun, andD.-Y. Kim, Sci.Rep.**4**,6953 (2014).

16) P. W. Liang, C. Y. Liao, C. C. Chueh, F. Zuo, S. T. Williams, X. K. Xin, J. Lin, and A. K. Y. Jen, Adv.Mater.**26**, 3748 (2014).

17) X. Song, W. Wang, P. Sun, W. Ma, and Z.-K. Chen, Appl. Phys. Lett.**106**, 033901 (2015).

18) C.-G. Wu, C.-H. Chiang, Z.-L. Tseng, M. K. Nazeeruddin, A. Hagfeldt, and M. Grätzel,Energy Environ. Sci.**8**, 2725 (2015).

19) J. You, Y. M. Yang, Z. Hong, T.-B. Song, L. Meng, Y. Liu, C. Jiang, H. Zhou, W.-H. Chang, and G. Li, Appl. Phys. Lett.**105**, 183902 (2014).

20) B. Yang, O. Dyck, J. Poplawsky, J. Keum, A. Puretzky, S. Das, I. Ivanov, C. Rouleau, G. Duscher, and D. Geohegan, J. Am. Chem. Soc.**137**, 9210 (2015).

21) Z. Xiao, Q. Dong, C. Bi, Y. Shao, Y. Yuan, and J. Huang, Adv. Mater.**26**, 6503 (2014).

22) Y. Zhou, M. Yang, W. Wu, A. L. Vasiliev, K. Zhu, and N. P. Padture, J. Mater. Chem. A**3**, 8178 (2015).

23) F. Hao, C. C. Stoumpos, P. Guo, N. Zhou, T. J. Marks, R. P. Chang, and M. G. Kanatzidis, J. Am. Chem. Soc.**137**, 11445 (2015).

24) H. Miyamae, Y. Numahata, and M. Nagata, Chem. Lett.**9**, 663 (1980).

25) J. Liu, C. Gao, X. He, Q. Ye, L. Ouyang, D. Zhuang, C. Liao, J. Mei, and W. Lau, ACS Appl.Mater. Interfaces **7**, 24008 (2015).

26) B. Wang, K. Y. Wong, S. Yang, and T. Chen, J. Mater. Chem. A**4**, 3806 (2016).

27) T. Baikie, Y. Fang, J. M. Kadro, M. Schreyer, F. Wei, S. G. Mhaisalkar, M. Graetzel, and T. J. White, J. Mater. Chem. A **1**, 5628 (2013).

28) L. Huang, Z. Hu, G. Yue, J. Liu, X. Cui, J. Zhang, and Y. Zhu, Phys. Chem. Chem. Phys.**17**, 22015 (2015).

29) D. Liu, L. Wu, C. Li, S. Ren, J. Zhang, W. Li, and L. Feng, ACS Appl.Mater.Interfaces**7**, 16330 (2015).

30) G. E. Eperon, V. M. Burlakov, P. Docampo, A. Goriely, and H. J. Snaith, Adv. Funct. Mater.**24**, 151 (2014).

31) C. Bi, Y. Shao, Y. Yuan, Z. Xiao, C. Wang, Y. Gao, and J. Huang, J. Mater. Chem. A **2**, 18508 (2014).

32) C. Bi, Q. Wang, Y. Shao, Y. Yuan, Z. Xiao, and J. Huang, Nat.Commun.**6,**7747 (2015).

33) Z. Zhou, Z. Wang, Y. Zhou, S. Pang, D. Wang, H. Xu, Z. Liu, N. P. Padture, and G. Cui,Angew. Chem., Int. Ed.**54**, 9705 (2015).

34) H. J. Snaith, A. Abate, J. M. Ball, G. E. Eperon, T. Leijtens, N. K. Noel, S. D. Stranks, J. T.-W. Wang, K. Wojciechowski, and W. Zhang, J. Phys.Chem.Lett.**5**, 1511 (2014).

35) D. Staebler and C. R. Wronski, J. Appl. Phys.**51**, 3262 (1980).

36) A. Dualeh, T. Moehl, N. Tétreault, J. Teuscher, P. Gao, M. K. Nazeeruddin, and M. Grätzel, ACS Nano **8**, 4053 (2014).

37) W. Tress, N. Marinova, T. Moehl, S. Zakeeruddin, M. K. Nazeeruddin, and M. Grätzel, EnergyEnviron. Sci.**8**, 995 (2015).

38) A. K. Jena, H.-W. Chen, A. Kogo, Y. Sanehira, M. Ikegami, and T. Miyasaka, ACS Appl.Mater. Interfaces **7**, 9817 (2015).

39) C. Tao, S. Neutzner, L. Colella, S. Marras, A. R. S. Kandada, M. Gandini, M. De Bastiani, G. Pace, L. Manna, and M. Caironi, Energy Environ. Sci.**8**, 2365 (2015).

40) V. O. Eze, T. Mori, Jpn. J. Appl. Phys. 55, 122301 (2016).

Chapter 5

Effect of fullerene C_{60} electron extraction interface on the performance of WOx-based perovskite solar cells 74)

5.1 Introduction

In perovskite solar cells (PSCs), the charge selective contacts play a crucial role in an attempt to further improve the performance of the solar cells [1, 2]. Several robust and stable metal oxide-based electron extraction layer (EELs) such as titanium oxide (TiO_2) [3, 4], zinc oxide (ZnO) [5, 6], tin oxide (SnO_2) [7], and indium oxide (In_2O_3) [8], have been used successfully in the n-i-p-type PSCs. Among the metal oxides, TiO_2 has been widely used as EELs. However, high-temperature (>450 °C) treatment of TiO_2 EEL is apparently required to obtain a highly compact and crystallized structure for efficient PSCs [9]. High-temperature treatment tends to be unfavorable when considering the production cost and energy payback time of PSCs. Low-temperature TiO_2 has been introduced as an EEL in PSCs, but its low electron conductivity and mobility usually results in charge accumulation in the TiO_2 layer [10-13], and low PCE as shown in Fig. 5.1

Tungsten trioxides (WO_3) are chemically stable metal oxide semiconductors with bandgaps in the range of 2 to 3 eV and high electron mobility (10–20 $cm^2. V^{-1}. s^{-1}$) [14-17]. WO_3 has also received significant attention as a very interesting material for electrochromic devices [18,19], gas sensing [20, 21], photocatalysis [22], polymer and DSCs [16, 17, 23, 24]. Khalid *et al.* were the first to employ WO_3 as an EEL in PSCs and achieved impressive PCEs [25]. Following their pioneering work, Kai *et al.* showed that low-temperature amorphous tungsten oxide (WO_x) could be used as EELs in PSCs [26]. It was found that WO_x based PSCs suffer from severe charge recombination at the perovskite/WO_x interface, resulting in an unsatisfied open-circuit voltage (V_{oc}) and fill factor (FF). Chih-Ming *et al.* modified the perovskite/WO_3 interface with cesium carbonate (Cs_2CO_3)/phenyl-C_{61}-butyric acid methyl ester (PCBM) to further improve the performance of the device and achieved a PCE of 10.0% [27].

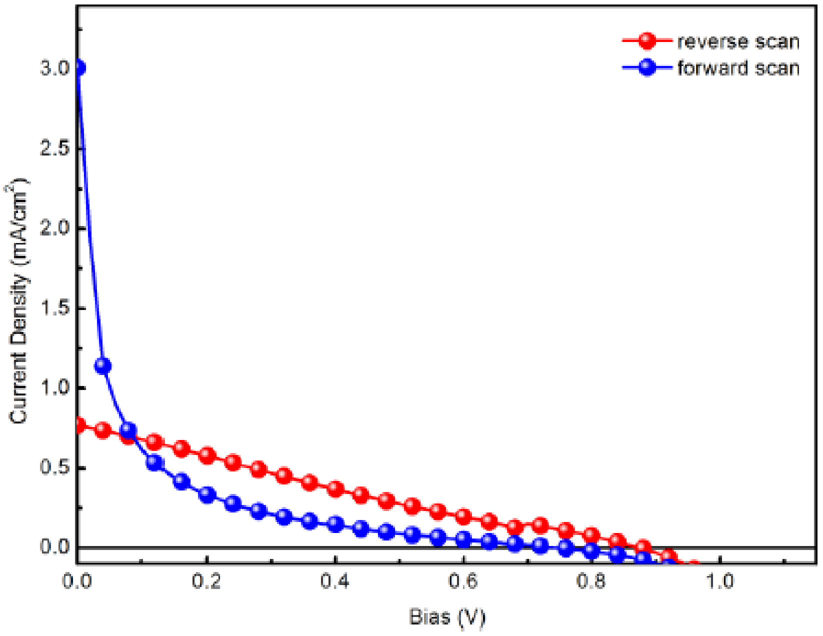

Fig. 5.1 Current density-voltage (*J*-*V*) curves of a TiO_x only device with the structure of $FTO/TiO_x/CH_3NH_3PbI_3$/spiro-MeOTAD/Au [13].

Kai *et al.* used WO_x –TiO_x composite thin films as EELs in PSCs. The WO_x–TiO_x composite EELs enabled a strong light transmittance, efficient charge transport, and dissociation, and as well as inhibition of the charge recombination, which notably increases the performance of the PSCs [28]. Kai *et al.* also demonstrated that amorphous niobium-modified tungsten oxide ($W(Nb)O_x$) could be used as EELs for efficient, flexible PSCs [29].

We propose the use of a low-temperature solution processed WO_x/fullerene C_{60} as excellent EELs for efficient planar PSCs. Fullerenes, such as C_{60} and PCBM have been used as excellent acceptors in organic solar cells [30-32], and EELs in PSCs [33-40]. According to previous reports, C_{60} and PCBM are excellent passivation materials for perovskite, which can effectively passivate the grain boundaries in the perovskite and reduce the density of trap states as well as reduce hysteresis of PSCs [41-43]. Moreover, fullerene C_{60} is a low-cost material that exhibits superior electron mobility (1.6 cm^2/V s) and conductivity (2.3 x 10^{-3} S cm^{-1}) than that of PCBM (6.1 x 10^{-2} cm^2/V s and 3.2 x 10^{-4} S cm^{-1}, respectively) [34]. Here, we incorporated C_{60} as an interface modifier for WO_x-based PSCs [36]. The WO_x/C_{60} EELs was found to work synergistically to further enhance the performance of PSCs. The best-performing planar PSCs using WO_x/C_{60} EELs achieved PCEs of 16.07% and 14.11% when measured under reverse and forward voltage scans, respectively. Such enhancement is mainly attributed to the improved V_{oc} and FF, benefiting from the better electron transfer and less charge recombination. This work shows that low-cost and high-performance PSCs can be achieved using WO_x/C_{60} EELs.

5.2 Results and discussion

5.2.1 Device structure and energy level

Fig. 5.2a shows the XRD patterns of the WO_x films annealed at 150 °C and 500 °C (crystalline WO_3). The film annealed at 150 °C shows only a broad feature at about 25°, suggesting an amorphous structure.

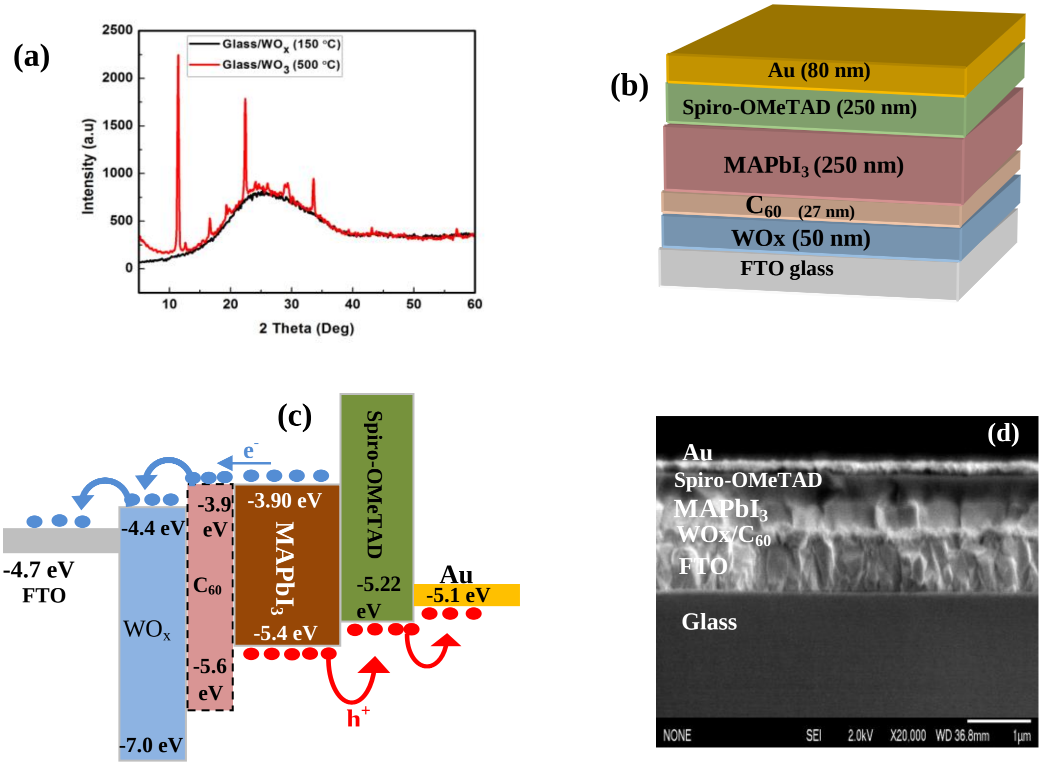

Fig. 5.2 (a) XRD pattern of WO_x and WO_3 films. (b) Schematic view of the device structure (c) Energy band diagram of planar PSC with a WO_x/C_{60} EELs and (d) Cross-sectional SEM image of our device.

In contrast, the film annealed at a higher temperature exhibits sharp crystalline peaks corresponding to monoclinic WO_3 [44, 45]. Fig. 5.2b shows the device architecture of a planar PSC, which consists of FTO/WO_x (50 nm)/C_{60} (27 nm)/$MAPbI_3$ (250 nm)/Spiro-OMeTAD (250 nm)/Au (80 nm). The fullerene C_{60} was introduced as an interface modifier between the WO_x and perovskite layers. The energy band diagram is shown in Fig. 5.2c. The conduction band minimums (CBMs), valence band maximums (VBMs) of WO_x and $MAPbI_3$ together with the lowest unoccupied molecular orbital (LUMO) and highest occupied molecular orbital (HOMO) levels of C_{60} were selected based on previous reports [24, 36]. The HOMO level of Spiro-OMeTAD and work function of Au were extracted from a previous report [46]. The LUMO of C_{60} (-3.9 eV) is equal to the CBM of $MAPbI_3$ can facilitate the smooth electron transfer from the $MAPbI_3$ to FTO. Fig. 5.2d shows the cross-sectional SEM image of our planar PSCs with the C_{60} interlayer. All layers are well-defined except for the C_{60} layer, which cannot be easily discerned from the cross-sectional image. High-quality $MAPbI_3$ perovskite films were deposited on the EELs by a simple one-step solution process and antisolvent bath (ASB) method in air. The morphology and grain growth of the resultant perovskite films were further improved by solvent-annealing under DMSO vapor atmosphere at 150 °C for 10 min [47]. The commercial p-type hole-transport material, Spiro-OMeTAD, was spin-coated on top of perovskite layer, and metal Au was evaporated on the Spiro-OMeTAD layer as a contact electrode.

5.2.2 Morphological characterization

Fig. 5.4a shows that the FTO exhibits a rough morphology with a root-mean-square (RMS) roughness of 24.5 nm (Fig. 5.3a). However, the RMS roughness was slightly reduced by depositing WO_x layer (Fig. 5.3b). The WO_x layer, which completely covered the FTO, contained many nanocaves (Fig. 5.4b and c). According to previous reports, these nanocaves might be due to the HCl volatilization as shown in the following reactions [26, 28, 48].

$$WCl_6 + xC_2H_5OH \longrightarrow WCl_{6-x}(OC_2H_5)x + x\,HCl \qquad (1)$$

$$WCl_{6-x}(OC_2H_5)x + (6-x)\,C_2H_5OH \longrightarrow W(OC_2H_5)_6 + (6-x)\,HCl \qquad (2)$$

When the FTO/WO_x film was coated with C_{60}, it was observed that the C_{60} molecules completely modified the WO_x layer, filled the nanocaves and reduced the RMS roughness of WO_x film (Figs. 5.3c and 5.4d). The smoother surface of the FTO/WO_x/C_{60} film should be favorable in enhancing the hole blocking ability, decreasing the leakage current at the EELs/perovskite interface and improving the device performance [49]. Figs. 5.5 (a) and (b) show the perovskite films deposited on

FTO/WO$_x$ and FTO/WO$_x$/C$_{60}$. Both films showed almost similar features that have uniform and highly compact morphologies.

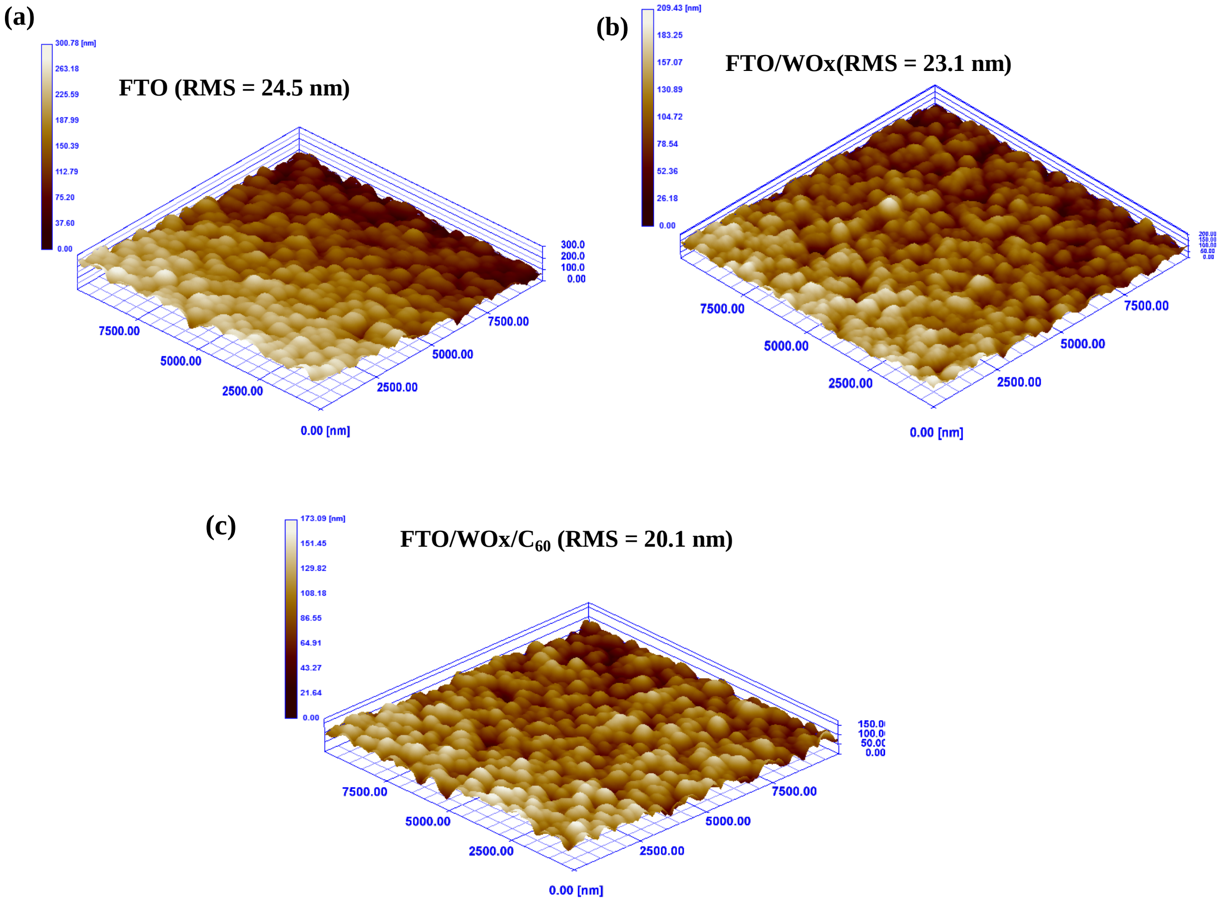

Fig. 5.3 AFM images of (a) FTO substrate, (b) FTO/WO$_x$ film and (c) FTO/WO$_x$/C$_{60}$ film.

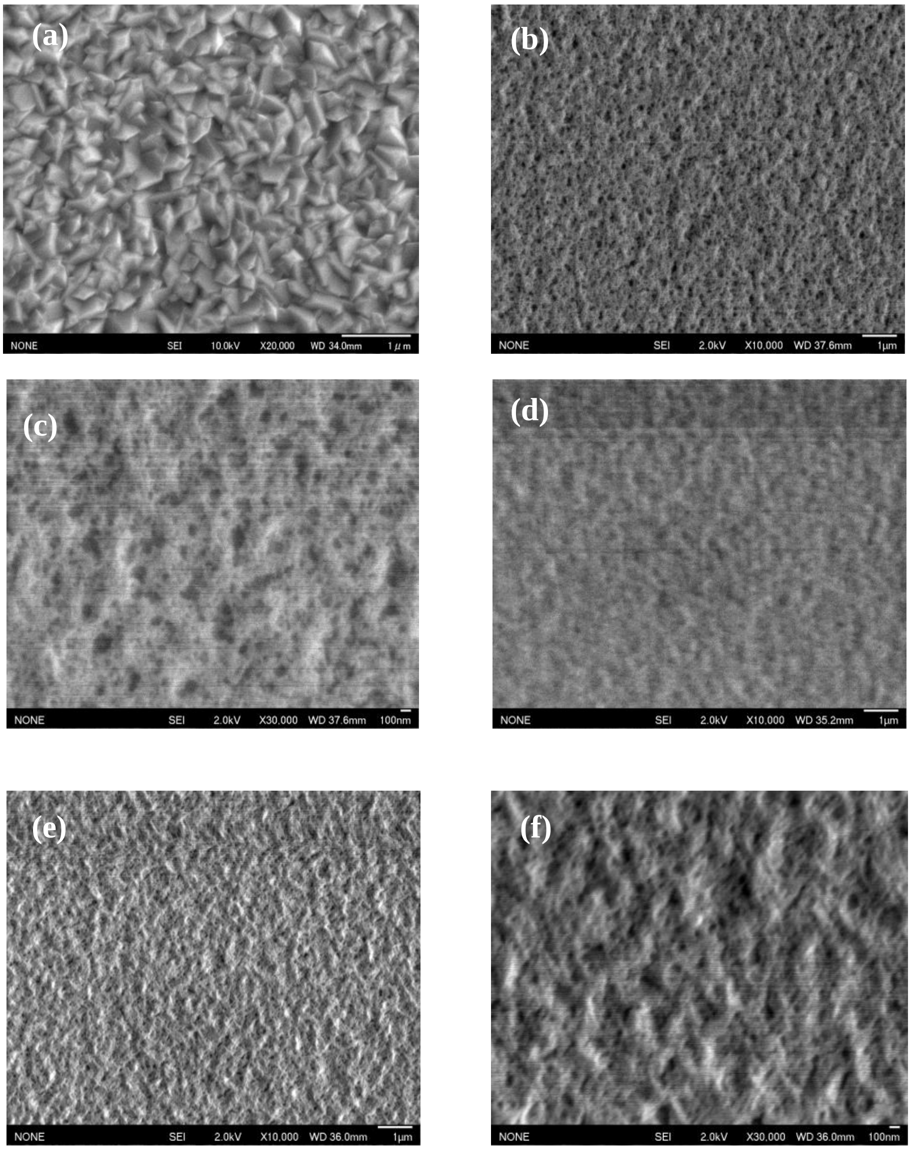

Fig. 5.4 Top view SEM images of (a) bare FTO substrate; (b) low magnification of WO_x film on FTO substrate; (c) high magnification WO_x film on FTO substrate. (d) WO_x/C_{60} film on FTO substrate. SEM images of; (e) low magnification of WO_3 film deposited on FTO substrate (f) high magnification of WO_3 film deposited on FTO substrate.

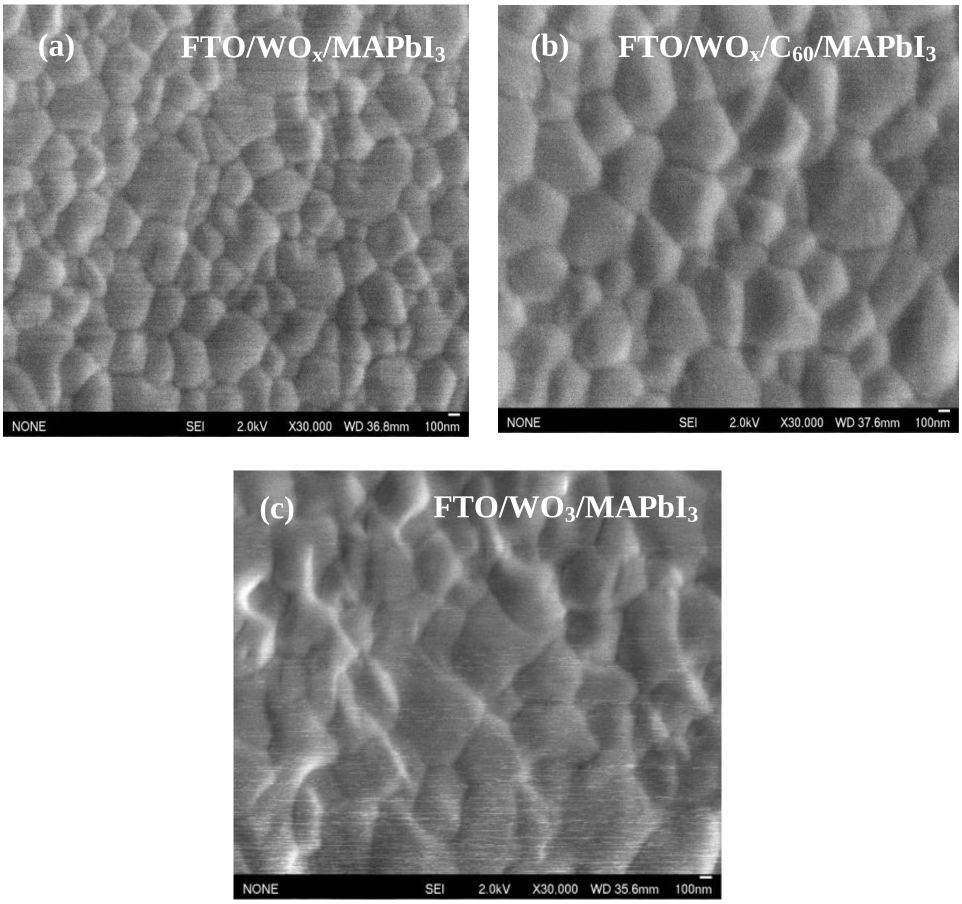

Fig. 5.5 SEM images of (a) FTO/WO$_x$/MAPbI$_3$, (b) FTO/WO$_x$/C$_{60}$/MAPbI$_3$ films, (c) MAPbI$_3$ film on FTO/WO$_3$ substrate

5.2.3 Structural and optical characterization

We further characterized the MAPbI$_3$ perovskite films deposited on FTO/WO$_x$ and FTO/WO$_x$/C$_{60}$ using XRD patterns and UV–vis absorption spectroscopy. The XRD patterns of MAPbI$_3$ perovskite films fabricated on FTO/WO$_x$ and FTO/WO$_x$/C$_{60}$ substrates are almost similar, revealing good crystallinity (Fig. 5.6a). The diffraction peaks located at 2θ values of 14.75, 28.41 and 31.86° can be assigned to (110), (220), and (310) planes of the tetragonal MAPbI$_3$ phase, respectively.

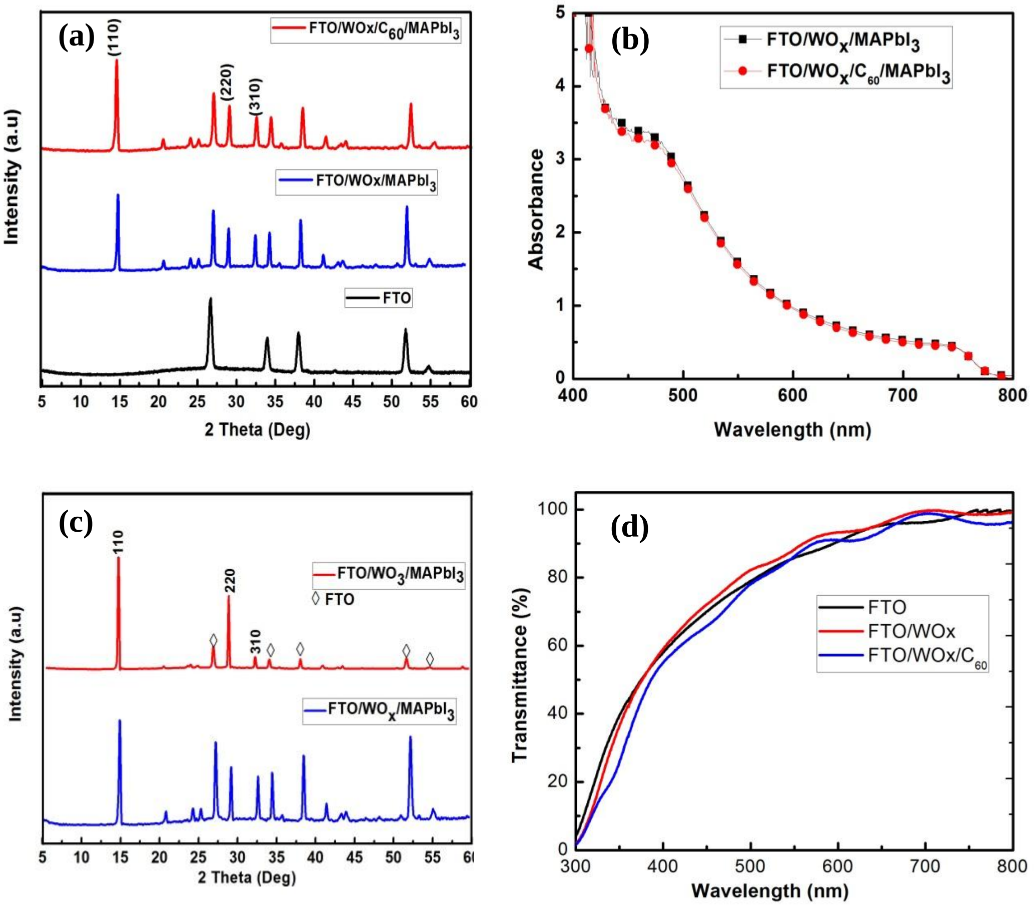

Fig. 5.6 (a) XRD patterns of FTO and perovskite films grown on WO_x and WO_x/C_{60} layers. (b) UV-vis absorbance spectra of PSCs films grown on WO_x and WO_x/C_{60} layers. (c) XRD patterns of $MAPbI_3$ films on FTO/WO_3 and FTO/WO_x substrates. (d) Transmission spectra of FTO substrate, FTO/WO_x, and FTO/WO_x/C_{60} (27 nm) films.

It is noteworthy that such similarity on the XRD patterns of the $MAPbI_3$ perovskite films reveals that C_{60} incorporation does not significantly affect the crystallinity of $MAPbI_3$ film [47, 52]. Fig. 5.6b shows the UV–vis absorption spectra of $MAPbI_3$ perovskite prepared on FTO/WO_x and FTO/WO_x/C_{60} substrates. The absorption onset of the perovskite film is about 790 nm, corresponding to an optical band gap of 1.57 eV [50]. It can be seen that the perovskite films deposited on WO_x and WO_x/C_{60} layers exhibited approximately similar absorbance spectra, suggesting that the light absorption of the remaining C_{60} layer after partial dissolution by the perovskite precursor solvents is negligible compared to the pristine perovskite film [35]. In addition, the similar optical absorption spectra further confirm that both films have similar perovskite composition and thickness.

5.2.4 Photovoltaic performance characterization

Fig. 5.7 shows the *J*-*V* curves of the PSCs with different WO_x EELs thicknesses measured both under forward (from short circuit to open circuit) and reverse scan (from open circuit to short circuit). The photovoltaic (PV) parameters of the cells using different WO_x thicknesses are summarized in Table 1.We found that the device performance increases when the thickness is increased from 30 to 50 nm and decreases as the WO_x thickness is further increased. It can also be seen that the optimum thickness for the WO_x is approximately 50 nm, which we employed in the rest of our investigation.

Table 1. Summary of the PV parameters of best-performing PSCs with varying thicknesses of WO_x measured under forward and reverse voltage scanning.

Devices/scan direction	Thickness (nm)	J_{sc} (mA/cm^2)	V_{oc} (V)	FF	PCE (%)
WOx Forward	30	23.16	0.69	0.41	6.55
WOx Reverse		23.13	0.77	0.57	10.15
WOx Forward	50	22.92	0.73	0.57	9.54
WOx Reverse		22.93	0.84	0.68	13.10
WO_x Forward	80	20.27	0.75	0.62	9.43
WO_x Reverse		20.28	0.82	0.68	11.31
WO_x Forward	100	17.90	0.73	0.61	7.97
WOx Reverse		17.93	0.80	0.67	9.61

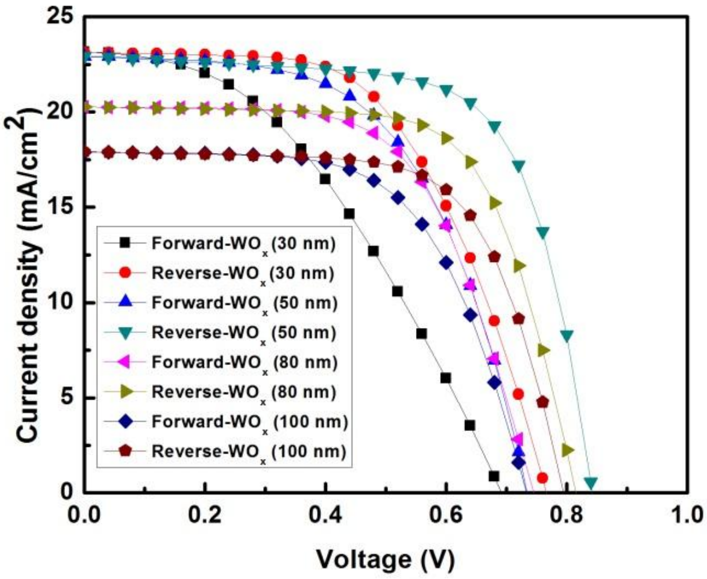

Fig. 5.7 *J–V* curves of PSCs based on WO$_x$ EELs with varying thickness

In order to investigate the effect of incorporating C$_{60}$ interlayer on the device performance, we fabricated planar PSCs with the FTO/WO$_x$/MAPbI$_3$/Spiro-OMeTAD/Au and FTO/WO$_x$/C$_{60}$/MAPbI$_3$/Spiro-OMeTAD/Au architectures. We first studied the influence of the C$_{60}$ layer thickness on the PV performance. PSCs with WO$_x$ EEL coated with different C$_{60}$ thicknesses were fabricated. Fig. 5.8a shows the device performance optimized as a function of C$_{60}$ thickness. The *J–V* parameters are summarized in Table 2. The PCE is increased from 13.68% to 16.07% (under the reverse scan) when the thickness is increased from 20 to 27 nm. The PCE drops to 14.70% when the C$_{60}$ thickness is further increased to 36 nm. Our results suggest that the optimum C$_{60}$ thickness can be achieved at a thickness of 27 nm.

The *J–V* curves of the PSCs based on WO$_3$, WO$_x$ and WO$_x$/C$_{60}$ measured under AM 1.5G irradiation (100 mW/cm^2) is presented in Fig. 5.8b. The PV parameters and average PCEs together with the standard deviations of measurement of 12 cells are summarized in Table 3.

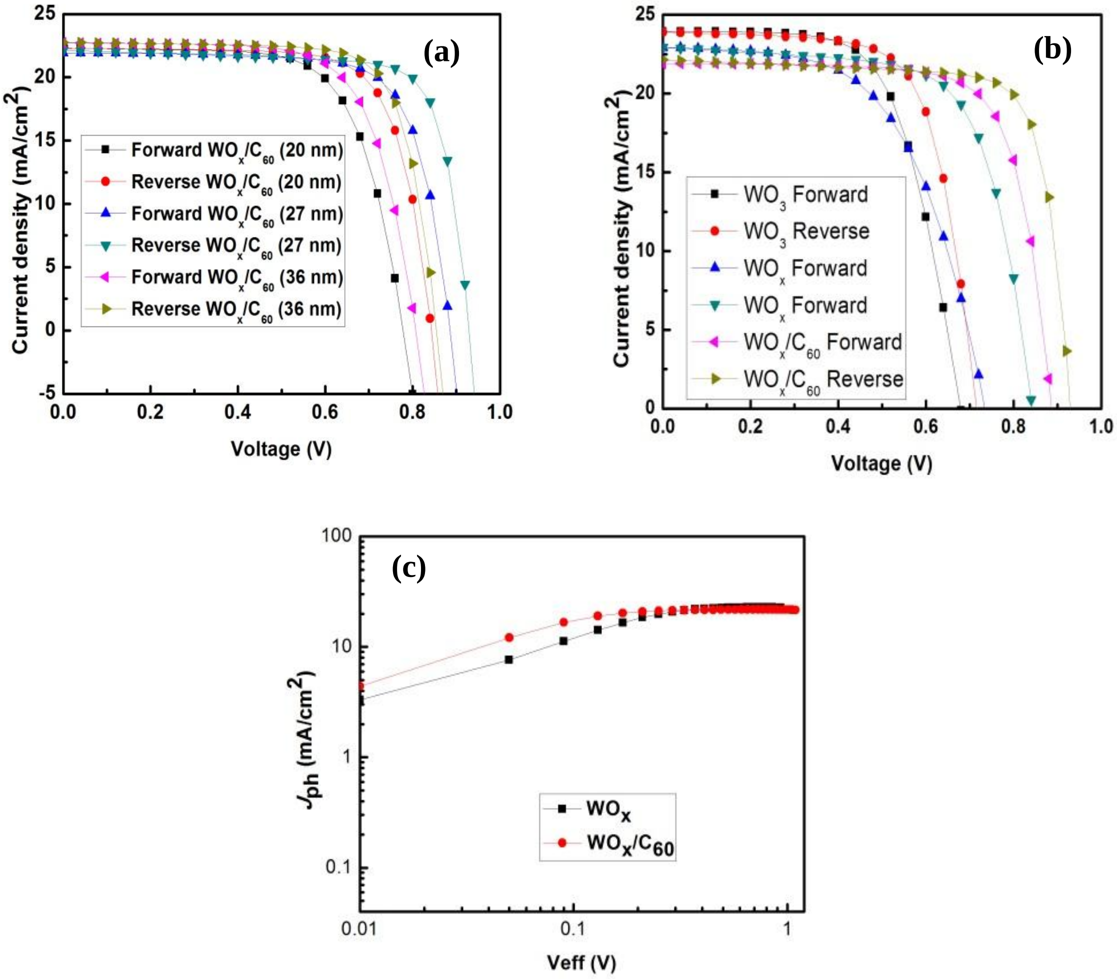

Fig. 5.8 (a) *J*–*V* curves of PSCs based on WO$_x$/C$_{60}$ EELs with varying C$_{60}$ films thickness. (b) *J*–*V* curves of PSCs based on WO$_3$, WO$_x$ and WO$_x$/C$_{60}$ EELs measured under forward and reverse voltage scanning. (c) Plots of J_{ph}– V_{eff} for with and without the C$_{60}$ layer.

Table 2. Summary of the PV parameters of WO_x/C_{60} based PSCs with C_{60} films prepared by different thicknesses measured under forward and reverse voltage scanning.

C_{60} Concentration (mg/mL)	Thickness (nm)	Scan direction	J_{sc} (mA/cm^2)	V_{oc} (V)	FF	PCE (%)
10	20	Forward	22.28	0.78	0.68	11.82
		Reverse	22.31	0.84	0.73	13.68
15	27	Forward	21.91	0.87	0.74	14.11
		Reverse	22.15	0.93	0.78	16.07
20	36	Forward	22.73	0.81	0.70	12.89
		Reverse	22.75	0.85	0.76	14.70

The WO_3 cell achieved a PCE of 10.42%, a V_{oc} of 0.68 V, a J_{sc} of 23.94 mA/cm^2, and a FF of 0.64 when measured in a forward voltage scanning direction. Under reverse voltage scanning, the WO_3 cell achieved a PCE of 11.88%, a V_{oc} of 0.72 V, a J_{sc} of 23.91 mA/cm^2, and a FF of 0.69. The solar cell with pristine WO_x EEL exhibited PCE of 9.54%, a V_{oc} of 0.73 V, a J_{sc} of 22.92 mA/cm^2 and a FF of 0.57 when measured under forward voltage scanning. When measured in the reverse voltage scanning, the solar cell achieved a PCE of 13.10%, a V_{oc} of 0.84 V, a J_{sc} of 22.93 mA/cm^2 and a FF of 0.68. The performances of our WO_x based device are comparable to those previously reported [29]. As it can be seen the WO_3 based device showed a higher J_{sc} and FF together with a lower V_{oc} in contrast to that of WO_x device. We studied the SEM images of FTO/WO_3 and FTO/WO_3/$MAPbI_3$ films. As it can be observed, the WO_3 film deposited on FTO exhibited a crystalline and compact morphology with several grooves (Fig. 5.4e and f). The $MAPbI_3$ perovskite deposited on the FTO/WO_3 exhibited a dense, uniform and compact morphology with grain size comparable to that of FTO/WO_x/$MAPbI_3$ film (see Figs. 5.5a and c).

We further studied the XRD patterns of $MAPbI_3$ deposited on both FTO/WO_x and FTO/WO_3 since the performance of PSCs can be correlated to its crystallinity. Fig. 5.6c shows the XRD patterns of both FTO/WOx/$MAPbI_3$ and FTO/WO_3/$MAPbI_3$ films. The XRD peak of the $MAPbI_3$ deposited on WO_3 at $2\theta = 14.75°$ is stronger, sharper and with a narrower full-width-at-half-maximum (FWHM), suggesting better crystallinity.

This result further suggested that crystalline WO_3 substrate can favor the efficient nucleation and crystallization of perovskite grains. Therefore, we suggest that the higher J_{sc} and FF achieved by the WO_3 device may stem from the high-quality perovskite film with enhanced crystallinity.

Table 3. Summary of the PV parameters of the best-performing PSCs based on WO_3, WO_x and WOx/C_{60} PSCs, and average PCEs together with the standard deviations of 12 cells measured under forward and reverse voltage scanning.

Devices/scan direction	J_{sc} (mA/cm^2)	V_{oc} (V)	FF	Rs (Ω.cm^2)	Rsh (KΩ.cm^2)	PCE (%)	Aver. PCE (± std.dev.)(%)
WO_3 Forward	23.94	0.68	0.64			10.42	10.69±0.86
WO_3 Reverse	23.91	0.72	0.69			11.88	10.71±0.87
WO_x Forward	22.92	0.73	0.57	3.18	1.36	9.540	9.940±1.78
WO_x Reverse	22.93	0.84	0.68	2.47	0.644	13.10	10.11±1.77
WO_x/C_{60} Forward	21.91	0.87	0.74	1.48	4.88	14.11	14.71±0.80
WO_x/C_{60} Reverse	22.15	0.93	0.78	1.35	0.912	16.07	14.79±0.80

Zhang et al. demonstrated that oxygen vacancy in WO_x is critical to the interface energetics for charge injection and transport in organic electronic devices. In their work, it was found that increasing thermal annealing temperature can control the degree of oxygen vacancies in WO_x. The increase in oxygen vacancies induced by thermal annealing led to the partial reduction of W cations, a decrease in the work function of WO_x and increase of charge injection barrier at the WO_x/organic interfaces [51, 52]. Based on their findings, the lower V_{oc} obtained by WO_3-based PSCs could be attributed to the higher energy offsets between the CBM of WO_3 and perovskite [53, 54]. To comparatively and systematically study the impact of using WO_3 and WO_x as EELs on PSCs, a more detailed investigation is required, such as further studying the electrical and optical properties of both WO_3 and WO_x and their effects on the PV parameters of PSCs.

Furthermore, the solar cell containing WO_x/C_{60} showed significant improvement in contrast to that of the WO_x based solar cell. The WO_x/C_{60} solar cell achieved a PCE of 14.11%, a $V_{oc}$of 0.87 V, a J_{sc} of 21.91 mA/cm^2, a FF of 0.74 under forward voltage scanning. In the reverse voltage scanning, the solar cell exhibited a PCE of 16.07%, a V_{oc} of 0.93 V, J_{sc} of 22.15 mA/cm^2, and FF of 0.78. We observed that the V_{oc} and FF values were markedly enhanced compared to those of the WO_x based device and the values reported here are comparable to previously reported values [55]. The J_{sc} values of WO_x/C_{60} solar cell were slightly lower than that of the pristine WO_x device, which may be due to the light loss caused by the absorption of C_{60} layer in the wavelength ranges of 300-550 nm [35, 40, 56, 57], revealed by the transmittance spectra (Fig. 5.6d). Notably, structural and optical characterization showed that the incorporation of C_{60} interlayer did not induce significant changes in the grain size, thickness, and crystallinity of the perovskite film [35]. As shown in Fig.5.2(c), it is well known that the V_{oc} of the PSCs is determined by the energy level offset between the quasi-Fermi levels of the EEL and the HEL adjacent to the perovskite absorber [58]. Therefore, such enhancement in the device performance can be attributed to the more favorable energy-level alignment between the CBM of WO_x/C_{60} and $MAPbI_3$ perovskite absorber and better efficient electron extraction and transport process.

The effect of C_{60} on the work function of WO_x was investigated by Kelvin probe vibrating capacitor method [59]. The C_{60} layer with varying thicknesses was successfully deposited on the WO_x layer by vacuum evaporation in a glove box. The surface potentials and work functions of FTO, FTO/WO_x, and FTO/WO_x/C_{60} are summarized in Table 4.

Table 4. Surface potentials and Work function of FTO, FTO/WO_x, and FTO/WOx/C_{60}

Sample	Surface potential (V)	Work function (eV)
FTO	-0.10 ± 0.036	4.80
FTO/WO_x	-0.12 ± 0.024	4.78
FTO/WO_x/C_{60} (5 nm)	-0.340 ± 0.017	4.56
FTO/WO_x/C_{60} (10 nm)	-0.320 ± 0.004	4.58
FTO/WO_x/C_{60} (20 nm)	-0.295 ± 0.005	4.61
FTO/WO_x/C_{60} (40 nm)	-0.252 ± 0.013	4.65

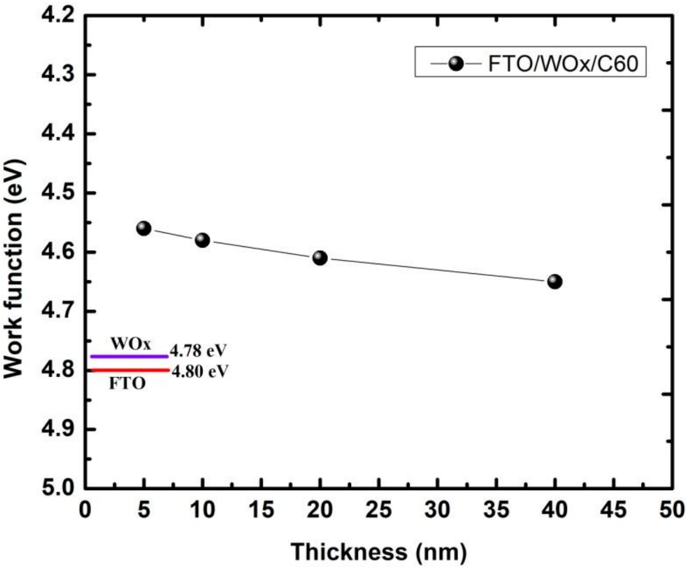

Fig. 5.9 Work function of WO_x/C_{60} with varying C_{60} thicknesses. The inset shows the work function of bare FTO and FTO/WO_x

Fig. 5.9 shows the work function WO_x/C_{60} with varying C_{60} thicknesses. It was found that the work function of WO_x coated on FTO decreased from 4.78 eV to 4.56 eV for WO_x/C_{60} (5 nm). Upon further increasing the C_{60} thickness (40 nm), the work function of WO_x/C_{60} was found to increase to about 4.65 eV, which is still lower than the work function of WO_x coated on FTO. The decrease in work function exhibited by WO_x/C_{60} may be due to the interfacial dipole change induced by C_{60}. The dipole is expected to lower the work function of WO_x through a downward vacuum energy level shift [60]. The decreased work function of WO_x with the deposited C_{60} layer would improve the energy level alignment between the WO_x and perovskite, leading to more effective electron extraction and transport. This effect is expected to contribute to the increase in the V_{oc} and FF of WO_x/C_{60} based solar cell [60].

We further investigated the effect of C_{60} on the performance of the devices, in particular on the enhancement of the FF, photocurrent density (J_{ph}) – effective voltage (V_{eff}) plots were estimated according to previous reports [50,61-65]. Fig. 5.8c shows the J_{ph}–V_{eff} plots of devices with WO_x and WO_x/C_{60} EELs in double-logarithmic coordinates. J_{ph} is determined by equation (3).

$$J_{ph} = J_L - J_D \tag{3}$$

Where J_L is the current densities under illumination and J_D is the current densities in the dark. V_{eff} is estimated from equation (4).

$$V_{eff} = V_0 - V \tag{4}$$

Where V is the applied voltage and V_0 is the voltage at which J_{ph} =0.

The J_{ph} of both devices exhibits a similar trend, first increasing linearly with V_{eff} and reaching a saturated level at >0.5 V (Fig. 5.8c). Notably, the PSCs with WO_x/C_{60} EEL showed higher J_{ph} at small V_{eff} compared to that of WO_x based solar cell, suggesting a higher charge extraction efficiency and consequently, a higher FF [62,63]. Furthermore, the R_{sh} and R_s values extracted from the slope of J–V curve (Fig. 5.8b) at near J_{sc} and V_{oc} points, respectively, for both devices are listed in Table 3. The WO_x/C_{60} based device showed lower R_s values than those of the WO_x based device, suggesting that the WO_x/C_{60} formed better electrical contact with the perovskite absorber layer. Also, the WO_x/C_{60} device exhibited a much larger R_{sh}, suggesting that the WO_x/C_{60} EEL can provide better hole blocking capability, and consequently lead to a higher V_{oc} [10].

Fig. 5.10a shows the IPCE spectra of the solar cells incorporating pristine WO_x and WO_x/C_{60} EELs. It is worth mentioning that high-quality $MAPbI_3$ perovskite deposited on the both WO_x and WOx/C_{60} EELs play a critical role in both solar light absorption and photocarrier generation in the solar cells. As can be seen in Fig. 5.10a, both devices exhibit a broad response with IPCE values higher than 80% in the region of 400-600 nm, indicating that the devices absorbed solar spectrum efficiently over a wide range. The slightly higher IPCE value exhibited by WO_x/C_{60} device could be attributed to the improved electron extraction and transport [66]. The Integrated photocurrent densities calculated from the IPCE curves are 20.72 and 20.98 mA/cm^2 for WO_x and WO_x/C_{60} based devices, respectively, which are comparable to the J_{sc} values determined from the *J*–*V* curves in Fig. 5.8b. To study the reproducibility of our devices, the box plots of photovoltaic parameters of 12 cells based on WO_x and WO_x/C_{60} are shown in Fig. 5.11. Both devices exhibited less scattering of the *J*–*V* parameters with smaller variability for the WO_x/C_{60} based solar cell, suggesting good reproducibility.

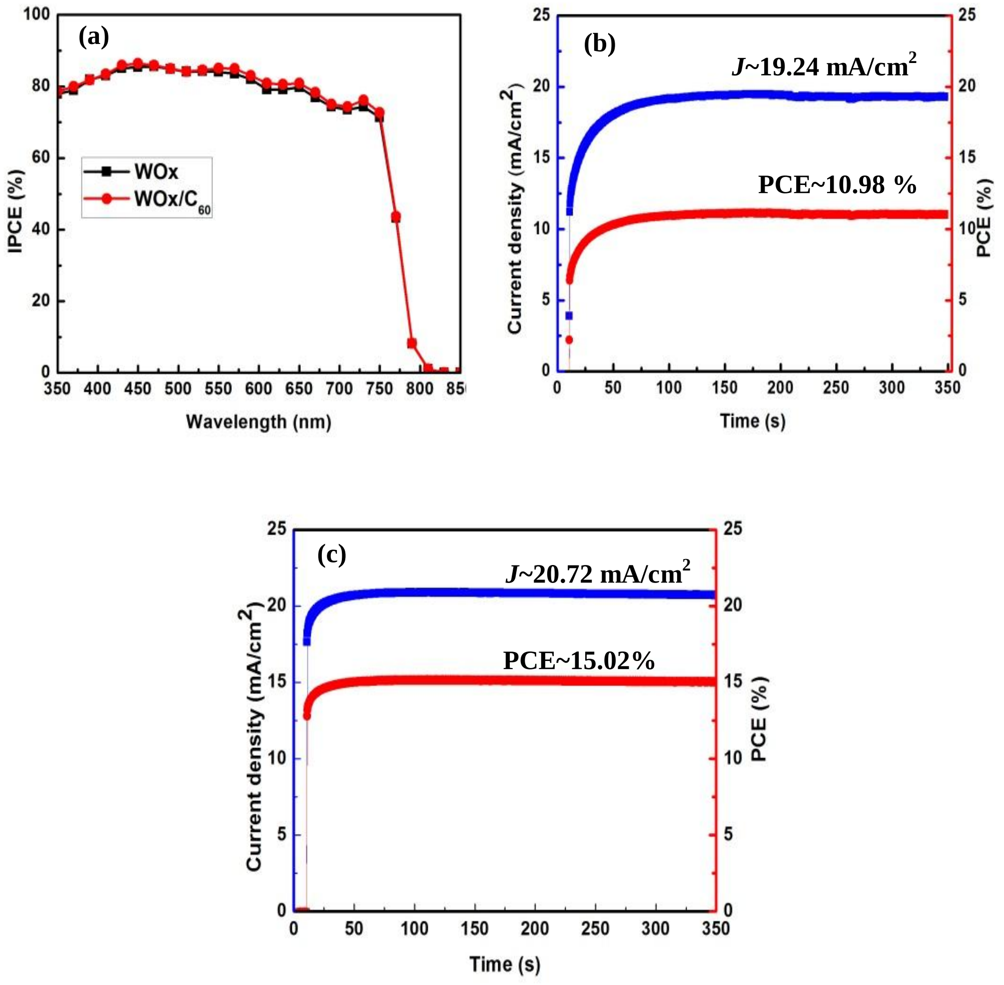

Fig. 5.10 (a) IPCE spectra of WO_x and WO_x/C_{60} based devices. Steady-state efficiency and photocurrent as a function of time of the best-performing devices with; (b) WO_x, and (c) WO_x/C_{60} EELs measured at the maximum power point.

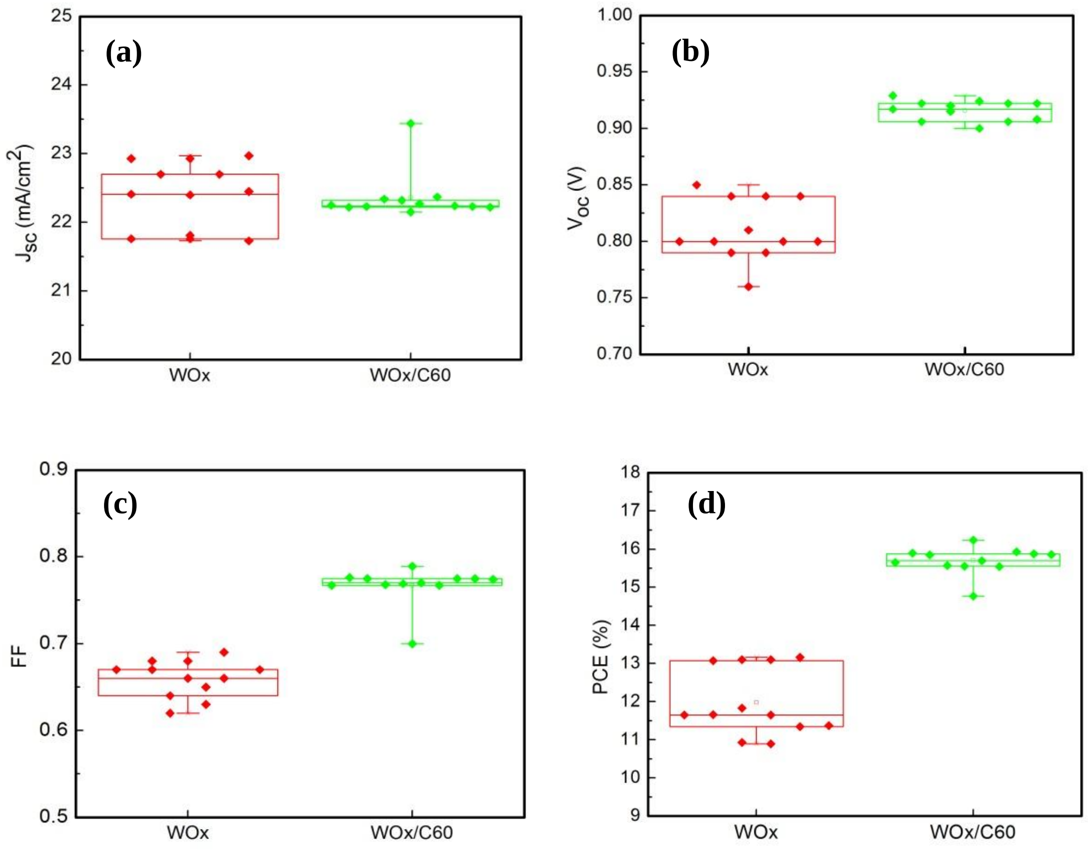

Fig. 5.11 Box plots of; (a) $J_{sc,}$ (b) $V_{oc,}$ (c) FF and (d) PCE for 12 cells based on WO_x and WO_x/C_{60} EELs measured under reverse voltage scanning.

Anomalous hysteresis of *J–V* characteristic is one of the most critical issues in PSCs. Typically the origin of hysteresis can be from the charge selective layers, trapping and detrapping of charge carriers, ionic movement or ferroelectric properties of the perovskite materials [67-71]. The WO_x and WO_x/C_{60} devices showed hysteretic *J–V* behavior (Fig. 5.8b). However, the hysteresis in WO_x device is more pronounced compared to the WO_x/C_{60} device. The less hysteresis exhibited by the WO_x/C_{60} based PSC can be attributed to the passivation of the grain boundaries and suppression of ion migration within the perovskite by the partially dissolved C_{60}, which infiltrated into the perovskite [35,41,43]. Also, the C_{60} may suppress the accumulated charge carriers, capacitance effect and trap-state density at the WO_x/perovskite interface, resulting in enhanced electron extraction efficiency and reduced hysteresis [72,73]. Figs. 5.10b and c show the steady-state photocurrent densities and efficiencies as a function of time of the best-performing devices measured maximum power point with a constant bias voltage of 0.80V (under 100 mW/cm^2 illumination). The WO_x based device delivered a photocurrent and PCE of about 19.24 mA/cm^2 and 10.98% respectively. Interestingly, the WO_x/C_{60} based device delivered a higher photocurrent of 20.72 mA/cm^2 and PCE of 15.02%, which are relatively close to the values obtained from the *J–V* measurement under reverse voltage scanning. Furthermore, upon illumination, the steady-state efficiency and photocurrent of WO_x/C_{60} based device showed a faster rise to the maximum value compared to the WO_x device, suggesting improved electron extraction/transport and reduce interface recombination in the device [35, 46].

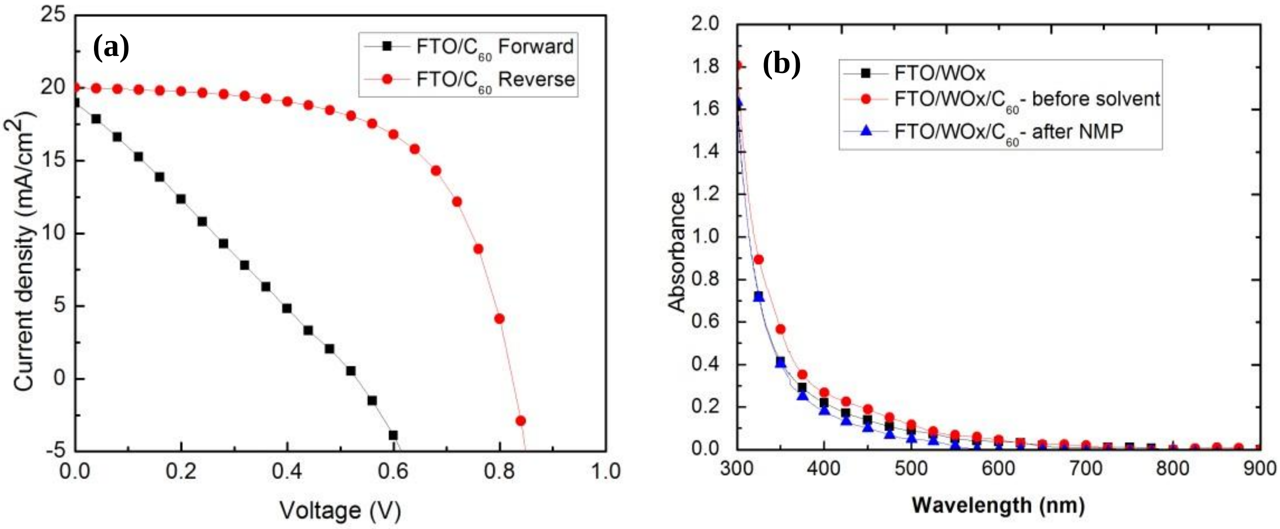

Fig. 5.12 (a) *J–V* curves of PSCs with C_{60} only EEL. (b) UV-vis absorbance spectra of FTO/WO_x, FTO/WO_x/C_{60} (27 nm) (before spin-coating NMP solvent), and FTO/WO_x/C_{60} films (after spin-coating NMP solvent).

We fabricated PSCs incorporating only C_{60} EEL to elucidate the synergic effect of WO_x and C_{60} in enhancing the performance of the device. Fig. 5.12a shows the *J–V* characteristics of the best-performing device with C_{60} only EEL. The device exhibited a J_{sc} of 19.00 mA/cm^2, V_{oc} of 0.53 V, FF of 0.26 and PCE of 2.62% under forward voltage scanning. When measured by reverse voltage scanning, the J_{sc}, V_{oc}, FF, and PCE increased to 20.02 mA/cm^2, 0.82 V, 0.62 and 10.18%, respectively. Notably, the PSCs incorporating only C_{60} EEL showed larger hysteretic behavior and lower performance compared to the best-performing WO_x-based device. It is worth mentioning that the *J–V* result of our C_{60} only device is lower than previously reported values [38]. We conducted a simple experiment to confirm the robustness of C_{60} when treated with the perovskite precursor solvent. Fig. 5.12b presents the UV-vis absorption spectra of FTO/WO_x, and FTO/WO_x/C_{60} films (with and without NMP treatment). The absorption of FTO/WO_x/C_{60} film decreases when treated with NMP solvent. Wojciechowski *et al.* reported that C_{60} only could be used as an efficient compact EEL in PSCs. In their work, it was found that C_{60} is poorly soluble in most polar aprotic solvents such as *N*, *N*-dimethylformamide (DMF), but the exposure to the solvent during spin-coating might be enough to cause partial dissolution of the C_{60} film and deteriorate the hole-blocking properties of the EEL layer [38]. Therefore, we hypothesized that the C_{60}-only device suffered from severe charge carrier recombination due to the partial dissolution of the C_{60} film by the precursor solvent (NMP), leaving a very thin layer of C_{60} on the FTO substrate [38, 40].

Recently, it was found that fullerenes can be re-dissolved when the perovskite is deposited using solution process, allowing ultra-thin fullerenes to be retained at the interface and some dissolved fullerenes infiltrate into the perovskite grain boundaries [35,40]. Therefore, based on previous reports, we conclude that the performance enhancement induced by the use of WO_x/C_{60} could be due the improvement of the EEL/perovskite interfacial properties, such as better electron extraction/transport and less charge recombination.

5.2.5 Photoluminescence analysis

To further gain insight into the improved performance of WO_x/C_{60}-based PSCs, the steady-state PL was measured for the $MAPbI_3$ perovskite absorber layer deposited on FTO, FTO/WO_x, and FTO/WO_x/C_{60} (Fig. 5.13). The PL spectra of the perovskite films show emission peak at around 770 nm. Upon the incorporation of the C_{60} interlayer, significant quenching of the perovskite is exhibited, indicating enhanced electron extraction and transportation from the perovskite to C_{60}. Therefore, the PL studies further confirm that the incorporation of the C_{60} layer could facilitate efficient charge transfer between the perovskite and WO_x layer, thereby improving the device performance [62].

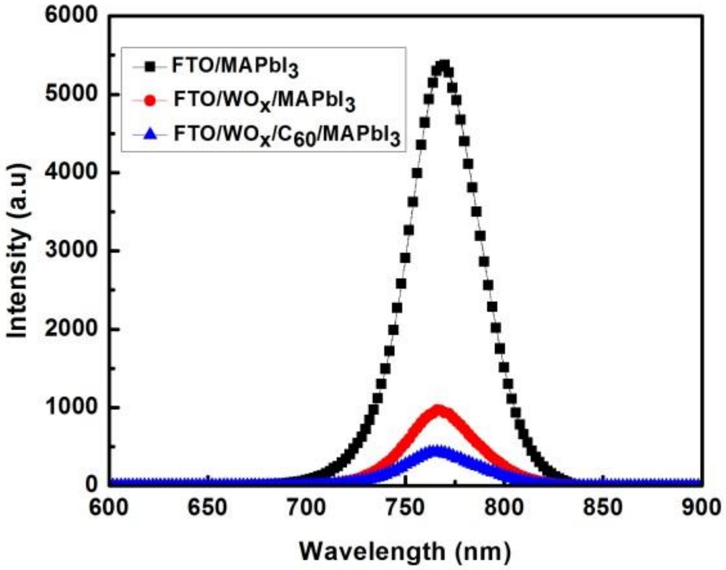

Fig. 5.13 PL spectra of perovskite films deposited on FTO, WO_x, and WO_x/C_{60} films.

5. 3 Conclusion

In summary, we have demonstrated that the use WOx/C60 EELs can significantly enhance the performance of PSCs. The best-performing PSCs using WO_x/C_{60} EEL achieved a PCE of 16.07% when measured under reverse voltage scanning. The *J–V* characterization and steady-state PL results suggest that the significantly improved efficiency by the WO_x/C_{60}-based device originates from improved electron extraction, transportation and as well reduced charge recombination at the WO_x/C_{60} and perovskite interface. Our results demonstrate a simple approach for further enhancing the efficiency of WO_x-based PSCs.

5.4 References

[1] X. Liu, H. Yu, L. Yan, Q. Dong, Q. Wan, Y. Zhou, B. Song, Y. Li, Triple cathode buffer layers composed of PCBM, C60, and LiF for high-performance planar perovskite solar cells, ACS Appl.Mater.&Interfaces, 7 (2015) 6230-6237.

[2] H. Zhou, Q. Chen, G. Li, S. Luo, T.-b. Song, H.-S. Duan, Z. Hong, J. You, Y. Liu, Y. Yang, Interface engineering of highly efficient perovskite solar cells, Science, 345 (2014) 542-546.

[3] J. Burschka, N. Pellet, S.-J. Moon, R. Humphry-Baker, P. Gao, M.K. Nazeeruddin, M. Grätzel, Sequential deposition as a route to high-performance perovskite-sensitized solar cells, Nature, 499 (2013) 316-319.

[4] G.E. Eperon, V.M. Burlakov, P. Docampo, A. Goriely, H.J. Snaith, Morphological control for high performance, solution-processed planar heterojunction perovskite solar cells, Adv. Funct. Mater., 24 (2014) 151-157.

[5] Y. Cheng, Q.-D. Yang, J. Xiao, Q. Xue, H.-W. Li, Z. Guan, H.-L. Yip, S.-W. Tsang, Decomposition of organometal halide perovskite films on zinc oxide nanoparticles, ACS Appl.Mater.&Interfaces, 7 (2015) 19986-19993.

[6] D. Liu, T.L. Kelly, Perovskite solar cells with a planar heterojunction structure prepared using room-temperature solution processing techniques, Nat.Photon., 8 (2014) 133-138.

[7] W. Ke, G. Fang, Q. Liu, L. Xiong, P. Qin, H. Tao, J. Wang, H. Lei, B. Li, J. Wan, Low-temperature solution-processed tin oxide as an alternative electron transporting

layer for efficient perovskite solar cells, J. Am. Chem. Soc., 137 (2015) 6730-6733.

[8] M. Qin, J. Ma, W. Ke, P. Qin, H. Lei, H. Tao, X. Zheng, L. Xiong, Q. Liu, Z. Chen, Perovskite solar cells based on low-temperature processed indium oxide electron selective layers, ACS Appl.Mater.&Interfaces, 8 (2016) 8460-8466.

[9] H.-S. Kim, C.-R. Lee, J.-H. Im, K.-B. Lee, T. Moehl, A. Marchioro, S.-J. Moon, R. Humphry-Baker, J.-H. Yum, J.E. Moser, Lead iodide perovskite sensitized all-solid-state submicron thin film mesoscopic solar cell with efficiency exceeding 9%, Sci.Rep., 2 (2012) 591.

[10] Z. Liu, Q. Chen, Z. Hong, H. Zhou, X. Xu, N. De Marco, P. Sun, Z. Zhao, Y.-B. Cheng, Y. Yang, Low-Temperature TiO x Compact Layer for Planar Heterojunction Perovskite Solar Cells, ACS Appl.Mater.&Interfaces, 8 (2016) 11076-11083.

[11] K. Wojciechowski, M. Saliba, T. Leijtens, A. Abate, H.J. Snaith, Sub-150 C processed meso-superstructured perovskite solar cells with enhanced efficiency, Energy Environ. Sci., 7 (2014) 1142-1147.

[12] A. Yella, L.-P. Heiniger, P. Gao, M.K. Nazeeruddin, M. Grätzel, Nanocrystalline rutile electron extraction layer enables low-temperature solution processed perovskite photovoltaics with 13.7% efficiency, Nano Lett., 14 (2014) 2591-2596.

[13] C. Tao, S. Neutzner, L. Colella, S. Marras et al., 17.6% stabilized efficiency in low-temperature processed planar perovskite solar cells, Energy Environ, 8 (2015) 2365-2370.

[14] J.M. Berak, M. Sienko, Effect of oxygen-deficiency on electrical transport properties of tungsten trioxide crystals, J. Solid State Chem., 2 (1970) 109-133.

[15] M. Gillet, K. Aguir, C. Lemire, E. Gillet, K. Schierbaum, The structure and electrical conductivity of vacuum-annealed WO 3 thin films, Thin Solid Films, 467 (2004) 239-246.

[16] S.-M. Yong, T. Nikolay, B.T. Ahn, D.K. Kim, One-dimensional WO 3 nanorods as photoelectrodes for dye-sensitized solar cells, J. Alloys Compd., 547 (2013) 113-117.

[17] H. Zheng, Y. Tachibana, K. Kalantar-zadeh, Dye-sensitized solar cells based on WO3, Langmuir, 26 (2010) 19148-19152.

[18] S.K. Deb, Opportunities and challenges in science and technology of WO 3 for electrochromic and related applications, Solar Energy Materials and Solar Cells, 92 (2008) 245-258.

[19] H.-S. Shim, J.W. Kim, Y.-E. Sung, W.B. Kim, Electrochromic properties of tungsten oxide nanowires fabricated by electrospinning method, Solar Energy Materials and Solar Cells, 93 (2009) 2062-2068.

[20] X.-L. Li, T.-J. Lou, X.-M. Sun, Y.-D. Li, Highly sensitive WO3 hollow-sphere gas sensors, Inorg. Chem., 43 (2004) 5442-5449.

[21] J. Solis, S. Saukko, L. Kish, C. Granqvist, V. Lantto, Semiconductor gas sensors based on nanostructured tungsten oxide, Thin Solid Films, 391 (2001) 255-260.

[22] F. Wang, C. Di Valentin, G. Pacchioni, Rational band gap engineering of WO3 photocatalyst for visible light water splitting, ChemCatChem, 4 (2012) 476-478.

[23] S.F. Shaikh, S.S. Kalanur, R.S. Mane, O.-S. Joo, Monoclinic WO 3 nanorods–rutile TiO 2 nanoparticles core–shell interface for efficient DSSCs, Dalton Trans., 42 (2013) 10085-10088.

[24] Z.a. Tan, L. Li, C. Cui, Y. Ding, Q. Xu, S. Li, D. Qian, Y. Li, Solution-processed tungsten oxide as an effective anode buffer layer for high-performance polymer solar cells, J. Phys. Chem. C, 116 (2012) 18626-18632.

[25] K. Mahmood, B.S. Swain, A.R. Kirmani, A. Amassian, Highly efficient perovskite solar cells based on a nanostructured WO 3–TiO 2 core–shell electron transporting material, J. Mater. Chem. A, 3 (2015) 9051-9057.

[26] K. Wang, Y. Shi, Q. Dong, Y. Li, S. Wang, X. Yu, M. Wu, T. Ma, Low-temperature and solution-processed amorphous WO X as electron-selective layer for perovskite solar cells, J.Phys.Chem.Lett., 6 (2015) 755-759.

[27] C.-M. Chen, Z.-K. Lin, W.-J. Huang, S.-H. Yang, WO 3 Nanoparticles or Nanorods Incorporating Cs 2 CO 3/PCBM Buffer Bilayer as Carriers Transporting Materials for Perovskite Solar Cells, Nanoscale Res. Lett., 11 (2016) 464.

[28] K. Wang, Y. Shi, B. Li, L. Zhao, W. Wang, X. Wang, X. Bai, S. Wang, C. Hao, T. Ma, Amorphous Inorganic Electron-Selective Layers for Efficient Perovskite Solar Cells: Feasible Strategy Towards Room-Temperature Fabrication, Adv. Mater., 28 (2016) 1891-1897.

[29] K. Wang, Y. Shi, L. Gao, R. Chi, K. Shi, B. Guo, L. Zhao, T. Ma, W (Nb) O x-based efficient flexible perovskite solar cells: From material optimization to working principle, Nano Energy, 31 (2017) 424-431.

[30] G. Li, V. Shrotriya, J. Huang, Y. Yao, T. Moriarty, K. Emery, Y. Yang, High-

efficiency solution processable polymer photovoltaic cells by self-organization of polymer blends, Nat.Mater., 4 (2005) 864-868.

[31] T. Mori, K. Kato, Photovoltaic properties of organic thin-film solar cell using various exciton-diffusion blocking materials, J. Photopolym. Sci. Technol., 20 (2007) 61-66.

[32] T. Mori, N. Naito, Photovoltaic Properties of Polythiophen: Fullerene Derivative Solar Cell Using Annealing due to Anode Joule Heating, J. Photopolym. Sci. Technol., 28 (2015) 393-398.

[33] W. Ke, D. Zhao, C.R. Grice, A.J. Cimaroli, G. Fang, Y. Yan, Efficient fully-vacuum-processed perovskite solar cells using copper phthalocyanine as hole selective layers, J. Mater. Chem. A, 3 (2015) 23888-23894.

[34] W. Ke, D. Zhao, C.R. Grice, A.J. Cimaroli, J. Ge, H. Tao, H. Lei, G. Fang, Y. Yan, Efficient planar perovskite solar cells using room-temperature vacuum-processed C 60 electron selective layers, J. Mater. Chem. A, 3 (2015) 17971-17976.

[35] W. Ke, D. Zhao, C. Xiao, C. Wang, A.J. Cimaroli, C.R. Grice, M. Yang, Z. Li, C.-S. Jiang, M. Al-Jassim, Cooperative tin oxide fullerene electron selective layers for high-performance planar perovskite solar cells, J. Mater. Chem. A, 4 (2016) 14276-14283.

[36] P.W. Liang, C.C. Chueh, S.T. Williams, A.K.Y. Jen, Roles of Fullerene-Based Interlayers in Enhancing the Performance of Organometal Perovskite Thin-Film Solar Cells, Adv. Energy Mater., 5 (2015) 1402321.

[37] S. Ryu, J. Seo, S.S. Shin, Y.C. Kim, N.J. Jeon, J.H. Noh, S.I. Seok, Fabrication of metal-oxide-free CH 3 NH 3 PbI 3 perovskite solar cells processed at low temperature, J. Mater. Chem. A, 3 (2015) 3271-3275.

[38] K. Wojciechowski, T. Leijtens, S. Siprova, C. Schlueter, M.T. Hörantner, J.T.-W. Wang, C.-Z. Li, A.K.-Y. Jen, T.-L. Lee, H.J. Snaith, C60 as an efficient n-type compact layer in perovskite solar cells, J.Phys.Chem.Lett., 6 (2015) 2399-2405.

[39] D. Zhao, M. Sexton, H.Y. Park, G. Baure, J.C. Nino, F. So, High-Efficiency Solution-Processed Planar Perovskite Solar Cells with a Polymer Hole Transport Layer, Adv. Energy Mater., 5 (2014) 1401855.

[40] Z. Zhou, J. Xu, L. Xiao, J. Chen, Z.a. Tan, J. Yao, S. Dai, Efficient planar perovskite solar cells prepared via a low-pressure vapor-assisted solution process with fullerene/TiO 2 as an electron collection bilayer, RSC Adv., 6 (2016) 78585-78594.

[41] Y. Shao, Z. Xiao, C. Bi, Y. Yuan, J. Huang, Origin and elimination of photocurrent hysteresis by fullerene passivation in CH3NH3PbI3 planar heterojunction solar cells, Nat.Commun., 5 (2014) 5784.

[42] Q. Wang, Y. Shao, Q. Dong, Z. Xiao, Y. Yuan, J. Huang, Large fill-factor bilayer iodine perovskite solar cells fabricated by a low-temperature solution-process, Energy Environ. Sci., 7 (2014) 2359-2365.

[43] J. Xu, A. Buin, A.H. Ip, W. Li, O. Voznyy, R. Comin, M. Yuan, S. Jeon, Z. Ning, J.J. McDowell, Perovskite-fullerene hybrid materials suppress hysteresis in planar diodes, Nat.Commun., 6 (2015) 7081.

[44] R. Balzer, V. Drago, W.H. Schreiner, L.F. Probst, Synthesis and structure-activity relationship of a WO3 catalyst for the total oxidation of BTX, J. Braz. Chem. Soc., 25 (2014) 2026-2031.

[45] H. Habazaki, Y. Hayashi, H. Konno, Characterization of electrodeposited WO 3 films and its application to electrochemical wastewater treatment, Electrochim. Acta, 47 (2002) 4181-4188.

[46] Y. Li, Y. Zhao, Q. Chen, Y. Yang, Y. Liu, Z. Hong, Z. Liu, Y.-T. Hsieh, L. Meng, Y. Li, Multifunctional fullerene derivative for interface engineering in perovskite solar cells, J. Am. Chem. Soci., 137 (2015) 15540-15547.

[47] V.O. Eze, T. Mori, Enhanced photovoltaic performance of planar perovskite solar cells fabricated in ambient air by solvent annealing treatment method, Japanese Journal of Applied Physics, 55 (2016) 122301.

[48] K. Nishio, S. Tadanori, T. Tsuchiya, Preparation of electrochromic tungsten oxide thin film by sol-gel process, J. Ceram. Soc. Jpn., 107 (1999) 199-203.

[49] J. Wang, X. Xiang, X. Yao, W.-J. Xiao, J. Lin, W.-S. Li, Efficient perovskite solar cells using trichlorosilanes as perovskite/PCBM interface modifiers, Organic Electronics, 39 (2016) 1-9.

[50] H. Yang, J. Zhang, C. Zhang, J. Chang, Z. Lin, D. Chen, X. Sun, H. Xi, G. Han, Y. Hao, Effect of polyelectrolyte interlayer on efficiency and stability of pin perovskite Solar cells, Solar Energy139 (2016) 190-198.

[51] M. Raja, J. Chandrasekaran, M. Balaji, B. Janarthanan, Impact of annealing treatment on structural and dc electrical properties of spin coated tungsten trioxide thin films for Si/WO 3/Ag junction diode, Materials Science in Semiconductor Processing,

56 (2016) 145-154.

[52] Z. Zhang, H.-X. Wei, G.-F. Ma, Y.-Q. Li, S.-T. Lee, J.-X. Tang, Interface energetics at WOX/organic interfaces: The role of oxygen vacancies, Appl. Phys. Lett., 103 (2013) 176_171.

[53] A. Gheno, T.T.T. Pham, C. Di Bin, J. Bouclé, B. Ratier, S. Vedraine, Printable WO 3 electron transporting layer for perovskite solar cells: Influence on device performance and stability, Solar Energy Materials and Solar Cells, 161 (2017) 347-354.

[54] J. Zhang, C. Shi, J. Chen, Y. Wang, M. Li, Preparation of ultra-thin and high-quality WO 3 compact layers and comparision of WO 3 and TiO 2 compact layer thickness in planar perovskite solar cells, J. Solid State Chem., 238 (2016) 223-228.

[55] Y. Hou, C.O.R. Quiroz, S. Scheiner, W. Chen, T. Stubhan, A. Hirsch, M. Halik, C.J. Brabec, Low-Temperature and Hysteresis-Free Electron-Transporting Layers for Efficient, Regular, and Planar Structure Perovskite Solar Cells, Adv. Energy Mater., 5 (2015) 1501056.

[56] D. Zhao, W. Ke, C.R. Grice, A.J. Cimaroli, X. Tan, M. Yang, R.W. Collins, H. Zhang, K. Zhu, Y. Yan, Annealing-free efficient vacuum-deposited planar perovskite solar cells with evaporated fullerenes as electron-selective layers, Nano Energy, 19 (2016) 88-97.

[57] H. Yoon, S.M. Kang, J.-K. Lee, M. Choi, Hysteresis-free low-temperature-processed planar perovskite solar cells with 19.1% efficiency, EnergyEnviron. Sci., 9 (2016) 2262-2266.

[58] J. Kim, G. Kim, T.K. Kim, S. Kwon, H. Back, J. Lee, S.H. Lee, H. Kang, K. Lee, Efficient planar-heterojunction perovskite solar cells achieved via interfacial modification of a sol–gel ZnO electron collection layer, J. Mater. Chem. A, 2 (2014) 17291-17296.

[59] N. Ishiyama, M. Kubo, T. Kaji, M. Hiramoto, Doping-based control of the energetic structure of photovoltaic co-deposited films, Appl. Phys. Lett. 99 (2011), 133301

[60] L. Zuo, Z. Gu, T. Ye, W. Fu, G. Wu, H. Li, H. Chen Enhanced Photovoltaic Performance of CH3NH3PbI3 Perovskite Solar Cells through Engineering Using Self-Assembling Monolayer

[61] H. Azimi, T. Ameri, H. Zhang, Y. Hou, C.O.R. Quiroz, J. Min, M. Hu, Z.G. Zhang,

T. Przybilla, G.J. Matt, A Universal Interface Layer Based on an Amine-Functionalized Fullerene Derivative with Dual Functionality for Efficient Solution Processed Organic and Perovskite Solar Cells, Adv. Energy Mater., 5 (2015) 1401692.

[62] T. Cao, Z. Wang, Y. Xia, B. Song, Y. Zhou, N. Chen, Y. Li, Facilitating Electron Transportation in Perovskite Solar Cells via Water-Soluble Fullerenol Interlayers, ACS Appl. Mater. Interfaces, 8 (2016) 18284-18291.

[63] J.D. Chen, C. Cui, Y.Q. Li, L. Zhou, Q.D. Ou, C. Li, Y. Li, J.X. Tang, Single-junction polymer solar cells exceeding 10% power conversion efficiency, Adv. Mater., 27 (2015) 1035-1041.

[64] A.K.K. Kyaw, D.H. Wang, D. Wynands, J. Zhang, T.-Q. Nguyen, G.C. Bazan, A.J. Heeger, Improved light harvesting and improved efficiency by insertion of an optical spacer (ZnO) in solution-processed small-molecule solar cells, Nano Lett., 13 (2013) 3796-3801.

[65] Z. Li, X. Zhang, C. Liu, Z. Zhang, J. Li, L. Shen, W. Guo, S. Ruan, Enhanced Electron Extraction Capability of Polymer Solar Cells via Employing Electrostatically Self-Assembled Molecule on Cathode Interfacial Layer, ACS Appl.Mater. Interfaces, 8 (2016) 8224-8231.

[66] J.H. Heo, H.J. Han, D. Kim, T.K. Ahn, S.H. Im, Hysteresis-less inverted CH 3 NH 3 PbI 3 planar perovskite hybrid solar cells with 18.1% power conversion efficiency, Energy Environ. Sci., 8 (2015) 1602-1608.

[67] C. Eames, J.M. Frost, P.R. Barnes, B.C. O’regan, A. Walsh, M.S. Islam, Ionic transport in hybrid lead iodide perovskite solar cells, Nat.Commun., 6 (2015) 7497.

[68] H.-S. Kim, N.-G. Park, Parameters affecting I–V hysteresis of CH3NH3PbI3 perovskite solar cells: effects of perovskite crystal size and mesoporous TiO2 layer, J.Phys.Chem.Lett., 5 (2014) 2927-2934.

[69] H.J. Snaith, A. Abate, J.M. Ball, G.E. Eperon, T. Leijtens, N.K. Noel, S.D. Stranks, J.T.-W. Wang, K. Wojciechowski, W. Zhang, Anomalous hysteresis in perovskite solar cells, J. Phys.Chem.Lett., 5 (2014) 1511-1515.

[70] Z. Xiao, Y. Yuan, Y. Shao, Q. Wang, Q. Dong, C. Bi, P. Sharma, A. Gruverman, J. Huang, Giant switchable photovoltaic effect in organometal trihalide perovskite devices, Nat.Mater., 14 (2015) 193-198.

[71] Y. Zhang, M. Liu, G.E. Eperon, T.C. Leijtens, D. McMeekin, M. Saliba, W. Zhang,

M. de Bastiani, A. Petrozza, L.M. Herz, Charge selective contacts, mobile ions and anomalous hysteresis in organic–inorganic perovskite solar cells, Mater. Horiz., 2 (2015) 315-322.

[72] K. Wojciechowski, S.D. Stranks, A. Abate, G. Sadoughi, A. Sadhanala, N. Kopidakis, G. Rumbles, C.-Z. Li, R.H. Friend, A.K.-Y. Jen, Heterojunction modification for highly efficient organic–inorganic perovskite solar cells, Acs Nano, 8 (2014) 12701-12709.

[73] W. Zhou, J. Zhen, Q. Liu, Z. Fang, D. Li, P. Zhou, T. Chen, S. Yang, Successive surface engineering of TiO 2 compact layers via dual modification of fullerene derivatives affording hysteresis-suppressed high-performance perovskite solar cells, J. Mater. Chem. A, 5 (2017) 1724-1733.

[74] V. O. Eze, Y. Seike, T. Mori, Efficient planar perovskite solar cells using solution-processed amorphous WO_x/fullerene C_{60} as electron extraction layers, Organic Electronics, 46 (2017) 253-262

Chapter 6

Summary

Organic-inorganic hybrid perovskite solar cells (PSCs) have received considerable attention because of its excellent photovoltaic properties, high power conversion efficiency (PCE), solution processability and low-cost fabrication. In the PSC configuration, perovskite light-absorbing layer, which is usually sandwiched between the electron transporting layer (ETL) and the hole transporting layer (HTL), is one of the most significant components, indicating that it must be homogenous and void free to guarantee sufficient light-absorption and high PCE. In most studies, high-quality perovskite films on planar substrates are prepared using expensive vacuum facilities such as a glove box and vapor deposition machines with humidity less than 1% to circumvent the problems of non-uniform film morphology and sub-stable characteristics of the perovskites, which is chiefly caused by moisture. However, when considering the production cost and energy payback time of PSCs, high-quality perovskite films fabricated under ambient air environment (i.e., without the use of expensive vacuum equipment) is paramount important. Therefore, it will be highly advantageous and beneficial if homogenous and uniform perovskite layer can be fabricated without the requirement of special precautions.

In this thesis, high-performance PSCs were fabricated on planar substrates. Planar architecture has the advantage of simplified device configuration and fabrication procedure. It is also feasible for flexible and low-temperature substrates, which will further reduce the production cost of PSCs. However, it is challenging to deposit high-quality and uniform perovskite films on a planar substrate in the air due to premature precipitation and sparse nucleation of $CH_3NH_3PbI_3$ perovskites. To improve the uniformity of the perovskite, in **Chapter 3** we demonstrated for the first time the use of two-step spin coating method together with air-assisted flow under ambient air condition. The air flow helps to expedite mass transfer and eliminated non-uniformity in the thickness of the perovskite layers caused by the disparity of centrifugal force between the substrate center and its edge. Also, it can markedly expedite the evaporation of the solvent to suppress the preferential crystallization of PbI_2 and

$CH_3NH_3PbI_3$ during spin-coating. This technique produced perovskite films with improved morphology and coverage to the underneath compact TiO_2 layer. Films characterization results suggest that films prepared with airflow showed improved features, which is beneficial in enhancing the device PCE. The device without airflow exhibited a PCE of 8.67%, whereas a higher PCE of 13.28% was obtained for the device incorporating airflow. This study presents a useful technique for fabricating high-quality perovskite films on planar substrates.

In **chapter 4,** we further demonstrated the importance of dense and uniform perovskite films with large grains for fabricating high-performance PSCs. High-quality perovskite films were deposited using one-step solution process, anti-solvent bath (ASB) method together with solvent annealing in ambient air condition. Diethyl ether (DEE), which has a low boiling point and no solubility or reactivity with the perovskite precursors, was used to extract the *N*-methyl-2-pyrrolidone (NMP) and γ-butyrolactone (GBL) solvents from the spin-coated solution film. This enabled a uniform, highly smooth and glossy perovskite film. While the solvent annealing treatment facilitated further grain growth by a dissolution and precipitation process. The latter approach led to $CH_3NH_3PbI_3$ films exhibiting large grain microstructures, with fewer grain boundaries and crystal defects that reduced carrier recombination. The morphological, structural, and optical features of perovskite films treated with solvent annealing, thermal annealing and without annealing treatment were meticulously and systematically investigated. PSCs containing solvent annealing treatment showed a PCE of 16.77% which is higher than those without solvent annealing treatments. This method offers a facile, and attractive way to fabricate high-quality perovskite films for high-performance solar cells.

Lastly, in **Chapter 5** we demonstrated that the development of alternative electron transport layers (ETLs) is essential to further advance the studies of PSCs. Herein, we showed that low-temperature solution-processed amorphous tungsten (WO_x) and fullerene C_{60} could cooperatively work together as efficient ETLs for high-performance planar PSCs. WO_x has been successfully employed as an ETL in PSCs. However, the WO_x-based devices usually suffer from inherent charge recombination, resulting in a low PCE. In this work, we demonstrated that the carrier injection efficiency of the WO_x-

based PSCs could be further improved by incorporating fullerene C_{60} as an interlayer. Interestingly, the WO_x/C_{60}-based PSCs achieved a PCE of 16.07% under reverse voltage scanning, which is significantly higher than the pristine WO_x-based device. The higher PCE achieved by the WO_x/C_{60} PSCs is attributed to the improved open circuit voltage (V_{oc}) and fill factor (FF), suggesting reduced charged recombination. This work shows a simple and efficient way to fabricate low-temperature and high-performance PSCs under ambient air condition, which will be of particular interest to the photovoltaic community. Low-temperature PSCs is a feasible approach for the future practical application.

6.1 Scope of the Future Work

In this thesis, I have highlighted the importance of morphology control in enhancing the photovoltaic performance of PSCs. Also, I showed the feasibility of fabricating high-performance PSCs with an active area of <0.1 cm^2 under ambient air condition. In order to commercialize PSCs, it must rival the current photovoltaic technologies regarding module efficiency, large-scale fabrication, stability, and cost.

It has been reported that obtaining high-performance and durable PSCs perovskite on a large substrate with active area > 1 cm^2, can be somewhat challenging. To improve the quality and stability of the perovskite films on large area substrates, Saliba et al., and Singh et al., showed that cesium-containing triple cation perovskites is a feasible approach in achieving thermally and moisture stable PSCs with improved reproducibility and high PCE of over 20%. In their work high-temperature mesoporous and planar substrates, respectively, were employed. It is believed that high-temperature substrates may hamper the mass production and commercialization of this cutting-edge technology.

My future work will focus on developing large area (>5 cm^2) PSCs on low-temperature and flexible planar substrates using blade coating and spray coating techniques. Low-temperature processed planar architecture is a feasible approach for large-scale production, flexible device, and tandem application. The surface coverage, uniformity and crystallization of the perovskite layer will be controlled through a combination of airflow and solvent annealing. Also, the stability and reproducibility of the pristine PSCs will be improved by introducing various additives into the perovskite precursor solution. A systematic investigation will be carried out to understand the influence of these additives introduced into the perovskite. Furthermore, I would investigate the underlying photophysics and dynamics of charge transport and recombination process in the resultant perovskites, and perovskites/charge transport layer interface using time-resolved photoluminescence (TRPL), transient absorption spectroscopy (TAS) and so on. I believe that understanding the mechanisms of the underlying photophysics of perovskites mixed with additives would be a proper guide in developing novel ones with enhanced performance.

6.2 References

1) M. Saliba, T. Matsui, J.-Y. Seo, et al., Cesium-containing triple cation perovskite solar cells: improved stability, reproducibility and high efficiency, Energy Environ., Sci., 2016, 9, 1989-1997.
2) T. Singh, T. Miyasaka, Stabilizing the Efficiency Beyond 20% with a Mixed Cation Perovskite Solar Cell Fabricated in Ambient Air under Controlled Humidity, Adv. Energy Mater. 2017, 1700677.

Acknowledgements

The work presented in this dissertation is financially supported by an AIT Special Grant for the Development of Hybrid-Power Science and Technology for Green Energy, a JSPS Grant-in-Aid for Scientific Research (C) 15K060410001, AIT Special Grant for Education and Research, and Hibi Science Foundation.

I would like to express my heartiest gratitude and sincere appreciation to my supervisor, Prof. Tatsuo Mori for giving me the opportunity to join his group and work under his supervision as a doctoral student. His continued support, guidance, and encouragements made this thesis possible. Also, I express my sincere thanks to Dr. Lei Binglong for his mentorship and motivation at the early stage of this work.

I would like to thank Prof. Yuichi Kobayashi, Prof. Nobuhiko Sawaki, and Prof. Hiroyuki Iwata for the X-ray diffraction, photoluminescence, and scanning electron microscopy measurements, respectively. My sincere thanks go to all other university staff in the international student affair office, student affair office, library and departmental office, for their conscious and unconscious assistance.

I would also like to thank my dissertation committee members, Prof. Yoshiyuki Seike, Prof. Yasuo Suzuoki, and Prof. Oosawa Yoshimi for their time and consideration on reviewing my dissertation.

I wish to thank my previous lab-mates Mr. Kousaki Shigematsu and Mr. Takanori Yagi and current lab-mates for their kind assistance.

This doctoral course would not have been possible without the enormous supports and motivation received from Prof. Noboru Sugino, Prof. Charles Kelly, Prof. Kazuhiko Eguchi, Dr. Ogeneochukome Lolodi, and Dr. Tubodenyefa Zibima. Their words of encouragement are highly appreciated.

Finally, I would like to thank my dear friend Ms. Nelly Nsah, parents, brothers and sisters for their unrelenting support and prayers.

List of research papers

Published in Journals/International and Domestics Conferences

論文題目	公表の方法及び時期	著者
(1). ジャーナル:		
1.) Improvement of Photovoltaic Properties for Unmodified Fullerene C_{60} Based Polymer Solar Cells by Addition of Fusible Fullerene	J. Photopolym. Sci. Technol., 4 (2017) 501–506.	Tatsuo Mori, Daiki Sato, Takaya Egami, Vincent Obiozo Eze
2.) Efficient planar perovskite solar cells using solution-processed amorphous WO_x/fullerene C_{60} as electron extraction layers	Organic Electronics 46 (2017), 253-262	Vincent Obiozo Eze, Yoshiyuki Seike, Tatsuo Mori
3.) Enhanced photovoltaic performance of planar perovskite solar cells fabricated in ambient air by solvent annealing treatment method	Jpn. J. Appl. Phys., 55 (2016), 122301	Vincent Obiozo Eze, Tatsuo Mori
4.) Effect of Morphology Control of Light Absorbing Layer on $CH_3NH_3PbI_3$ Perovskite Solar Cells	J. Nanosci. Nanotechnol., 4 (2016), 3176-3182.	Binglong Lei, Vincent Obiozo Eze, Tatsuo Mori
5.) Air-assisted flow and two-step spin-coating for highly efficient $CH_3NH_3PbI_3$ perovskite solar cells	Jpn. J. Appl. Phys., 55 (2016), 02BF08.	Vincent Obiozo Eze, Binglong Lei, Tatsuo Mori

6.)Organic-Inorganic Hybrid Perovskite Solar Cells Using Hole Transport Layer Based on α-Naphthyl Diamine Derivative	J. Photopolym. Sci. Technol., 4 (2016), 581-586.	Vincent Obiozo Eze, Tatsuo Mori
7.)High-performance $CH_3NH_3PbI_3$ perovskite solar cells fabricated under ambient conditions with high relative humidity	Jpn. J. Appl. Phys., 54 (2015), 100305.	Binglong Lei, Vincent Obiozo Eze, Tatsuo Mori
(2). 国際会議:		
1.) High-performance Planar perovskite Solar Cells with WO_x/C_{60} Electron Transporting Layer	The 9th Asian Conference on Organic Electronics (A-COE), October 25-27, 2017. KAIST, Daejeon, Korea.	Vincent Obiozo Eze, Yoshiyuki Seike, Tatsuo Mori
2.) Low Temperature Fabrication of Inverted Organic Perovskite Solar Cells Using Air-Assisted Flow	The 9th Asian Conference on Organic Electronics (A-COE), October 25-27, 2017. KAIST, Daejeon, Korea.	Hiroyuki Okada, Yuta Kondo, Mitsutaka Hoshino, Vincent Obiozo Eze, Yoshiyuki Seike, Tatsuo Mori
3.) Effect of Additive Inclusion and Solvent Annealing on the performance of Inverted Structure $CH_3NH_3PbI_{3-x}Cl_x$ Perovskite Solar Cells Fabricated Under High Humidity	11th Aseanian Conference on Nano-Hybrid Solar Cells (NHSC11) 2017. October 8-10, 2017. October 8-10, 2017. Egret Himeji Convention Hall, Himeji, Japan.	Vincent Obiozo Eze, Yoshiyuki Seike, Tatsuo Mori

4.) Effect of Fullerene C_{60} Interlayer in Enhancing the Performance of Amorphous Tungsten Oxide Planar Perovskite Solar Cells	9thInternational Conference on Molecular Electronics and Bioelectronics M & BE9, June 26-28, 2017. Ishikawa Ongakudo and ANA Crowne Plaza Kanazawa, Kanazawa, Japan.	Vincent Obiozo Eze, Yoshiyuki Seike, Tatsuo Mori
5.) Effect of Air Assisted Flow on Organic Perovskite Solar Cells Fabricated by One Step Spin-Coating Method	The 6th International Symposium on Organic and Inorganic Electronic Materials and Related Nanotechnologies (EM-NANO) June 19-21, 2017. AOSSA building, Fukui, Japan	Hiroyuki Okada, Kenta Saito, Vincent Obiozo Eze, Yoshiyuki Seike, Tatsuo Mori
6.) $CH_3NH_3PbI_3$ perovskite solar cells employing Cu-phthalocyanine doped poly-3-hexylthiophene hole-transporting layer	The 8th Asian Conference on Organic Electronics (A-COE), December 5-7, 2016. Uji Obaku Plaza, Kyoto University, Uji, Kyoto, Japan.	Vincent Obiozo Eze, Yoshiyuki Seike, Tatsuo Mori
7.) Cu-phthalocyanine doped poly-3-hexylthiophene based hole-transporting layer for efficient mesoscopic $CH_3NH_3PbI_3$ perovskite solar cells	The 11th International Conference of Electroluminescence and Optoelectronic devices (ICEL). October 2-5, 2016. Sheraton Raleigh Hotel, Raleigh North Carolina, USA.	Vincent Obiozo Eze, Yoshiyuki Seike, Tatsuo Mori

8.)Organic-Inorganic Hybrid Perovskite Solar Cells Using Hole Transport Layer Based on α-Naphthyl Diamine Derivative	The 33rd International Conference of Photopolymer Science and Technology. June 22-24, 2016. International Conference Hall, Makuhari Messe, Chiba, Japan.	Vincent Obiozo Eze, Yoshiyuki Seike, Tatsuo Mori
9.) Benefit of solvent annealing for $MAPbI_3$ Planar Perovskite Solar Cells Fabricated by One-Step Spin-Coating and Antisolvent Bath Methods	9th International Symposium on Organic Molecular Electronics (ISOME). May 18-20, 2016. Tokimate, Niigata, Japan.	Vincent Obiozo Eze, Tatsuo Mori
10.) Planar $CH_3NH_3PbI_3$ Perovskite Solar Cells Prepared with Inclusion of Polyvinylpyrrolidone	International Electron Devices and Material Symposium (IEDMS). November 19-20, 2015. Kun Shan University, Tainan, Taiwan.	Vincent Obiozo Eze, Binglong Lei, Tatsuo Mori
11.) Performance of Organic Perovskite Photovoltaic Using TiO_2 Dense Layer Fabricated by Spray Pyrolysis or Spin Coating	The 7th Asian Conference on Organic Electronics, October 28-31, 2015.Peking University, Beijing, China.	Takanori Yagi, Vincent Obiozo Eze, Binglong Lei, Tatsuo Mori
12.) Air-Assisted Flow and Two Step Spin-Coating for High Efficient $CH_3NH_3PbI_3$ Perovskite Solar Cells	The Fifth International Symposium on Organic and Inorganic on Electronic Materials and Related Nanotechnologies (EM-NANO). Japan. 16-19, 2015. Toki Messe Niigata Convention Center	Vincent Obiozo Eze, Binglong Lei, Tatsuo Mori

(3). 国内会議： 1.) エアフローを用いた逆構造有機ペロブスカイト太陽電池の作製	第78回応用物理学会秋季学術講演会, (2017) 5p-PA3-21 2017年9月5日～8日福岡国際会議場国際センター福岡サンパレス	岡田 紘幸, 近藤 勇太, 星野 充崇, ビンセント オビオゾ エゼ, 清家 善之, 森 竜雄
2.) 有機ペロブスカイト太陽電池の活性層へのエアフロー効果	第64回応用物理学会春季学術講演会, (2017)16p-p6-28 2017年3月14日～17日パシフィコ横浜	岡田 紘幸, ビンセント オビオゾ エゼ, 清家善之, 森 竜雄,
3.)Efficient Planar Perovskite Solar Cells Using Solution-Processed Amorphous WO_x/Fullerene C_{60} as Electron Extracting Layers	第64回応用物理学会春季学術講演会, (2017)16p-p6-28 2017年3月14日～17日パシフィコ横浜	Vincent Obiozo Eze, Yoshiyuki Seike, Tatsuo Mori
4.) Influence of Airflow on $MAPbI_3$ Perovskite Solar Cells Fabricated by Two-Step Spin-Coating Method	電子情報通信学会(2017). 2017年3月22日～25日名城大学天白キャンパス	Vincent Obiozo Eze, Binglong Lei, Tatsuo Mori
5.) $CH_3NH_3PbI_3$ Perovskite Solar Cells Employing Cu-Phthalocyanine Doped Poly-3-hexylthiophene Hole-Transporting Layer.	第77回応用物理学会秋季学術講演会(2016) E 14a-A41-11. 2016年9月13日～１６日トキメッセ、新潟コンベンションセンター	Vincent Obiozo Eze, Yoshiyuki Seike, Tatsuo Mori

6.) 有機ペロブスカイト太陽電池の高効率化の為の酸化チタン緻密 層の表面解析	第77回応用物理学会秋季学術講演会(2016) 15p-A41-15. 2016年9月13日～１６日トキメッセ、新潟コンベンションセンター	八木 崇徳, エゼ オビオゾ・ヴィンセント, 清家 善之, 森 竜雄
8.) Facile Fabrication of Planar Perovskite Solar Cells via One-step Spin-Coating and Antisolvent Bath Methods.	第63回応用物理学会春学会講演会 (2016) 20a-W531-6. 2016年3月19日～22日大岡山キャンパス、東京工業大学	Vincent Obiozo Eze,Tatsuo Mori
9.) 有機ペロブスカイト太陽電池における TiO2 緻密層の影響	第63回応用物理学会春学会講演会 (2016) 19a-P5-22. 2016年3月19日～22日大岡山キャンパス、東京工業大学	八木 崇徳, エゼ ヴィンセント・オビオゾ, 森 竜雄
10.) Improved $CH_3NH_3PbI_3$ Perovskite Morphology for Highly Efficient Solar Cells via Air-Assisted Flowing in the Two-Step Spin Coating Method	第76回応用物理学会秋季学術講演会(2015) E 14a-1G-3. 2015年9月13日～16日名古屋国際会議場	Vincent Obiozo Eze, Binglong Lei, Tatsuo Mori
11.) 有機ペロブスカイト太陽電池に対するスプレー熱分解とスピンコート酸化 チタン緻密層の違い	第76回応用物理学会秋季学術講演会 (2015) 13p-PB9-26. 2015年9月13日～16日名古屋国際会議場	八木 崇徳, 雷 丙尤, エゼ オビオゾビンセント, 森 竜雄